INVESTIGATION OF THE THERMAL AND ELECTRICAL PROPERTIES OF GRAPHENE

WANG ZIQIAN
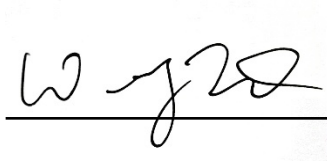
(B. Eng. (Hons), National University of Singapore)

A THESIS SUBMITTED

FOR THE DEGREE OF DOCTOR OF PHILOSOPHY

DEPARTMENT OF ELECTRICAL AND COMPUTER ENGINEERING

NATIONAL UNIVERSITY OF SINGAPORE

2012

DECLARATION

I hereby declare that the thesis is my original work and it has been written by me in its entirety. I have duly acknowledged all the sources of information which have been used in the thesis.

This thesis has also not been submitted for any degree in any university previously.

Wang Ziqian

23 July 2012

Acknowledgements

Table of Contents

Summary

Graphene is believed to possess very high thermal conductivity (κ) near room temperature, making it a promising material for thermal management in electronic devices. However, there is a lack of systematic experimental studies on its thermal properties, mainly due to the difficulties in preparing and conducting such measurements on graphene samples.

At the outset, two existing approaches were considered: the non-contact Raman technique, and the thermal-bridge technique using a top-down microfabricated device. The former provides limited accuracy in determining κ while the latter is only applicable to supported samples. In view of the drawbacks, we developed a process to transfer and pattern graphene samples on a pre-fabricated MEMS device that incorporates thermal-bridge structures. This approach has two main advantages: it allows precise control over the size and shape of the graphene flake; and it can be used to measure both suspended and supported samples.

Thermal conductance measurements were first carried out on a set of supported graphene samples with different sizes. It was observed that the room temperature κ is comparable to that of bulk graphite for the largest flake, but reduces significantly for smaller flakes due to cut-off of low-frequency phonons involved in heat conduction. This is consistent with the predictions of many theoretical works, and provides the first experimental evidence for the size dependence of κ in graphene. By comparing the κ values of graphene of the same lateral dimensions with and without a support, it was shown that the presence of a substrate impedes thermal transport due to phonon scattering at the interface, and the effect is weaker for thicker flakes showing diminished scattering in the top layers away from the interface.

For supported samples, κ increases with T and saturates at $310 - 360$ K, which agrees well with published results. However, for the suspended sample, $\kappa - T$ shows no saturation and followed a power law with an exponent of 1.4 ± 0.1, suggesting that the flexural phonon modes contribute significantly to the thermal transport. Thermal boundary scattering at the graphene-contact interfaces was studied by a non-contact electron beam heating method, which can spatially resolve the thermal resistance at any position on the sample. It was found that significant scattering occurs at the contacts especially for small flakes, as a result of material and structural changes.

Furthermore, the samples were exposed to various gas ambients instead of vacuum to study the effects of gas adsorption. κ shows negligible change at 300 K, but increases substantially at low temperatures due to adsorbates forming parallel thermal conduction paths. It was discovered that adsorption of molecular nitrogen introduced n-type doping to graphene. The charge transfer takes place both at single vacancies and at the edges, with the latter being the dominant sites. The doping effect can be controlled via a perpendicular electric field, which can shift the Fermi level of graphene and change the energy barrier of the charge transfer process. Combined with published results on the p-type doping effect of oxygen gas, electric-field-controlled doping of graphene was demonstrated by selective charge transfer from different gas adsorbates.

List of Figures

List of Symbols

v	phonon velocity
ω	phonon frequency
Λ	phonon mean free path
Q	heating power
I_h	heating current
$I_{lock\text{-}in}$	lock-in current
$f_{lock\text{-}in}$	frequency of $I_{lock\text{-}in}$
T	temperature
T_h	temperature of *heater*
T_s	temperature of *sensor*
ΔT_h	temperature rise on *heater*
ΔT_s	temperature rise on *sensor*
T_{sub}	substrate temperature
T_c	2D critical temperature
S	Seebeck coefficient
C_v	specific heat
κ	thermal conductivity
G_b	thermal conductance of six SiN$_x$ beams
G_s	thermal conductance of sample
G_{SiNx}	thermal conductance of supporting SiN$_x$ platform
R_{total}	thermal resistance from *heater* to *sensor*
R_i	thermal resistance from *heater* to electron beam position i
R_b	thermal resistance of six SiN$_x$ beams
R_c	contact thermal resistance
Z	acoustic impedance
ρ	density
E	Young's modulus
V_g	gate voltage
V_{dp}	gate voltage at Dirac point
p	hole concentration
n	electron concentration
n_i	gate-induced electron concentration
σ	electrical conductivity
μ	charge carrier mobility
R	electrical resistance
R_h	electrical resistance of *heater*
R_s	electrical resistance of *sensor*
R_L	electrical resistance of two SiN$_x$ beams for passing I_h
L	length of sample
W	width of sample
h	thickness of sample
t	time
t_{ml}	monolayer formation time
τ	time constant for adsorption

Chapter 1   Introduction

1.1   Background

Graphene, the mono-atomic layer of carbon atoms arranged in a honeycomb lattice, has garnered great interest since groundbreaking experiments reported in 2004 [1] due to its many extraordinary physical properties. This two-dimensional system is remarkably different from conventional bulk materials from a fundamental physics point of view. Intrinsic graphene is a semi-metal or a zero-gap semiconductor, and its energy dispersion is linear near the six corners of the Brillouin zone, leading to zero effective mass for electrons and holes [2] which behave like relativistic particles following the Dirac equation [3] instead of the usual Schrödinger equation. Hence graphene offers a platform to study relativistic physics in a non-relativistic material.

Graphene exhibits superior room temperature carrier mobility exceeding 200000 $cm^2V^{-1}s^{-1}$ [4]. The possibility of bandgap opening through lateral quantum confinement, and the prospects for large-area epitaxial growth make graphene a promising material for future electronics [5]. Much effort has been devoted to the fabrication of graphene field-effect-transistors (FETs), and the field is advancing very fast. In 2004, the first graphene FET was demonstrated by the Manchester group with an on-off ratio of ~30 at room temperature [1]. In 2009, Sordan *et al.* demonstrated four different types of logic gates, each composed of a single graphene transistor [6]. In 2010, researchers at IBM reported the successful fabrication of graphene FETs with a cutoff frequency of 100 GHz, exceeding the speed of silicon FETs with an equal gate length [7]. The replacement of silicon by graphene FETs is no longer a dream.

To duplicate the Si-based CMOS technology, graphene needs to be first doped n-type or p-type. Schedin *et al.* doped graphene with gaseous species including both donors and acceptors, and found that the carrier mobility is little affected even for dopant concentrations higher than 10^{12} cm^{-2} [8]. However, Chen *et al.* doped graphene with potassium and found that the ions act as charged impurities in graphene [9] and can significantly reduce the mobility [10]. In both experiments, the graphene can be restored to its initial state after removing the dopants through vacuum annealing. Increasing research effort is being invested in the controllable doping of graphene without degradation of its carrier mobility.

Due to the light weight of the constituent carbon atoms and the superior crystallinity of its lattice, graphene is believed to have very high thermal conductivity near room temperature [11-13], which is recently measured to be ~5000 Wm^{-1}K^{-1} [14]. This exceeds those measured for carbon nanotubes and diamonds, and is many times higher than that of common metals, thus graphene can be potentially used for thermal management in electronic devices. The thermal conduction is phonon-dominated, and is contributed by three acoustic phonon branches. The relative contribution of the in-plane and flexural modes still remains a subject of argument [14, 15], and is yet to be experimentally verified.

1.2   Motivation and objectives

In spite of numerous interesting theoretical predictions, few experimental studies [14, 16-19] have been reported on the thermal properties of graphene, mainly due to the difficulties in preparing and conducting such measurements on graphene samples. The room temperature thermal conductivity κ of suspended single-layer graphene has been measured with a micro-Raman technique; however reported data

show wide variations with values ranging from 600 to 5000 $Wm^{-1}K^{-1}$ [14, 16]. As this technique is normally applied under ambient conditions, the accuracy in estimating κ is not only limited by various assumptions about the laser power absorbed, but also by unknown convective heat losses. By comparison, the conventional thermal-bridge setup offers direct measurements of the heating power and precise temperature readout in vacuum, from which κ can be conveniently and accurately extracted. While this technique has been used to study the thermal transport of supported graphene [19], the method reported is not applicable to suspended samples. In this project, effort is expended on the improvement of the thermal-bridge technique to allow a systematic study of the thermal properties of both suspended and supported samples. Various parameters affecting the thermal transport in graphene, in particular the sample size and temperature dependence of the thermal conductivity, are to be thoroughly investigated.

On the electrical aspect, two major issues in making graphene-based integrated circuits are the lack of a bandgap, and how to dope graphene. The former has been extensively studied, where the bandgap can be opened through quantum confinement by making graphene nanoribbons [20-22], or by breaking the lattice symmetry of bilayer graphene through molecular adsorption [23, 24] or through the application of asymmetric electric fields [25, 26]. Doping is relatively less explored. Unlike silicon which can be easily doped by implantation of Group III and V elements, the incorporation of dopant atoms in the graphene lattice is more difficult, and can result in severe degradation of the carrier mobility [27, 28]. In this work, doping by a gas adsorption approach will be explored. The electrical properties of graphene will be studied in various gas ambients, and efforts will be devoted to find a method that can controllably dope graphene via surface gas adsorption.

The main objectives of this project are to conduct a systematic study of the thermal transport in graphene, and to explore the effects of gas adsorption on the thermal and electrical properties of graphene.

1.3 Organization of thesis

This thesis is organized as six chapters, with the first chapter being the introduction.

Chapter 2 covers a literature review on the thermal transport in graphitic materials, which consist of carbon nanotubes, graphene and graphite.

The sample fabrication techniques and measurement methodologies are described in Chapter 3.

In Chapter 4, a systematic experimental study of the thermal transport in graphene is presented. The sample size and temperature dependence of its thermal conductivity, substrate effect, and thermal boundary resistances are discussed.

The effects of gas adsorption on the thermal and electrical properties of graphene are investigated in Chapter 5. It is discovered that adsorption of molecular nitrogen introduces n-type doping to graphene, where the charge transfer can be controlled by applying a perpendicular electric field.

Chapter 6 summarizes the accomplishments of this project and provides recommendations for future work.

References used in the thesis are listed at the end of the thesis.

Chapter 2   Literature Review

2.1   Thermal transport in graphite

Graphite, the most stable allotrope of carbon under standard conditions, has garnered undying interest from researchers in various disciplines due to its many extraordinary properties. It consists of layers of sp^2-hybridized carbon weakly bonded by van der Waals forces, and exists in many different natural and artificial forms. Scientific studies of its thermal properties started with the successful production of pyrolytic graphite [29] in the late 19th century. Due to its layered structure, graphite has large anisotropy in thermal conduction, where the in-plane thermal conductivity is more than 2 orders of magnitude larger than the cross-plane value at room temperature [30]. Therefore unless otherwise stated, the thermal conductivity discussed in this section all refers to the more interesting in-plane value.

In 1923, Pirani and Fehse [31] discovered that carbon filaments with well-aligned crystallites of graphite possess a thermal conductivity higher than that of copper. In spite of their great practical importance, systematic studies of the thermal properties were difficult in the earlier years due to the poor and varying quality of individual graphite pieces.

Like any other nonmetallic crystals, the thermal conduction in graphite is chiefly the result of transfer of elastic vibrations via valence bonds, with a negligible contribution from the free electrons except at very high temperatures [32]. According to Debye's formula $\kappa = \frac{1}{3} C_v v \Lambda$ [33], where C_v is the specific heat, v is the phonon velocity, and Λ is the phonon mean free path (MFP), the thermal conductivity κ strongly depends on Λ. At low temperatures, Λ is limited by the microcrystalline dimensions Λ_0, and $\kappa \sim C_v$. At elevated temperatures, Λ is dominated by the phonon-

phonon interactions (Λ_L) commonly referred to as Umklapp scattering, which gives κ ~ T^{-1} [34]. A maximum of κ is expected when the boundary scattering $1/\Lambda_0$ is comparable to the lattice scattering $1/\Lambda_L$. Therefore, the temperature dependence curve of κ is always similar in shape, but the magnitude of κ and its turnover temperature are determined by the sample crystalline quality. Shown in Figure 2.1 are the κ of polycrystalline graphite obtained from different production techniques, where the peak value ranges from 100 to 4000 $Wm^{-1}K^{-1}$ depending on the perfection of individual crystallites and the fraction of non-graphitic carbon.
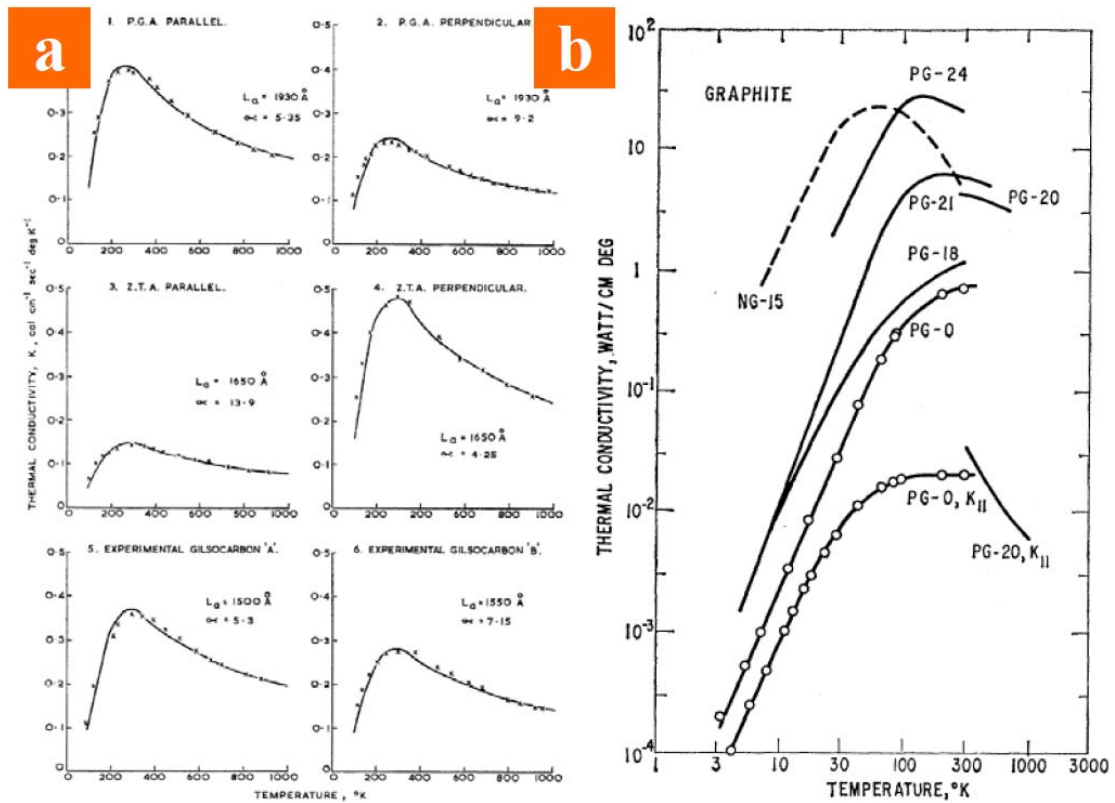
Figure 2.1: (a) Comparison of predicted and measured thermal conductivities [35]. (b) The thermal conductivity of various samples of pyrolytic graphite (PG) and one sample of natural graphite (NG) [36].

In addition to Λ_0 and Λ_L, Λ is also affected by the presence of point defects:

$\frac{1}{\Lambda} = \frac{1}{\Lambda_0} + \frac{1}{\Lambda_L} + \frac{1}{\Lambda_d}$, where Λ_d is the phonon MFP due to defect scattering. Figure

2.2(a) shows the drastic decrease of Λ at increasing vacancy concentrations. By

annealing at extremely high temperatures, the lattice reconstruction as well as the removal of most point defects will result in significant improvement in Λ, as shown in Figure 2.2(b). However, the annealing process cannot eliminate the ^{13}C isotopes, which has a natural abundance of 1.1 %. Since the mass of the isotope is very close to the host lattice atom ^{12}C, in most cases the isotope scattering may be neglected except in high quality crystals where $\Lambda_0 > 3$ μm.
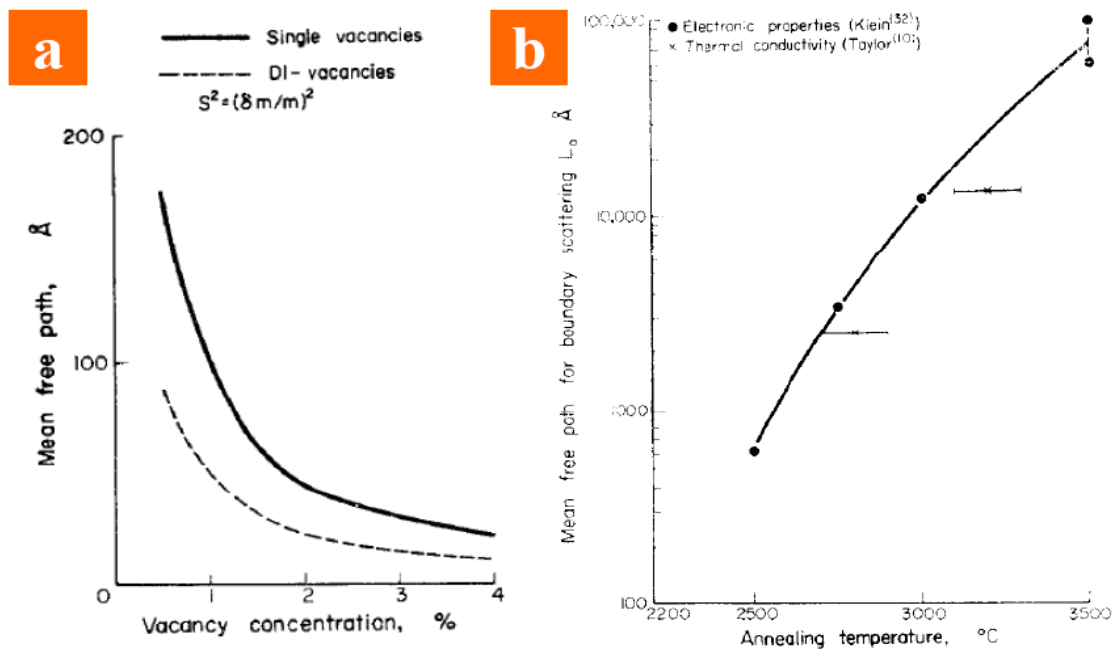
Figure 2.2: (a) Variation of mean free path at room temperature with vacancy concentration for single vacancies and divacancies for in-plane waves. (b) Comparison of mean free paths for boundary scattering as a function of heat treatment in pyrolytic graphite using thermal and electrical properties [37].

Although the uncontrollable sample specifications, and inability to reproduce and directly compare with others' results had complicated the experimental studies in this area, the interest in the thermal properties of graphite has never subsided, especially after the discovery of its counterpart 1D and 2D allotropes that will be discussed below.

7

2.2 Thermal transport in carbon nanotubes (CNTs)

Thermal measurement of CNT, the one-dimensional (1D) counterpart of graphite, is much more complicated mainly due to the difficulties encountered in the sample preparation process. For thermal isolation from bulk substrate and other heat sinks, the CNT under test needs to be fully suspended between temperature sensors. Shown in the upper inset of Figure 2.3(a) is a typical test device mounted with a small bundle of multi-walled carbon nanotubes (MWNT) [38]. A micro-electro-mechanical system is delineated by a series of electron beam lithography (EBL) and photolithography steps followed by metallizations and released by etching away the silicon substrate [39]. The measurement device includes two adjacent silicon nitride (SiN_x) membrane islands suspended with long SiN_x beams. A thin Pt serpentine loop is deposited on each island to serve as both an electrical heater and a resistive thermometer where the temperature is extracted from its resistance value [40]. The CNT is placed on the device to bridge the two suspended islands by utilizing nano-manipulated probes and forms the only thermal path between them. When an electrical current is passed through one of the Pt resistors, the temperature of that island will rise due to Joule heating. At steady state, the system can be analyzed with a simple heat transfer model shown in Figure 2.3(a) lower inset. The thermal conductance of the MWNT bundle, K_t, and the suspending legs, K_d, are related by:

$$T_h = T_0 + \frac{K_d + K_t}{K_d(K_d + 2K_t)}P \text{ and } T_s = T_0 + \frac{K_t}{K_d(K_d + 2K_t)}P$$

where P is the Joule power applied to the resistor R_h. From the slopes of the electrical resistances R_h and R_s versus P, the thermal conductance K_t of the sample at temperature T_0 can be computed.

The temperature dependence of the thermal conductance of an individual MWNT is measured and shown in Figure 2.3(b). At low temperatures (8 – 50 K), $\kappa(T) \sim T^{2.5}$. In the intermediate temperature range (50 – 150 K), $\kappa(T) \sim T^2$. Above this range, $\kappa(T)$ deviates from quadratic temperature dependence, peaks at 320 K, and then decreases rapidly. For MWNT, below the Debye temperature of interlayer phonon mode $\Theta_\perp$, $\kappa(T)$ has slight three-dimensional nature, and $\kappa(T) \sim T^{2.5}$ as observed in graphite single crystals [41]. When $T > \Theta_\perp$, the interlayer phonon modes are fully occupied, and $\kappa(T) \sim T^2$, indicative of the 2D nature of thermal conduction in MWNT. From this crossover behavior of $\kappa(T)$, $\Theta_\perp$ is estimated to be ~50 K, comparable to the value obtained by a measurement of specific heat of MWNT [42]. As T increases further, phonon-phonon Umklapp scattering becomes dominant due to the thermal population of higher energy phonons, and $\kappa(T)$ starts to decrease.
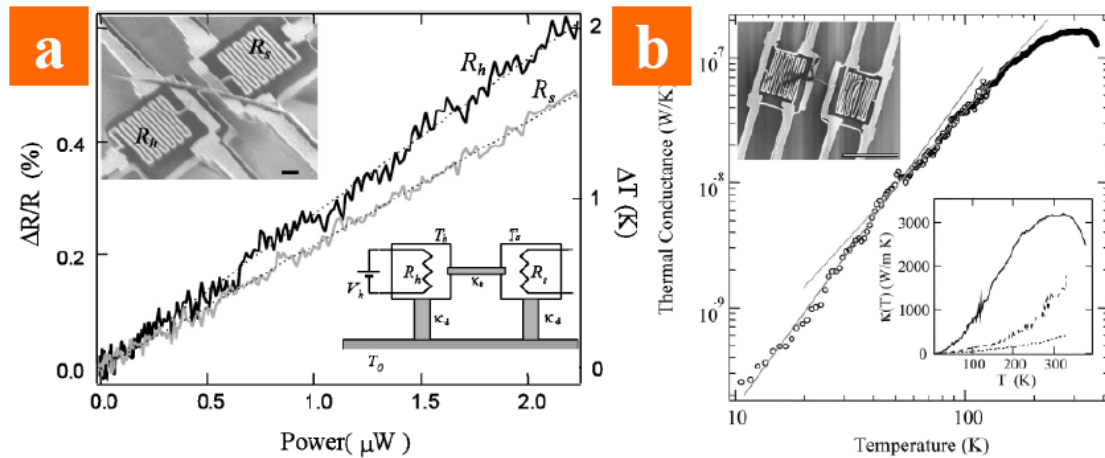
Figure 2.3: (a) The change of resistance of the heater resistor (R_h) and sensor resistor (R_s) as a function of the applied power to the heater resistor. Upper inset: SEM image of the suspended islands with a MWNT bundle across the device. The scale bar represents 1 μm. Lower inset: A schematic heat flow model of the device. (b) The thermal conductance of an individual MWNT of a diameter 14 nm. The solid lines represent linear fits of the data in a logarithmic scale at different temperature ranges. The slopes of the line fits are 2.50 and 2.01, respectively. Lower inset: Solid line represents $\kappa(T)$ of an individual MWNT ($d = 14$ nm). Broken and dotted lines represent small ($d = 80$ nm) and large bundles ($d = 200$ nm) of MWNTs, respectively. Upper inset: SEM image of the suspended islands with the individual MWNT. The scale bar represents 10 μm [38].

In bulk solids like graphite, heat transfer follows the empirical Fourier's law, which states that the thermal conductance of a material scales inversely with its length,

or equivalently, κ is independent of the system size. However, this is violated for a variety of one-dimensional systems [43] such as CNTs and boron nitride nanotubes (BNNTs). By sequentially depositing Pt contact pads along the nanotube, its thermal conductance at different lengths can be extracted. The length dependence is shown in Figure 2.4, where κ is found to follow $L^{0.6}$ and $L^{0.5}$ for CNT and BNNT, respectively. Classically, the phonon mean free path (Λ) is a characteristic length beyond which phonons lose their phase coherence, and conduction follows Fourier's law in bulk materials when $L \gg \Lambda$. Nevertheless, even in the purely diffusive regime ($L \gg \Lambda$), many 1D systems do not obey Fourier's law [44-47]. This extraordinary behavior of low-dimensional systems could be due to quantum confinement effect, anharmonicity of the lattice [43] and other disorders [48].
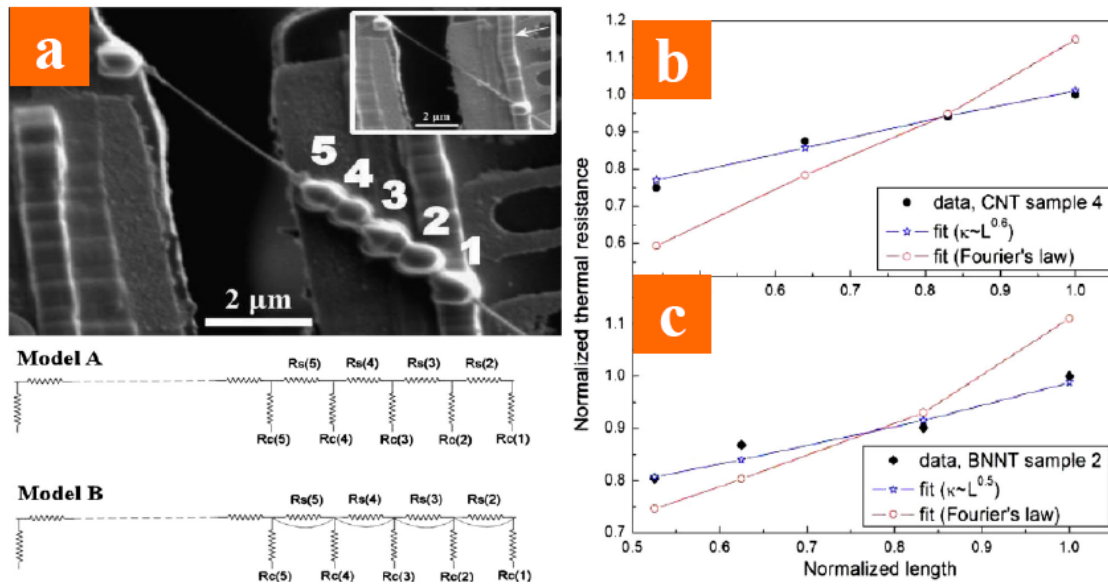
Figure 2.4: (a) Upper: A SEM image of a thermal conductivity test fixture with a BNNT after five sequences of $(CH_3)_3(CH_3C_5H_4)Pt$ deposition. The numbers denote the nth deposition. The inset shows the SEM image after the first $(CH_3)_3(CH_3C_5H_4)Pt$ deposition. The arrow denotes the preformed rib for suspending the BNNT. Lower: Two circuit models for analyzing the data of BNNT. $R_s(n)$ and $R_c(n)$ denote the sample resistance and the contact resistance at each deposition, respectively. (b) Normalized thermal resistance vs normalized sample length for CNT (solid black circles), best fit assuming $\beta = 0.6$ (open blue stars), and best fit assuming Fourier's law (open red circles). (c) Normalized thermal resistance vs normalized sample length for BNNT (solid black diamonds), best fit assuming $\beta = 0.4$ (open blue stars), and best fit assuming Fourier's law (open red circles) [49].

In addition to the length dependence, κ of CNT is also strongly affected by its diameter. For a very narrow single-walled carbon nanotube (SWNT), the value of κ is smaller than that of a monolayer graphene and approaches from below as the diameter increases, as shown in Figure 2.5. This is because graphene has reflection symmetry which strongly restricts phonon-phonon scattering, whereas the inherent curvature in SWNT breaks the reflection symmetry and results in a reduction in κ.
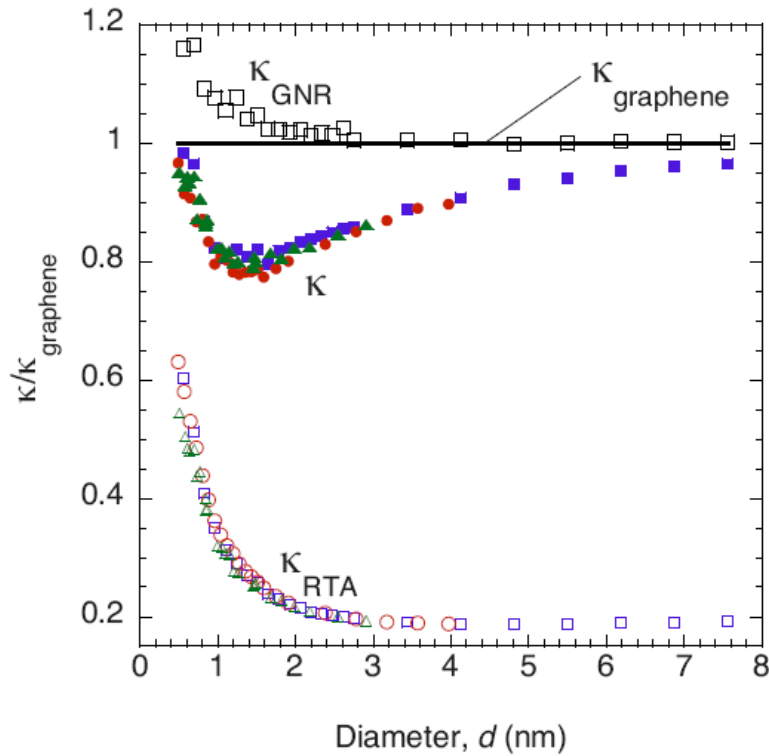
Figure 2.5: κ vs d for a variety of zigzag (solid red circles), armchair (solid blue squares), and chiral (solid green triangles) SWCNTs. The black line shows $\kappa_{graphene}$ while the black open squares give κ_{GNR}. Open red circles, blue squares, and green triangles are RTA results for zigzag, armchair, and chiral SWCNTs. For all cases, $L = 3$ μm and $T = 300$ K. All values are scaled by $\kappa_{graphene}$ [50].

For a MWNT, the intertube coupling also plays an important role in the heat transfer. Analogous to the weak interlayer interaction between graphene layers in bulk graphite, ideally the interaction between these concentric tube walls is very limited. The phonon scattering on different walls is vanishingly small since it is difficult to conserve the momentum. However, due to the imperfect growth processes, vacancies, junctions and intertube misalignments are commonly present in the MWNT. These

11

disorders can induce strong coupling between the tube walls and change the selection rule for the phonon-phonon scattering [51]. The value of κ is calculated for both strong and weak intertube coupling, and compared in Figure 2.6, where the intertube interaction is shown to substantially affect κ. This may also explain the low values of κ measured in several experiments [42, 52-59].
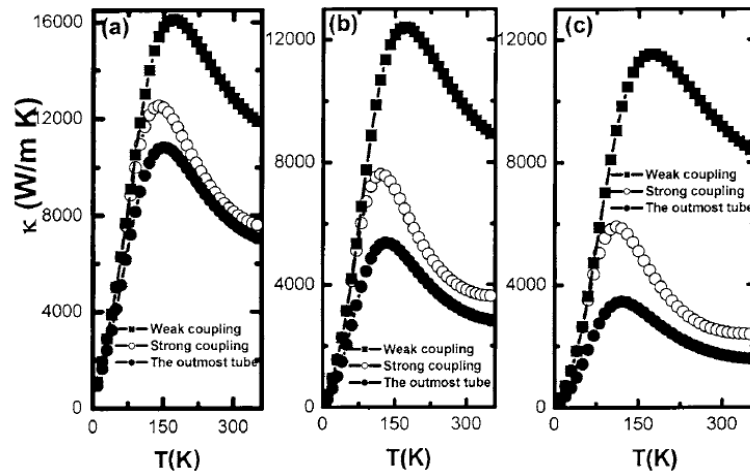
Figure 2.6: Thermal conductivity of (a) double-walled, (b) triple-walled, and (c) quadruple-walled MWCNTs for the weak (solid squares) and strong (open circles) intertube couplings [51].

Although many studies have demonstrated the superior thermal properties of individual CNTs [60-64], they easily form bundles [65] and the actual κ is affected by many factors. Therefore, the lack of control still remains an issue that limits the application of CNTs in thermal management devices [66].

2.3   Thermal transport in graphene

2.3.1 Thermal conductivity measurement techniques

There are mainly two approaches for the thermal conductivity measurements of graphene, based on Raman spectroscopy and the thermal-bridge configuration.

The first reported thermal conductivity (κ) measurement of graphene was performed by Balandin *et al*. [14] on a suspended single layer flake by a novel micro-

Raman technique. As shown in Figure 2.7, a 3 μm wide trench with a nominal depth of 300 nm is fabricated on a SiO$_2$/Si substrate by reactive ion etching (RIE), and a single layer graphene (SLG) flake is mechanically exfoliated to suspend over the trench. Measurements are carried out using confocal micro-Raman spectroscopy which restricts the sampling volume to the suspended portion of the graphene flake. The laser beam is focused at the centre of graphene which causes a local temperature rise due to the laser excitation of the SLG. Assuming heat conduction through air is negligible, the heat has to propagate laterally through the extremely thin graphene layer. Thus a small dissipated power can result in a detectable temperature rise at the laser spot. The G peak in the Raman spectroscopy of graphene shifts approximately linearly with the local temperature rise [67, 68], and the thick graphitic layers attached at the two sides are assumed to be good heat sinks that stay at room temperature. The thermal conductivity of the SLG can be evaluated as $\kappa = \chi_G \dfrac{L}{2hW}(\dfrac{\delta\omega}{\delta P})^{-1}$, where L, h and W are the length, thickness and width of the SLG respectively, χ_G is the pre-determined temperature coefficient of G peak shift, and $\dfrac{\delta\omega}{\delta P}$ is the G peak shift over the change in the heating power on graphene.
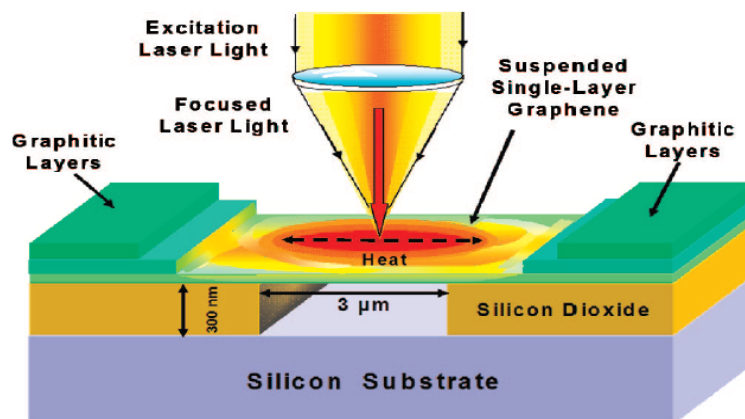
Figure 2.7: Schematic of the experiment showing the excitation laser light focused on a graphene layer suspended across a trench. The focused laser light creates a local hot spot and generates a heat wave inside SLG propagating toward heat sinks [14].

The biggest merit of this Raman technique is the ease of sample fabrication and measurement setup. Since graphene flakes are directly exfoliated on pre-defined trenches on the SiO_2/Si substrate without any patterning or chemical processes, and the measurement is done using a non-contact optical method, the superior quality of graphene can be preserved with minimal contamination. In addition, the dimension of the graphene sample is conveniently tailored by the size of the pre-defined trench. Hence this technique provides high throughput in the characterization of thermal properties of graphene.

Nevertheless, there are several drawbacks of this Raman technique. Firstly, the temperature rise is determined from either the red shift of the G-band or 2D-band frequency [14, 17], or from the Anti-Stokes/Stokes ratio [16], which all give very limited temperature sensitivity as demonstrated by the large scatter of data in Figure 2.8. Hence the temperature rise in the suspended graphene is often larger than 50 K to improve the accuracy. The large temperature difference across the graphene sample makes accurate temperature dependence study difficult.
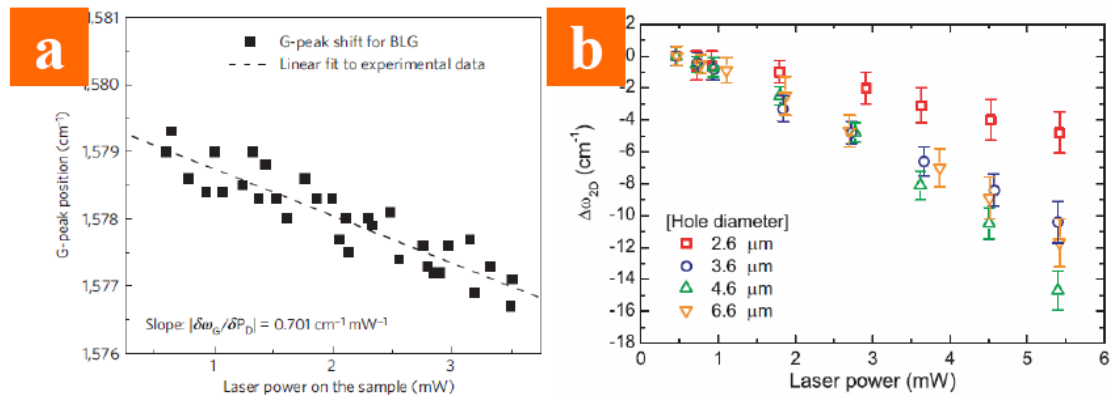
Figure 2.8: (a) Experimental data for Raman G-peak position as a function of laser power, which determines the local temperature rise in response to the dissipated power [18]. (b) Shift of the Raman 2D band as a function of the laser power [69].

Secondly, the measured thermal conductivity value depends linearly on the percentage of the laser power absorbed by the graphene. Although various types of

calibrations are done by the experimentalists, there is still a wide variation of values being used in different reports ranging from 2.3% to 13% [14, 16, 69, 70], resulting in large disagreement in the reported room temperature values of κ of graphene.
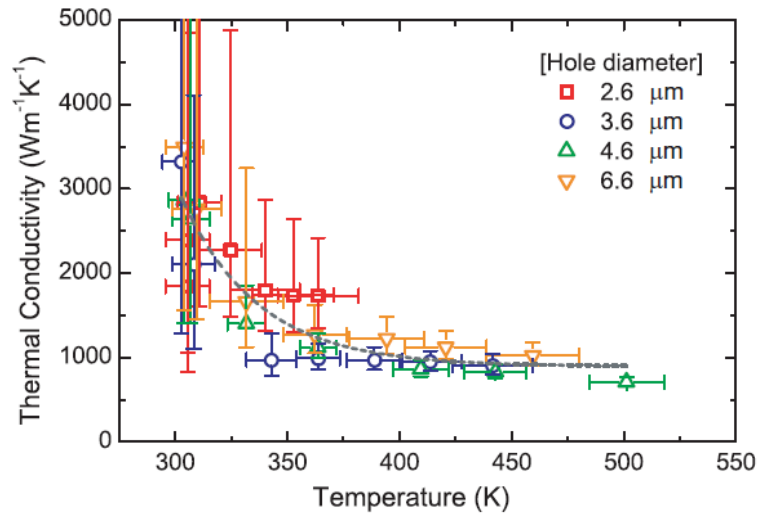
Figure 2.9: Thermal conductivity of suspended graphene as a function of measured temperature. The dotted curve is guide to eye [69].
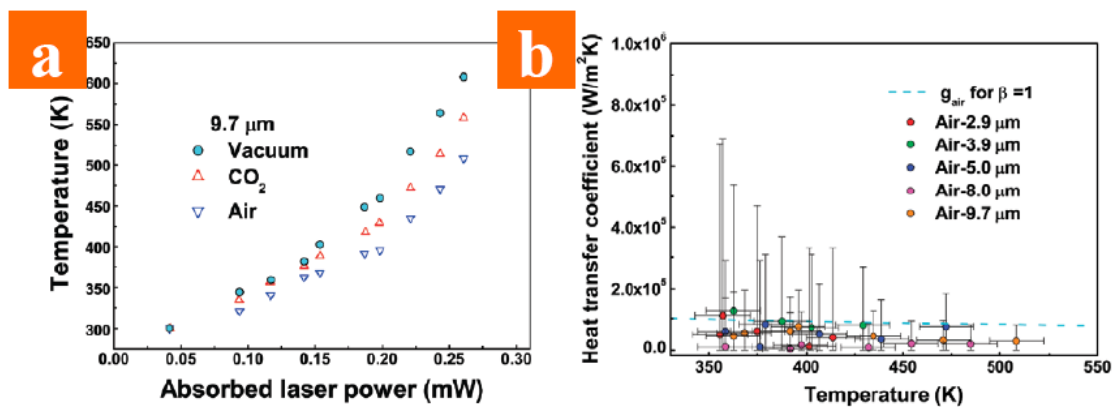
Figure 2.10: (a) The 2D peak shift measured at the center of the suspended graphene as a function of the absorbed laser power for a 9.7 μm diameter suspended graphene sample in vacuum, CO_2, and air. (b) Gas heat transfer coefficient as a function of the measured temperature of graphene suspended over holes of various diameters in air. Shown in comparison are the maximum thermal boundary conductance values calculated from the kinetic theory [70].

Lastly, most Raman systems are limited to operate under ambient conditions, thus the thermal transport of graphene in the low-temperature range that is useful for understanding its fundamental physics cannot be studied. Even the region near room temperature has very large error bars, as shown in Figure 2.9. In addition, the heat

loss through the convection of ambient air is quite significant as shown in Figure 2.10. For a 9.7 μm diameter SLG sample measured in ambient air, if this heat loss to the surrounding gas is ignored, the thermal conductivity value obtained will be 14 – 40% higher than that measured in vacuum [70], thus the parasitic heat loss causes substantial errors in the obtained κ. Carrying out measurements under vacuum conditions can eliminate this uncertainty, but the modification of the Raman system is not something easily achievable in most labs.

Although the micro-Raman technique offers a very convenient way for the thermal measurements of graphene, it cannot be used for rigorous investigations of the fundamental physics due to the limited temperature range and the poor accuracy. In view of this, researchers start to show interest in the thermal-bridge configuration that has been successfully employed in the studies of graphene's 3D (graphite) and 1D (CNT) allotropes.
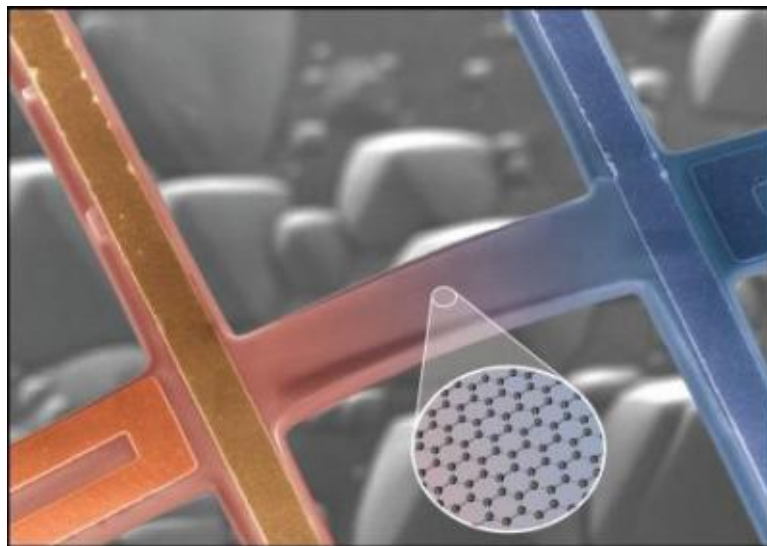
Figure 2.11: SEM image (in false colors) of a single layer graphene (SLG) on a thermal-bridge test device [11].

The thermal-bridge method is very similar to those used in studying CNT. As shown in Figure 2.11, the graphene flake is placed between two temperature sensors, and the entire system is suspended by long beams for thermal isolation. A known

amount of heating power is injected on the left-hand-side by Joule heating to establish a temperature gradient across the graphene flake. The temperature at the two ends of graphene is accurately determined from the electrical resistance of the sensors. From the heating power and the temperature difference values, the thermal conductance of the sample can be calculated.

This conventional configuration has high temperature sensitivity and allows measurements at low temperatures in vacuum. However, the sample preparation is extremely difficult especially in the assembly of graphene between the two suspended micro-thermometers. As the atomically thin flake of graphene is fragile and prone to crumpling, the direct nano-manipulation method described previously for CNT is not applicable. Two different processes have been developed to fabricate such samples.
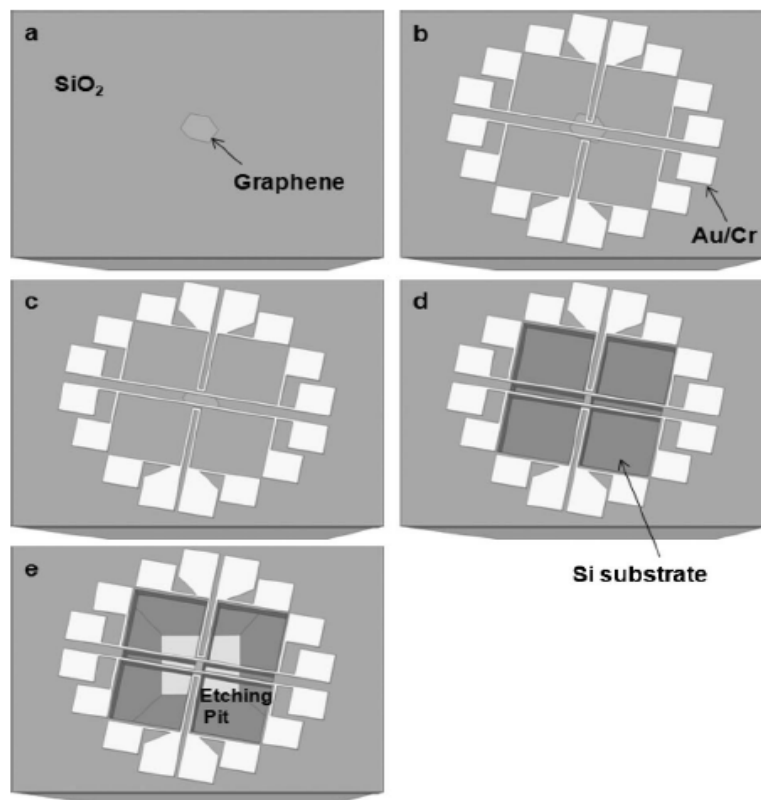
Figure 2.12: Schematic diagram of the fabrication process. (a) A graphene flake was exfoliated on a 300-nm-thick SiO_2 film thermally grown on a Si wafer. (b) Au/Cr RT lines were patterned with the use of EBL and metal lift-off. (c) The graphene was patterned using EBL and oxygen plasma etching so that only the part of graphene flake between the two inner straight RTs was left after patterning. (d) Windows in the SiO_2 layer were patterned and etched to form Au/Cr/SiO_2 beams and graphene/SiO_2 beams. (e) The device was suspended by etching the underlying silicon substrate in a TMAH solution. All schematics are not to scale [71].

17

The first is a top-down process [71]. Graphene is mechanically exfoliated on the standard SiO_2/Si substrate, and a series of photolithography, EBL, metallization and etching steps are used to align the electrical circuit, pattern the graphene and release the suspended structure, as shown in Figure 2.12. One limitation is that this structure is only applicable to supported graphene samples.

The other is a transfer process [72]. Graphene is mechanically exfoliated on a Si substrate coated with a 90 nm thick polymethyl-methacrylate (PMMA) layer, which allows optical identification of the flakes just like the SiO_2/Si substrate. The pre-fabricated thermal test structure is aligned to the graphene with the top-side down, and attaches to it with the help of a drop of isopropyl alcohol (IPA). After electron beam exposure of PMMA near the two central thermometers, the device is wetted in methyl isobutyl ketone (MIBK) and acetone to release the entire suspended structure, as shown in Figure 2.13.
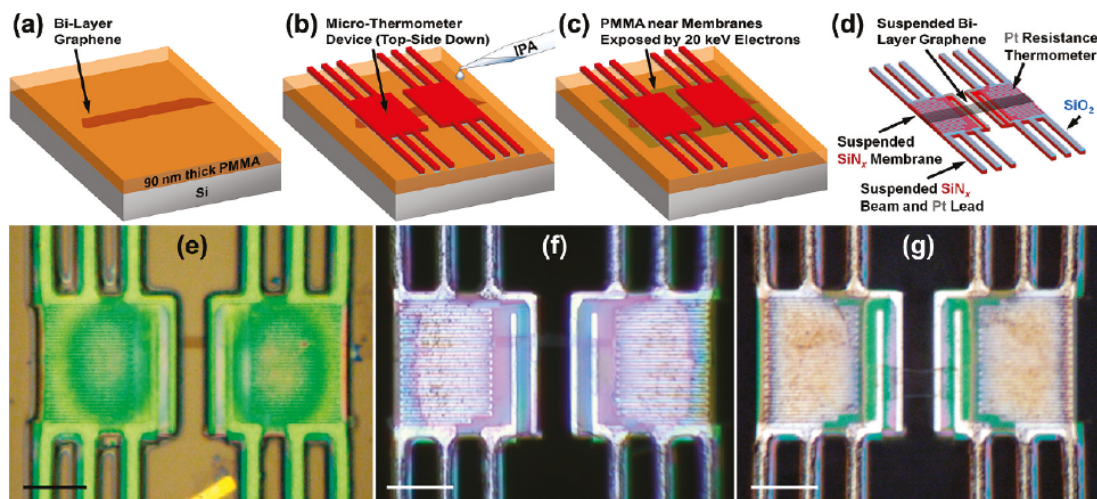
Figure 2.13: Schematic of the bilayer graphene (BLG) transfer procedure showing (a) exfoliation of BLG onto PMMA on Si, (b) attachment and alignment of microresistance thermometer device to BLG with the help of a drop of isopropyl alcohol, (c) electron beam exposure of PMMA near the two central membranes, and (d) BLG suspended between two microthermometers after wetting in methyl isobutyl ketone and acetone. (e) Optical micrograph of bilayer graphene sample BLG_1 corresponding to (b), and final suspended BLG sample (f) BLG_1 and (g) BLG_2 corresponding to (d). Scale bars in (e – g) are 10 μm [72].

In summary, the thermal-bridge method provides excellent accuracy in the measured data and flexibility in the experimental parameters, but the sample is subject to possible damage or contamination during the lithography and etching processes; whereas the micro-Raman method offers a fast and convenient way to examine the thermal conductivity of pristine graphene, but with fairly poor accuracy and little control of the environmental conditions. One has to practice caution when comparing results acquired from different methods.

2.3.2 Phonon contribution and temperature dependence of κ

Similar to other semiconductors, for intrinsic or lightly-doped graphene, its thermal conduction is dominated by phonons. As shown in Figure 2.14, the optical phonons contribute little to the thermal conductivity compared to the acoustic phonons [15], especially in the normal temperature range of interest below 500 K. Hence most of the heat is carried by the three acoustic branches, namely the in-plane transverse (TA) and longitudinal (LA) modes, and the out-of-plane transverse (ZA) mode.

In the earlier theoretical works, the ZA mode or the flexural mode is ignored in the calculation of graphene's thermal conductivity, due to their low group velocity and high Gruneisen parameter γ [73-75]. Based on a relaxation time approximation (RTA) model [73, 76], the ZA contribution is negligibly small due to large Umklapp scattering rate (τ_u^{-1}). However, the expression derived for τ_u^{-1} has large uncertainty due to the assumptions in the three-phonon scattering phase space that is not explicitly calculated [77]. Full quantum mechanical calculations of both normal and Umklapp scattering processes in SLG are carried out to address the issue. A selection rule is obtained for the three-phonon Umklapp scattering which requires an even number of

ZA phonons in each process as a consequence of the reflection symmetry in flat 2D SLG. The selection rule forbids 60% of the three-phonon scattering phase space of ZA phonons.
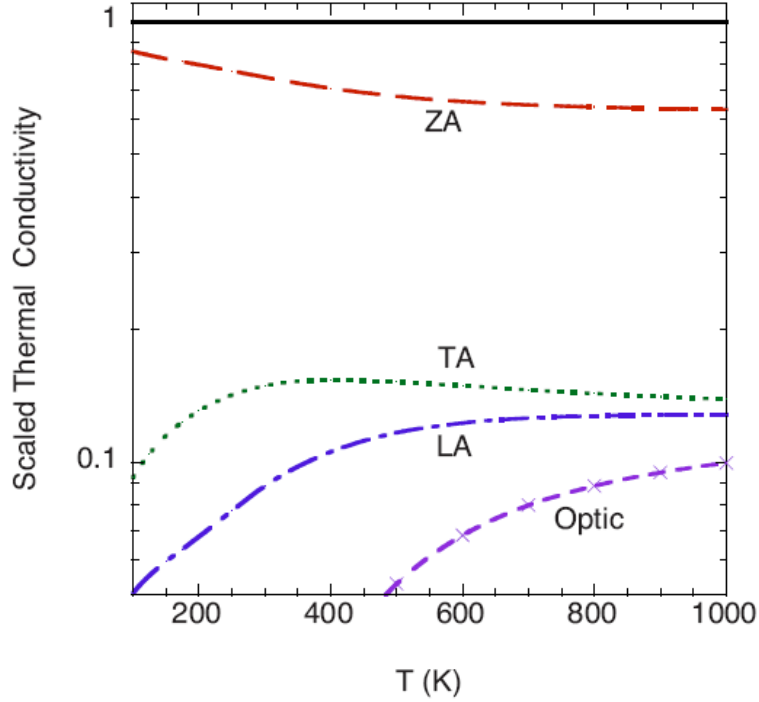
Figure 2.14: κ_{ZA} (red dashed), κ_{TA} (green dotted), and κ_{LA} (blue dash-dotted) and the combined contributions from the optic branches (dashed purple with crosses) as a function of temperature for L=10 µm. Values are scaled by $\kappa_L(T)$ (horizontal black line) [15].

In addition, the ZA branch in graphene has quadratic phonon dispersion over a wide range of the 2D Brillouin Zone (BZ): $\omega_{ZA}(q) = \alpha_{ZA}q^2$, where ω_{ZA} is a positive constant and q is the 2D phonon wave vector. The corresponding density of phonon modes, $D_{ZA}(\omega) = 1/(4\pi\alpha_{ZA})$, is also constant. The average number of phonons per unit ω is $N(\omega) = n^0(\omega)D(\omega)$, where $n^0(\omega)$ is the Bose distribution function. Here $N_{ZA}(\omega)$ diverges as $1/\omega$ for $\omega \to 0$. The in-plane branches have linear dispersion, $\omega_{in}(q) \approx v_{in}q$ with $D_{in}(\omega) = \omega/(2\pi v_{in}^2)$, and $N_{in}(\omega) \to$ constant for $\omega \to 0$. Hence the ratio $N_{ZA}(\omega)/N_{in}(\omega) = v_{in}^2/2\alpha_{ZA}\omega$ diverges as $\omega \to 0$, i.e., the ZA branch has a much higher density of phonons than the in-plane branches due to its quadratic

dispersion. Furthermore, the ZA group velocity at diminishingly small wave vector q approaches half of that of LA and TA branches and is far from negligible. Through an exact numerical solution of the phonon Boltzmann transport equation (BTE), the thermal conductivity of graphene is found to be dominated by the ZA mode at all temperatures [15], which contributes as much as 77% and 86% of the total κ at 300 K and 100 K respectively, as shown in Figure 2.14.
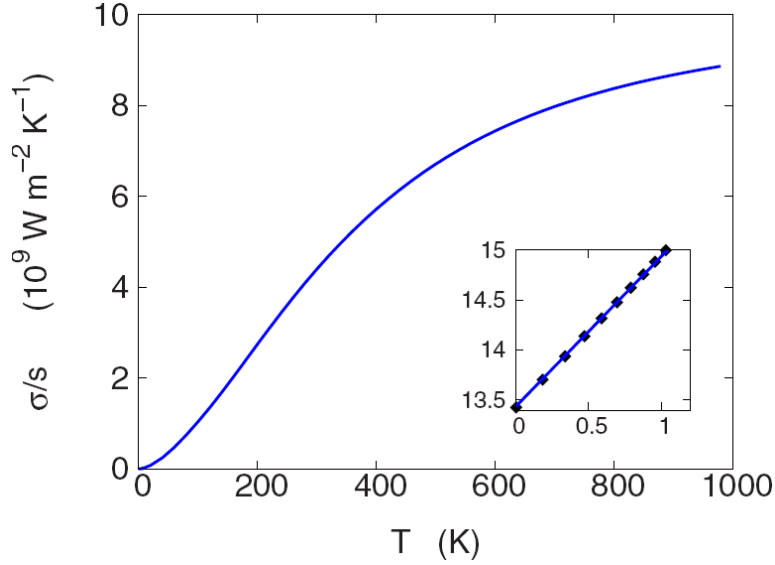
Figure 2.15: The thermal conductance of the graphene sheet vs temperature. Inset is log σ vs log T in extremely low-temperature region. The calculated results (filled squares) can be fitted by function (blue line). It indicates that the thermal conductance has a $T^{1.5}$ dependence in this region [13].

The temperature dependence of κ of graphene is first studied in the ballistic regime using the standard expression for the ballistic lattice thermal conductance $\sigma_b(T) = \int_0^\infty \Gamma(\omega)\hbar\omega(df/dT)d\omega/2\pi$, where $f(\omega, T)$ is the occupation distribution function for the heat carriers at the reservoirs, and the transmission function $\Gamma(\omega)$ is defined as the number of phonon branches at frequency ω. At low temperatures, the calculated κ of graphene has a $T^{1.5}$ dependence as shown in Figure 2.15, differs from the T^2 dependence expected for 2D acoustic phonon gases. This anomalous behavior is attributed to the quadratic dispersion of the ZA mode, whose transmission function

at low frequency is $\Gamma(\omega) \simeq \int_{-q(\omega)}^{q(\omega)} (D/2\pi)dq = (D/\pi)\sqrt{\omega/\alpha}$. Since the ZA mode dominates the heat transfer especially at low temperatures, $\sigma_b \sim T^{1.5}$ [11].

As T increases, the phonon-phonon Umklapp scattering becomes stronger as higher energy phonons are thermally populated [38], and the ballistic assumption is no longer appropriate. Typically $\kappa \sim T^{-1}$ at elevated temperatures where Umklapp scattering dominates over other static scattering processes. In this region, the $\kappa - T$ relation is very similar to those obtained for CNT and high-quality graphite, as shown in Figure 2.16.
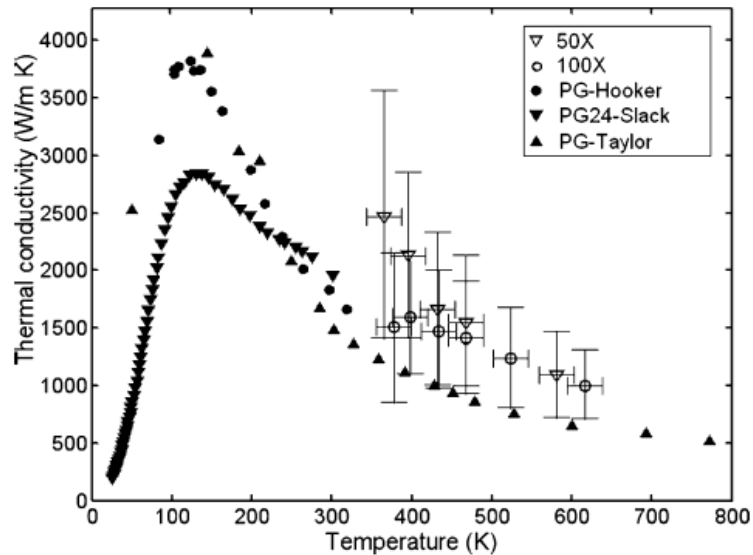
Figure 2.16: Thermal conductivity of the suspended CVD graphene measured using 100× and 50× objective lens as a function of the measured graphene temperature. Also shown in comparison are the literature thermal conductivity data of pyrolytic graphite samples as a function of temperature [17, 70].

2.3.3 Substrate effect

While suspended graphene is ideal for studying its intrinsic properties, in a practical perspective, graphene devices are always supported on a substrate. The effect of substrate on the thermal transport of graphene was first studied by Seol *et al.* using a thermal-bridge configuration [19]. The room temperature thermal conductivity measured for supported SLG is only 600 Wm^{-1}K^{-1}, significantly lower than that for

suspended SLG, which ranges from 1800 $Wm^{-1}K^{-1}$ to 5000 $Wm^{-1}K^{-1}$ [14, 69, 70, 74] depending on individual sample preparation and measurement setup. The significant reduction in κ in the presence of a substrate is attributed to the suppression of the flexural mode. As the supported graphene partially conforms to the surface roughness of the underlying substrate, phonons leak across the graphene-support interface and flexural phonons are strongly scattered. By considering Van der Waals (VdW) force constant between graphene and the substrate for LA, TA and ZA polarizations, the contribution of different branches was calculated and is reproduced in Figure 2.17. It clearly demonstrates that the ZA phonons dominating the heat transfer in suspended graphene are strongly suppressed in supported graphene. Therefore, the presence of a substrate significantly reduces the measured thermal conductivity of graphene due to interface scattering.
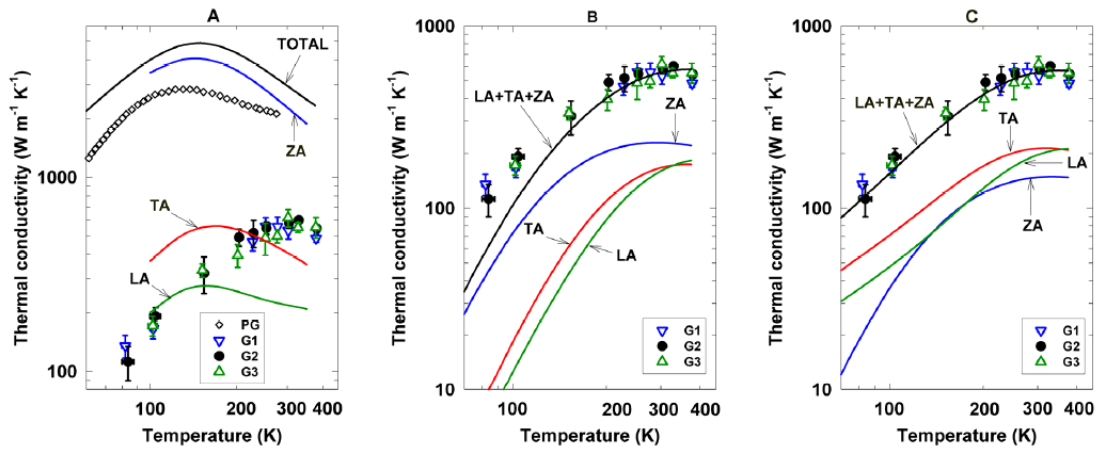
Figure 2.17: Thermal conductivity and the contributions from different acoustic branches obtained by the BTE calculation for suspended and supported SLG with specular edges in comparison with experimental results of supported SLG and PG. (A) Suspended SLG. (B) Supported SLG with $d = s = 30$ nm, $K_{ZA} = K_{LATA} = 0.46$ N/m. (C) Supported SLG with $d = s = 30$ nm, $K_{LATA} = 0$, and $K_{ZA} = 0.73$ N/m [19].

Nevertheless, it is intuitive that for multi-layer graphene, the effect of the substrate scattering will only penetrate the nearest few layers. The exact penetration depth was investigated using a heat spreader configuration as shown in Figure 2.18. Graphene flakes of different thicknesses were encased between SiO_2 layers, and their

in-plane thermal conductivities were extracted by fitting the temperature profile T_1, T_2 and T_3 with a numerical model [78].
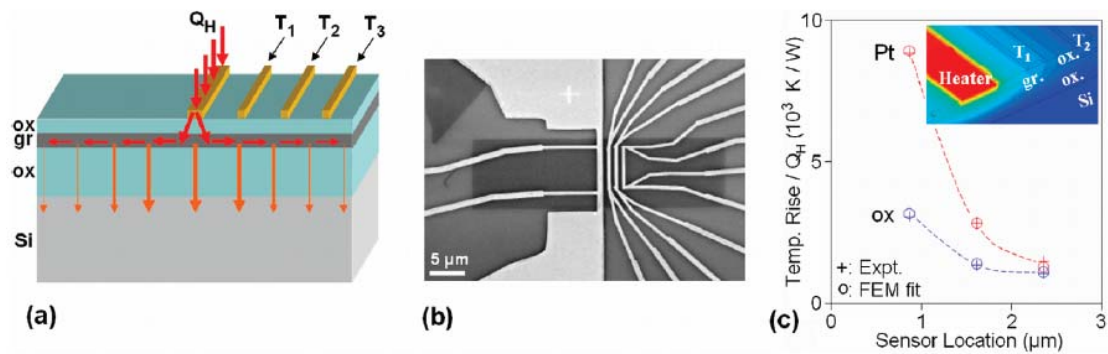
Figure 2.18: (a) Schematic of the heat spreader method. Heat flows (red arrows) through the encased graphene and into the Si heat sink. (b) Top-view SEM image of one of the devices used in this work, including heater and three T sensors (white) and trimmed graphene flake (dark rectangle). An additional triangular flake can be seen in the upper-left corner. (c) Temperature profiles normalized to the heater power Q_H for validation experiments using oxide (blue) and a Pt film (red). κ is extracted by fitting the experimental data (crosses) with the FEM model (circles), resulting in $\kappa_{ox} = 1.43$ W/m-K and $\kappa_{Pt} = 25.4$ W/m-K. Dashed lines are to guide the eye. Inset: Detail of a typical 3D FEM simulation [78].
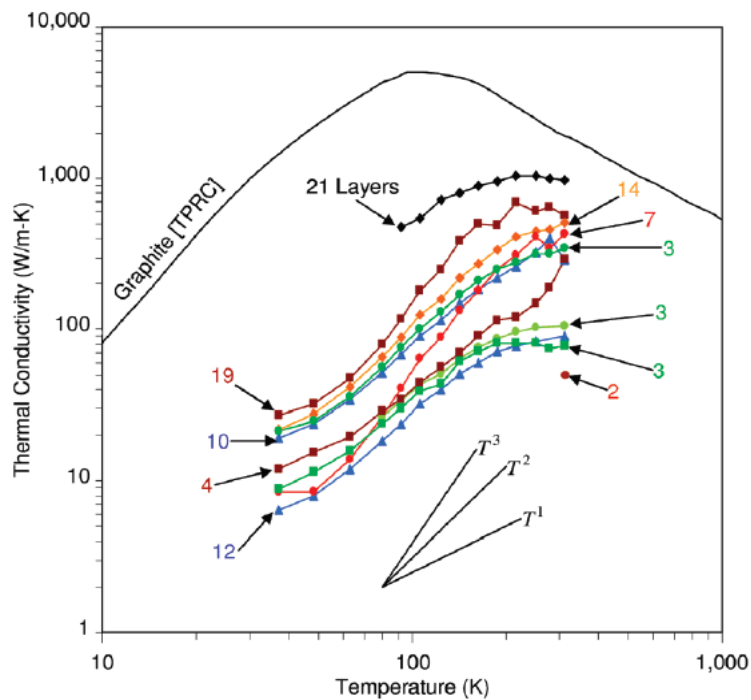
Figure 2.19: Temperature dependence of κ for encased graphene and ultrathin graphite [78].

For SLG, the measured value of κ is lower than 160 $Wm^{-1}K^{-1}$, showing strong phonon leakage and scattering at the graphene-oxide interfaces. κ increases with the number of graphene layers and approaches that of bulk graphite for the thickest flake

24

as shown in Figure 2.19. As the thickness increases, the core layers away from the oxide are shielded and experience diminishing influence of the interfaces. In addition, the defect density in the outer layers may be higher due to the SiO_2 deposition process. By fitting the data using a semi-empirical relation between the measured thermal conductivity and the exponential decay length of the interface scattering, the disruption effect of the thermal transport due to the encasing oxide penetrates a characteristic distance of approximately 2.5 nm or 7 graphene layers. Therefore, from a device point-of-view, especially when using ultrathin graphite as thermal components in integrated circuits, the layer thickness should target at least 10 nm to maximize κ.

2.3.4 Size dependence

Unlike bulk graphite, theoretical calculations have shown that the thermal conductivity of graphene strongly depends on its lateral size (with length L defined parallel to the direction of thermal conduction, and width W perpendicular to it). Even before graphene had been isolated, Klemens [79, 80] had compared the heat transport in basal planes of graphite and in SLG. The former can be treated as a 2D system till a certain low-bound cut-off phonon frequency ω_C. Below ω_C the cross-plane coupling is very strong and heat starts to propagate in all directions, hence the contribution of these phonon modes in the basal plane heat transport is negligible. Following the spirit, Nika *et al.* [73] found that the low-bound cut-off frequency for a given phonon branch $\omega_{min} \sim L^{-1/2}$ since the phonon mean free path (MFP) cannot exceed the physical size of the SLG. Therefore, a larger L allows a larger interval of phonons to participate in heat conduction. In other words, in larger graphene flakes, acoustic phonons with longer wavelength are available for heat transfer, thus giving a higher κ.
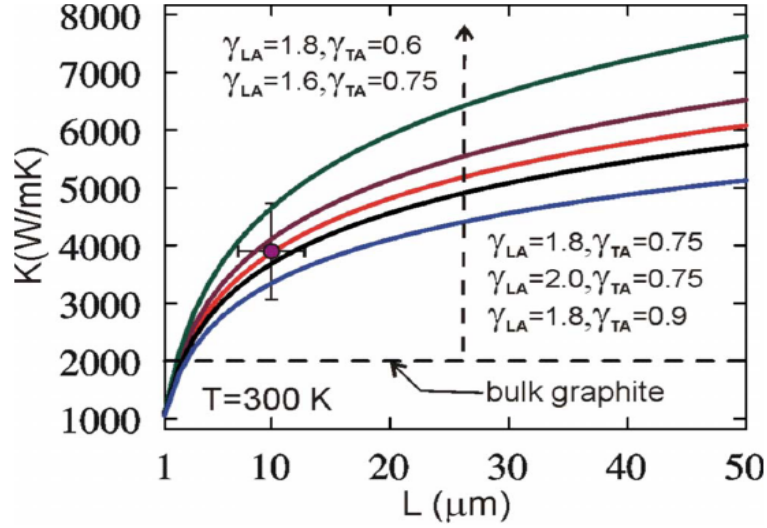
Figure 2.20: Thermal conductivity of graphene as a function of the graphene flake size L. Note that the thermal conductivity of graphene exceeds that of basal planes of graphite when the flake size is larger than few micrometers [73].
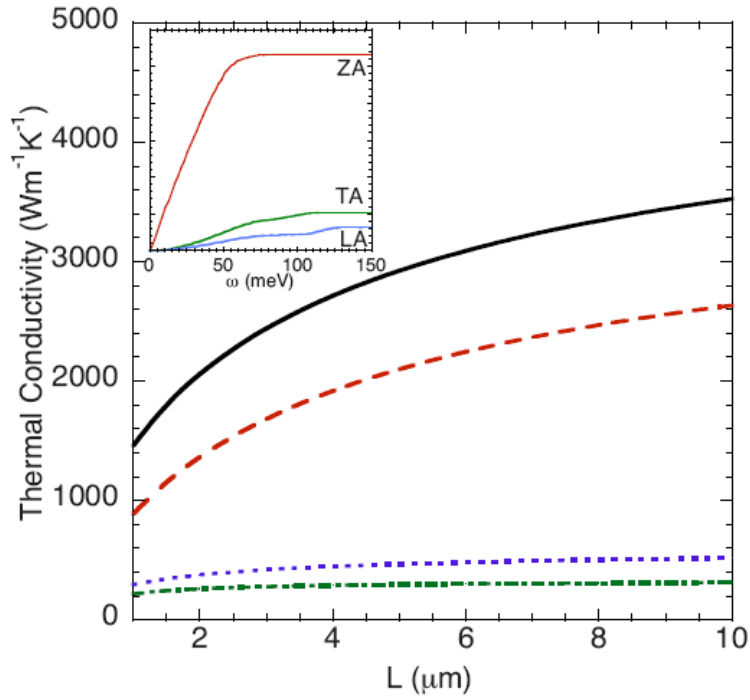
Figure 2.21: Calculated κ_L at T = 300 K as a function of the sheet length, L, along the transport direction (black solid curve). Also shown are κ_{ZA} (red dashed), κ_{TA} (blue dotted), and κ_{LA} (green dash-dotted) acoustic branches. Inset shows the total contribution to each branch as a function of phonon frequency. Units are also in $Wm^{-1}K^{-1}$. Saturated values for large ω correspond to $\kappa_{ZA} \approx 2600\ Wm^{-1}K^{-1}$, $\kappa_{TA} \approx 520\ Wm^{-1}K^{-1}$, and $\kappa_{LA} \approx 315\ Wm^{-1}K^{-1}$ [15].

As shown in Figure 2.20, the size dependence of κ is rather strong for small

flakes and weakens gradually for larger flakes. Lindsay *et al.* [15] considered the

contribution from the three acoustic branches individually by solving their phonon

BTE, and a similar relationship between κ and L was obtained and is shown in Figure

2.21. This agrees with many recent theoretical studies [47, 49, 81-83], which suggest

that the intrinsic thermal conductivity of 1D and 2D anharmonic crystals is anomalous

and diverges with the size of the system defined by either the number of atoms N or

linear dimension L. This anomalous behavior of κ is often termed as breakdown of

Fourier's law [49], and leads to $\kappa \sim \ln(N)$ in 2D [81].

2.3.5 Interlayer interaction
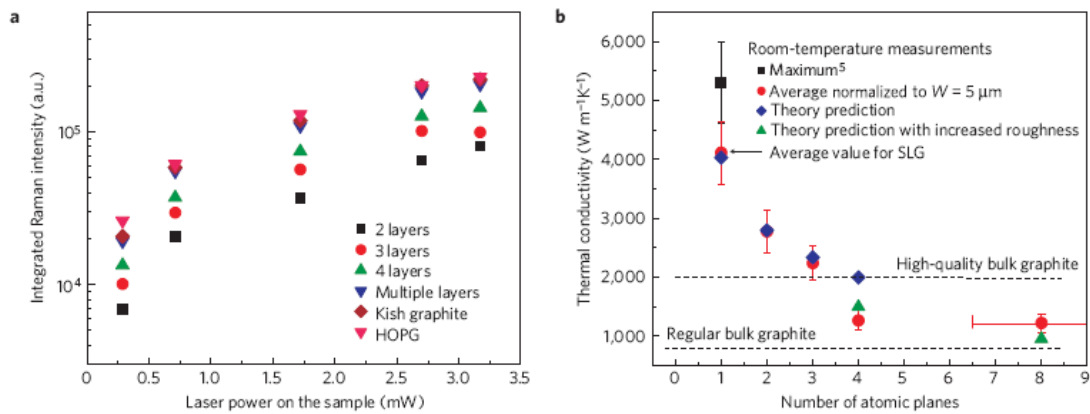
Figure 2.22: Experimental data. (a) Integrated Raman intensity of the G peak as a function of the laser power at the sample surface for FLG and reference bulk graphite (Kish and highly ordered pyrolytic graphite (HOPG)). The data were used to determine the fraction of power absorbed by the flakes. (b) Measured thermal conductivity as a function of the number of atomic planes in FLG. The dashed straight lines indicate the range of bulk graphite thermal conductivities. The blue diamonds were obtained from the first-principles theory of thermal conduction in FLG based on the actual phonon dispersion and accounting for all allowed three-phonon Umklapp scattering channels. The green triangles are Callaway–Klemens model calculations, which include extrinsic effects characteristic for thicker films [18].

The intrinsic properties of SLG are in many ways different from its 3D form,

and it is interesting to know when and how the 3D to 2D crossover happens as the

thickness of the graphite decreases towards monolayer. Ghosh *et al.* [18] investigated

the interlayer interaction with a micro-Raman setup. Graphene samples similar to that

in Figure 2.7 are prepared with different thicknesses. Using the method described in

Section 2.3.1, the room temperature thermal conductivity of graphene was measured and plotted against the number of atomic planes, as shown in Figure 2.22. It is clear that the value of κ decreases as the thickness increases, and intersects that of high-quality bulk graphite at ~4 atomic planes.

In conventional thin film whose thickness is less than the phonon mean free path, thermal transport is dominated by phonon-rough-boundary scattering, and κ scales down with decreasing thickness. In graphene, the thickness dependence of κ is opposite, partly because there are little random thickness fluctuations and cross-plane velocity component in the ultrathin FLG. Instead of scattering at the top and back surfaces, the dominant mechanism limiting κ is the Umklapp scattering caused by crystal anharmonicity. Compared to SLG, although the number of available phonon branches (heat conduction channels) in bilayer graphene doubles, the q phase space available for Umklapp scattering increases even more, resulting in a reduction of κ. Based on first-principles calculations of the phonon dispersion, and considering all allowable Umklapp processes through extension of the diagram technique developed for SLG [84], the room temperature κ of graphene is expected to decrease for thicker flakes, consistent with the experimental observation. Therefore, the change in thermal conductivity from graphite to SLG is attributed to the fundamental properties of 2D systems such as the phonon dispersion relation.

2.3.6 Static scattering sites: edges, defects and isotopes

In most theoretical studies, graphene is assumed to have a perfect lattice to reduce the complexity of the calculations. However, there are many static scattering sites present in graphene that may affect the thermal transport, such as rough edges, point defects and ^{13}C isotopes [85-87].

In relatively large SLG (L, $W > 5$ µm), the phonon scattering from the rough edges is evaluated using the Ziman equation [33]: $\dfrac{1}{\tau_{edge}} = \dfrac{v}{W}\dfrac{1-p}{1+p}$, where $\dfrac{1}{\tau_{edge}}$ is the edge-limited phonon relaxation rate, v is the phonon group velocity, W is the width of the graphene flake and p is the specularity parameter which depends on the roughness of the edges. Here $p = 0$ corresponds to the perfectly diffusive phonon scattering and $p = 1$ corresponds to the perfectly specular scattering (ideal case). This relaxation rate is negligible compared to that of Umklapp processes for smooth edges, but becomes significant as the edge roughness increases. Since the total phonon relaxation rate is given by $\dfrac{1}{\tau_{total}} = \dfrac{1}{\tau_{edge}}\dfrac{1}{\tau_{umklapp}}$, for rougher edges with a smaller p, there is a significant reduction in κ, as shown in Figure 2.23(a).
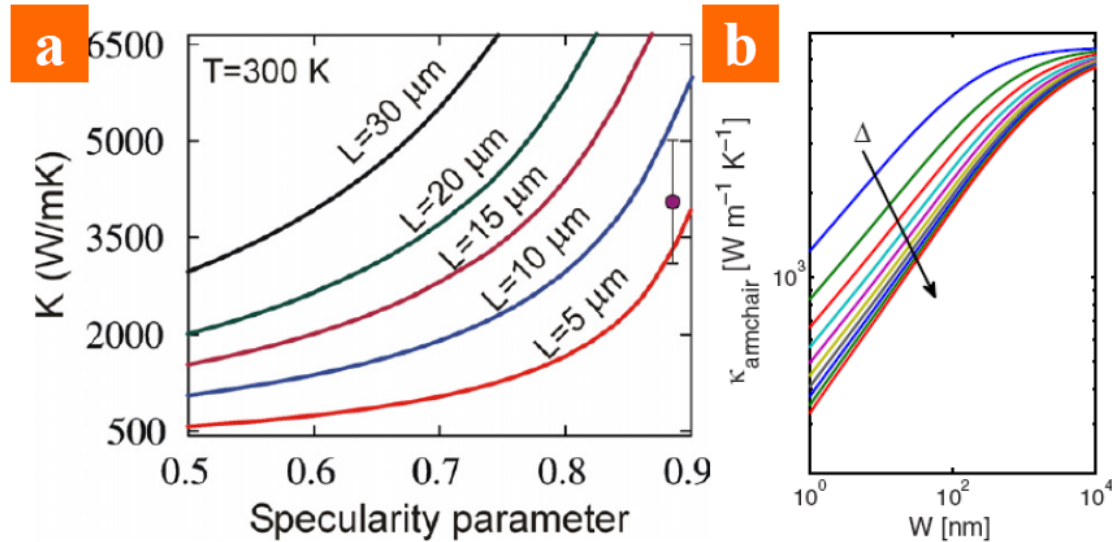
Figure 2.23: (a) Calculated thermal conductivity of the suspended graphene as a function of the specularity parameter p for the phonon scattering from the flake edges. Note a strong dependence on the size of the graphene flakes [88]. (b) Dependence of the room temperature thermal conductivity of armchair GNRs on the GNR width. The rms roughness Δ of the nanoribbon edges was varied from 0.1 to 1 nm in 0.1 nm steps; the direction of increasing Δ is indicated by the arrows. Thermal conductivity decreases with decreasing width W and increasing roughness Δ due to the stronger diffuse scattering with the rough edges [89].

For graphene nanoribbon (GNR) whose width W is comparable to or smaller than the phonon MFP, the edge effect is more dominant, as shown in Figure 2.23(b),

where the edge roughness is quantified by the root-mean-square (rms) value Δ. As the presence of line edge roughness in narrow GNR affects the thermal transport very strongly [84, 88] while leaving electronic transport relatively unchanged [90], it has a very high thermoelectric figure-of-merit ZT [90], making it an promising thermoelectric material.
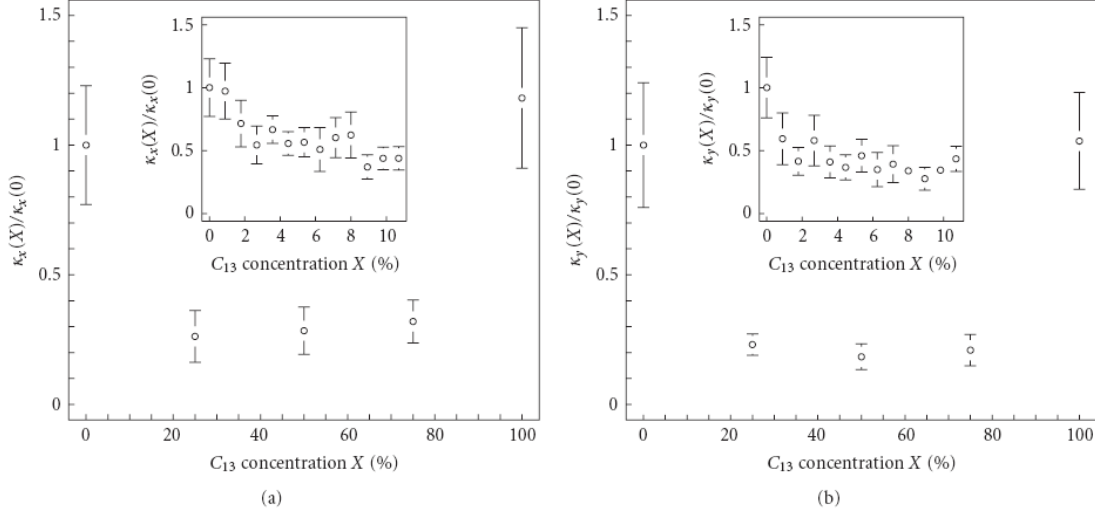
Figure 2.24: Normalized Graphene TC as a function of C_{13} concentration (a) TC in armchair direction (b) TC in zigzag direction. Inset shows TC as a function of C_{13} for low concentration. The normalizing factors κ_x and κ_y are the values for pure graphene, 630 Wm^{-1}K^{-1} and 1000 Wm^{-1}K^{-1}, respectively [91].

The scattering rate at point defects can be written as $\dfrac{1}{\tau_{pd}} = \dfrac{S_0 \Gamma}{4} \dfrac{q}{v} \omega^2$, where S_0 is the cross-section area per atom of the lattice and Γ is the measure of the strength of the scattering at the point defects. Because of the superior crystallinity of graphene, the majority of the defects are due to ^{13}C isotopes rather than impurities or vacancies. The natural abundances of ^{12}C and ^{13}C are 98.9% and 1.1%, respectively, and thus the effect of ^{13}C isotopic impurity is not manifested in most thermal measurements due to its low intrinsic density. In addition, point defects are not effective in scattering long wavelength phonons [92] that dominate the thermal conductivity of pristine graphene at low temperatures. Therefore, the isotopic effect is conveniently ignored in fundamental studies. Nevertheless, recently, it has been experimentally demonstrated

that different carbon isotopes such as ^{13}C can be controllably introduced in the chemical vapor deposition growth of graphene on metals. Both random distribution and segregation by domains of different isotopes have been observed [93]. When ^{13}C concentration increases, κ decreases and reaches a minimum at around 50%. The ^{13}C atoms with a different mass are efficient phonon scatterers and the phonon MFP is substantially shortened at ^{13}C concentration between 25% and 75%, as shown in Figure 2.24. In contrast, the electronic structure, and hence the electrical conductivity of graphene, are little affected by isotopes. Thus ZT can be easily improved by up to a factor of 5 as it is inversely proportional to κ, making this isotope engineering especially useful in GNR thermoelectric devices [94].

2.3.7 Contact thermal resistance

Before performing thermal measurements or making thermal devices, contacts need to be made at the boundary of graphene. Although the contact thermal resistance is not part of the graphene's intrinsic properties, it is of practical importance to understand its origin as well as its relative magnitude.

At the interface between graphene and contacts, due to the mismatch in the phonon spectrum, particularly in the acoustic branches, the propagation of phonon waves are impeded, resulting in a finite contact thermal resistance. Its magnitude can vary several orders of magnitude, depending on the contact material, the overlapping area, and the quality of the interface. Practically, the contact materials of interest are SiO$_2$ and metals commonly used for electrodes such as Au.

Contact thermal resistances between graphene or graphite basal plane and several common materials such as SiO$_2$, Au, Cr, Ti and Pt have been experimentally measured, which all give values in the order of 10^{-8} m^{2}KW^{-1} [17, 95-98]. As shown in

Figure 2.25 for a graphene-SiO_2 interface, the thermal resistance is between the theoretical values calculated by two different models, the "maximum transmission model" (MTM) and the elastic diffuse mismatch model (DMM). The MTM is a generalization of the "phonon radiation limit" [99] and sets the lower bound [100] of the thermal resistance, whereas the DMM is used for contact between isotropic and anisotropic materials [97, 101]. The thermal resistance shows no clear dependence on the graphene thickness, possibly because it is dominated by the single layer that is in direct contact with SiO_2.
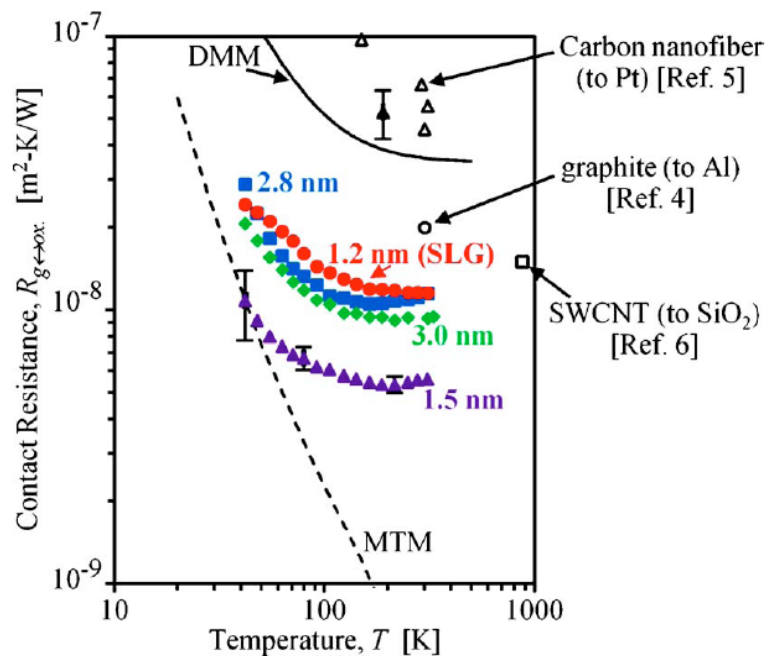
Figure 2.25: Experimental measurements of the thermal contact resistance between silicon dioxide and graphene, for four samples of different thicknesses as determined by AFM (filled points, in color). Also included for comparison are the contact resistances of several related carbon materials from the literature (open points), and theoretical curves for a DMM and a MTM (lines) [95].

For very thin and long graphene flakes, the contact thermal resistance from a nominal contact area of 1 μm^2 is several orders of magnitude smaller than that of the graphene itself, and has negligible impact on the heat conduction. However, it may be of concern when thicker and shorter graphene flakes are involved, or when the quality of contact between graphene and other materials is poor.

Chapter 3   Experimental Techniques

As reviewed in the previous chapter, thermal measurements of graphene are conducted in two approaches: the non-contact Raman technique, and the thermal-bridge technique using a top-down microfabricated device. The former provides limited accuracy in determining κ while the latter is only applicable to supported samples. In view of the drawbacks, we have developed a process to transfer and pattern graphene samples on a pre-fabricated MEMS device that incorporates thermal-bridge structures. This approach has two main advantages: it allows precise control over the size and shape of the graphene flake; and it can be used to measure both suspended and supported samples. This chapter describes the sample preparation process and the thermal measurement methodologies.

3.1   Sample fabrication
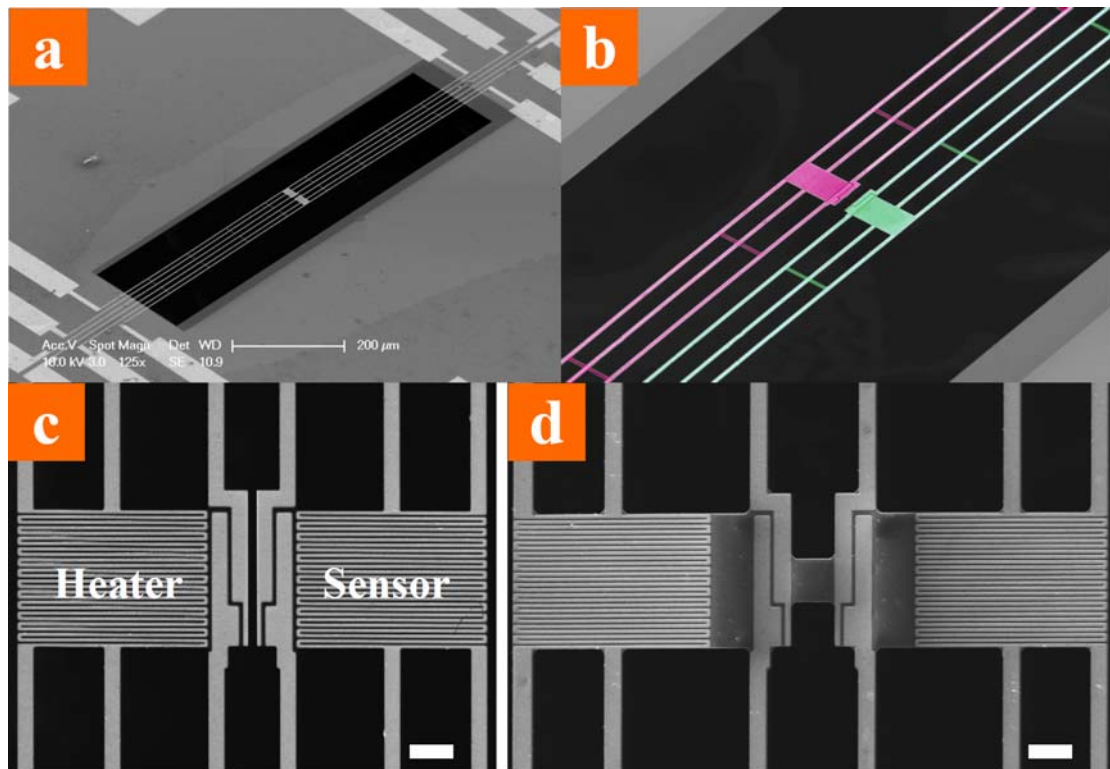
Figure 3.1: SEM images of the METS for (a – c) suspended and (d) supported samples; scale bar: 5 µm.

In this thesis, we adopted the thermal-bridge configuration for all the thermal measurements. The micro-electro-thermal system (METS) devices were fabricated in the Institute of Microelectronics (IME) following a process similar to that described by others previously [39]. Figures 3.1(a – c) and (d) show the scanning electron microscope (SEM) images of the METS used for measuring suspended and supported graphene, respectively. The METS consists of a 300 nm thick SiN_x layer as mechanical support and 60 nm thick Pt metallization on top for electrical connection. The *heater* and *sensor* labeled in Figure 3.1(c) each comprises a SiN_x island suspended by six long beams for thermal isolation from the bulk substrate, and the serpentine Pt loop on top acts as a resistance thermometer.

Flakes of single- (SLG) and few-layer graphene (FLG) were mechanically exfoliated on an oxidized Si substrate with 285 nm thick SiO_2. An optical microscope (Leica DM LM) with a 100 × objective lens was used to locate suitable flakes. The thickness of the graphene was primarily determined from its optical contrast, and Figure 3.2 shows an example of a flake with regions of different thicknesses.
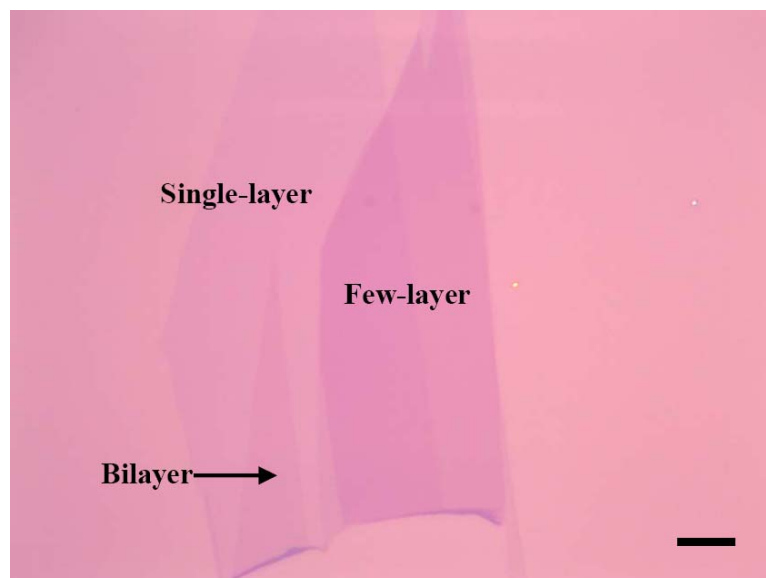
Figure 3.2: Optical image of a graphene flake with regions of different thicknesses; scale bar: 10 μm.

The optical method alone was convenient and reliable for identifying single-layer and bilayer graphene (BLG). For thicker FLG flakes, Raman spectroscopy was also performed using a green laser (532 nm) to provide supplementary information on the exact number of layers. As shown in Figure 3.3, the G-band near 1582 cm^{-1} is characteristic of a graphitic lattice; and single- to 5-layer graphene can be clearly distinguished by the FWHM value of the 2D-band near 2680 cm^{-1}, which is typically 20 times the layer number, i.e. ~20 for SLG, ~ 40 for BLG etc. up to 5 layers. The small D-band observed for the BLG in this example implies that there exists a considerable amount of lattice defects on the graphene basal plane, and such defective samples were discarded.
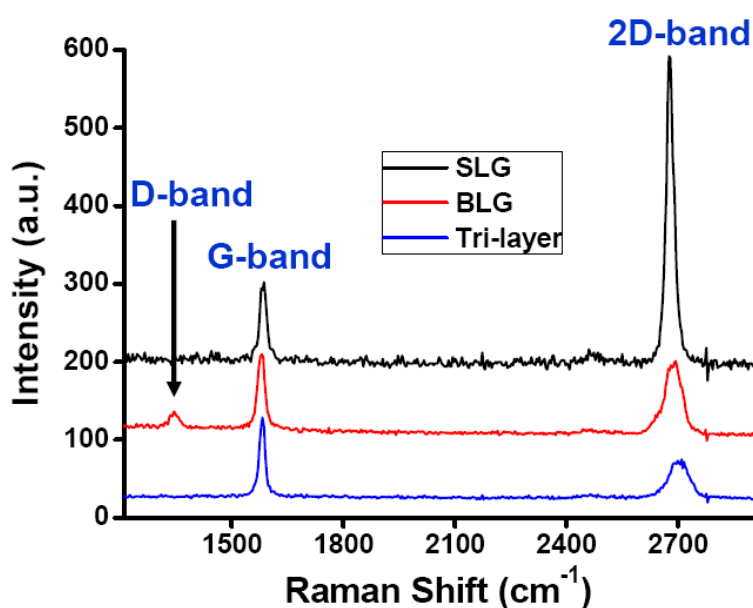
Figure 3.3: Raman spectra of a SLG, a BLG and a tri-layer graphene flake by using a 532nm laser.

We have developed a process to transfer suitable graphene flakes to the METS described earlier. The position of the flake was first noted with reference to the thick graphite pieces in the vicinity (Figure 3.4a). A 600 nm thick polymethyl-methacrylate (PMMA) layer was spin-coated on top (6 % PMMA solution spun at 6000 rpm for 1 min) and baked at 120 °C in an oven for 30 min to improve its adhesion with the

graphene. The substrate was then immersed in a 45 wt% KOH solution at room temperature for about 2 hours, and the PMMA membrane started to detach from the surface. The membrane was rinsed in de-ionized (DI) water and carefully transferred to a Petri dish filled with DI water. The METS was taped to the center of the Petri dish, and the membrane was placed on its surface.
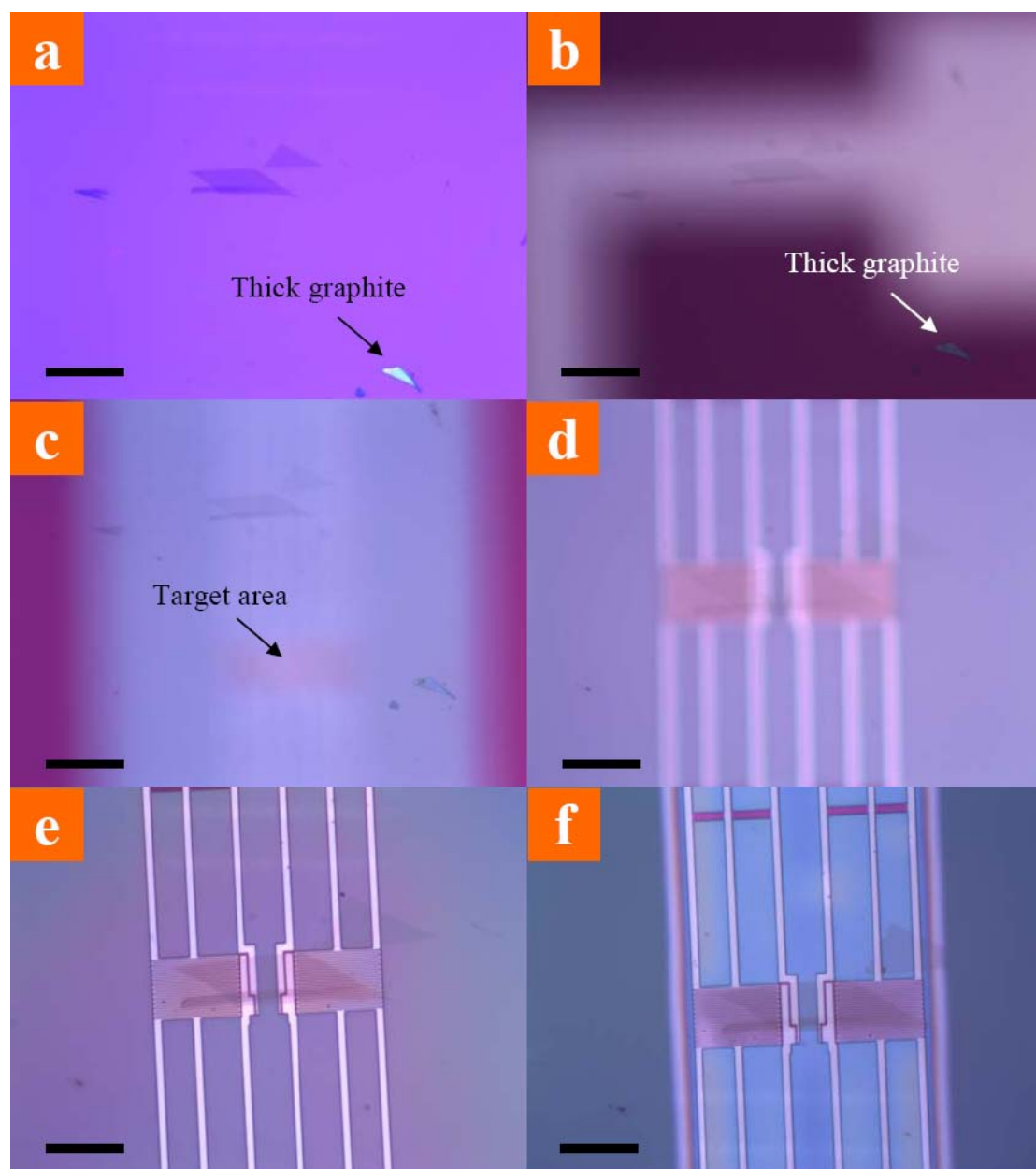
Figure 3.4: (a) Identifying a suitable FLG flake and noting its position with reference to a thick graphite piece. (b) Locating the flake underneath the PMMA membrane. (c) Moving the flake to the vicinity of the target area. (d) Aligning the flake to the target area. (e) Drying the sample naturally in air. (f) Flake successfully transferred onto the METS; scale bar: 10 μm.

The FLG flake on the underside of the PMMA was clearly visible under an optical microscope due to its optical opacity of approximately 2.3 % per layer (Figure 3.4b). The target flake was first identified and moved to the vicinity of the *heater*/*sensor* at lower magnification by the help of the thick reference graphite (Figure 3.4c), and was then slowly aligned to the test area by moving the very robust PMMA membrane with micro-manipulated probes. After the alignment (Figure 3.4d), the DI water in the Petri dish was emptied and the sample was left to dry naturally in air for 1 hour (Figure 3.4e). Due to the hydrophobic nature of PMMA, the FLG adhered very well to the surface of the METS upon drying (Figure 3.4f).
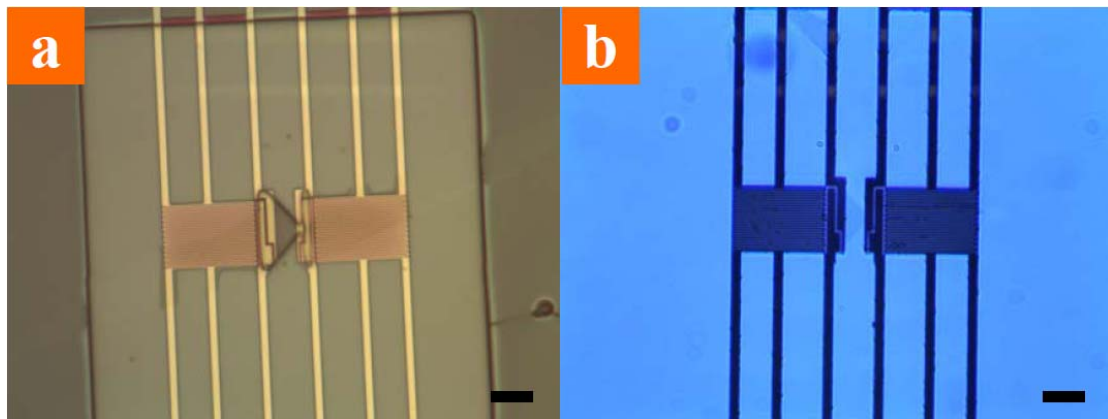
Figure 3.5: (a) Patterning the transferred FLG flake into desired shapes by EBL. (b) A suspended FLG sample on the released METS, ready for thermal measurements; scale bar: 10 μm.

The PMMA was removed by soaking in acetone for 10 min, leaving the FLG intact at the target position. Another 600 nm thick PMMA was spin-coated on the METS and baked at 120 °C for 15 min as a resist layer, followed by standard electron beam lithography (EBL) process to pattern the FLG into desired shapes (Figure 3.5a). The unwanted portion of the FLG was etched away in oxygen plasma (20 sccm O_2 flow, 0.4 mBar chamber pressure, 50 W power, 180 V substrate bias, and 1 min duration). The PMMA was again dissolved in acetone, and the METS with the aligned FLG flake was released by selective removal of the underlying Si substrate in

a XeF$_2$ dry etcher. The FLG sample was successfully suspended between the *heater* and *sensor* platforms (Figure 3.5b) and was ready for thermal measurements.
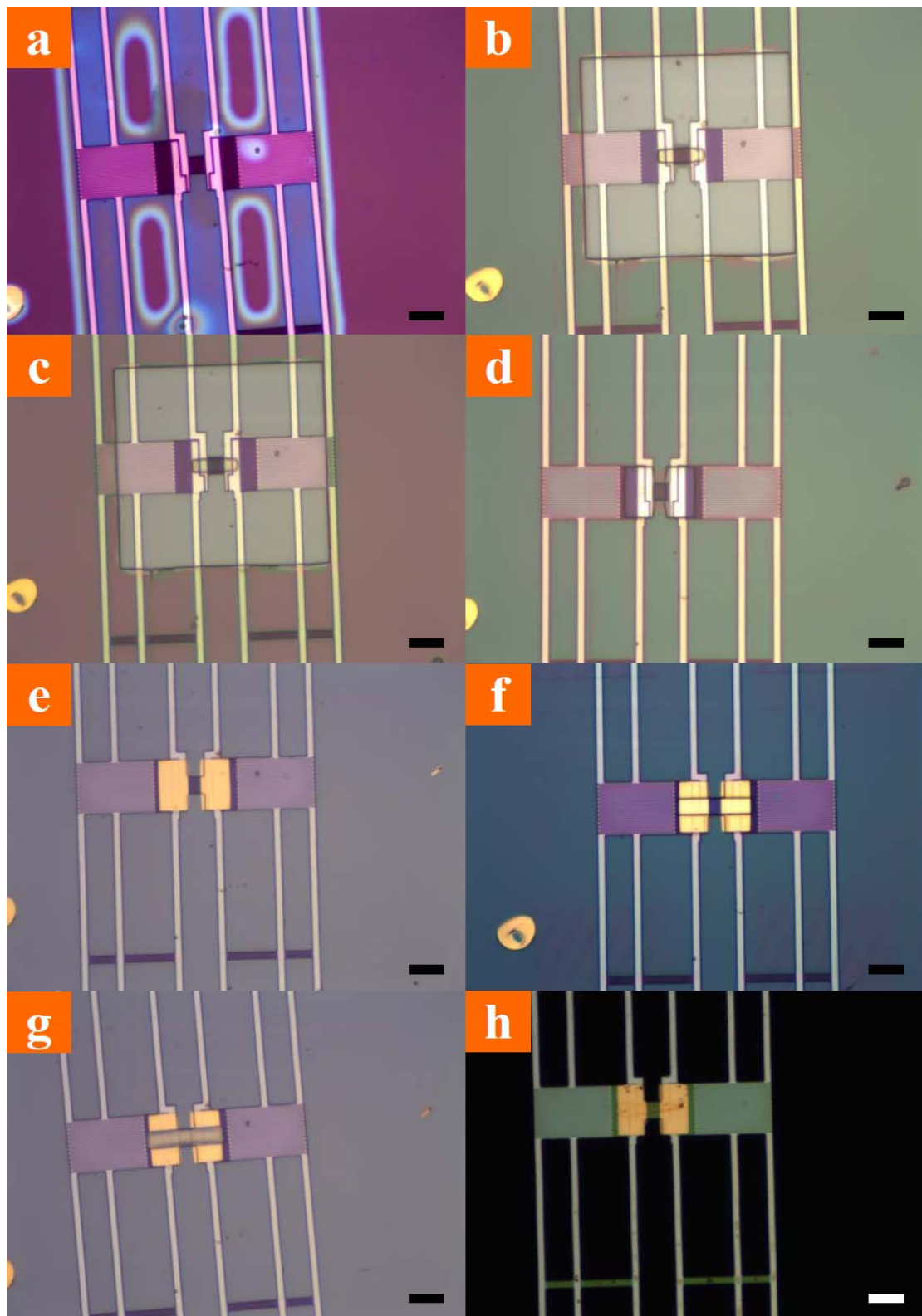
Figure 3.6: (a) – (c): Transfer and patterning of a FLG flake on the METS. (d) – (e): Defining and depositing Cr/Au contacts. (f) – (g): Defining and depositing Ni mask. (h): A supported FLG sample on the released METS, ready for thermal measurements; scale bar: 10 μm.

For supported samples, the fabrication process involved a few additional steps. The FLG flake was transferred onto the METS and etched into the desired ribbon shape in the same way as the suspended samples (Figure 3.6a – c). Windows were opened at the two ends of the graphene ribbon by EBL, followed by a metallization of Cr/Au (5/50 nm) (Figure 3.6d – e). This could improve its thermal contact with the *heater* and *sensor*, and also help in anchoring the FLG during the release of the METS. Another 70 nm thick layer of Ni was deposited on top to protect the FLG (Figure 3.6f – g), and the METS was immersed in a 45 wt% KOH solution at 80 °C for 45 min to be fully released. The Ni mask was then dissolved (Figure 3.6h) by soaking in a 1M solution of $FeCl_3$ for 15 min, and after rinsing and drying, the supported FLG sample was ready for characterization.

3.2 Measurement methodologies

3.2.1 Thermal measurements by a thermal-bridge method

We used a method similar to that described by Shi *et al*. [39] for the thermal measurements. A direct current I_h (typically $10 - 50$ μA) was passed through the *heater* loop (Figure 3.1a left) and a temperature gradient across the two ends of the sample was established due to Joule heating. The four-terminal electrical resistance of the *heater* Pt loop R_h was acquired using a lock-in amplifier by passing a very small alternating current $I_{lock-in}$ (500 nA, 2017 Hz) superimposed on I_h. The magnitude of $I_{lock-in}$ was only less than 5 % of I_h, thus the additional heating was negligible. The frequency $f_{lock-in}$ of $I_{lock-in}$ had to be carefully chosen. As shown in Figure 3.7a (red curve), we first measured R_h at room temperature with different values of $f_{lock-in}$. R_h decreases slightly at higher $f_{lock-in}$ due to capacitive coupling as the serpentine loops are densely packed together. R_h was measured again (blue curve) when a 10 μA dc

heating current was superimposed on $I_{lock-in}$, and it deviates from the original trend for $f_{lock-in}$ < 200 Hz. The difference between the two measurements is plotted in Figure 3.7b. The large ΔR_h at lower $f_{lock-in}$ is attributed to a strong coupling effect between $I_{lock-in}$ and I_h, which diminished at higher frequencies (> 500 Hz). Nevertheless, higher $f_{lock-in}$ would result in larger electrical noise from the parasitic capacitances in the lock-in system. A frequency of ~2000 Hz was found to give the best results. The electrical resistance of the *sensor* Pt loop R_s was obtained similarly, but the ac current used a slightly different frequency (500 nA, 1917 Hz) to avoid interference with the *heater* side.
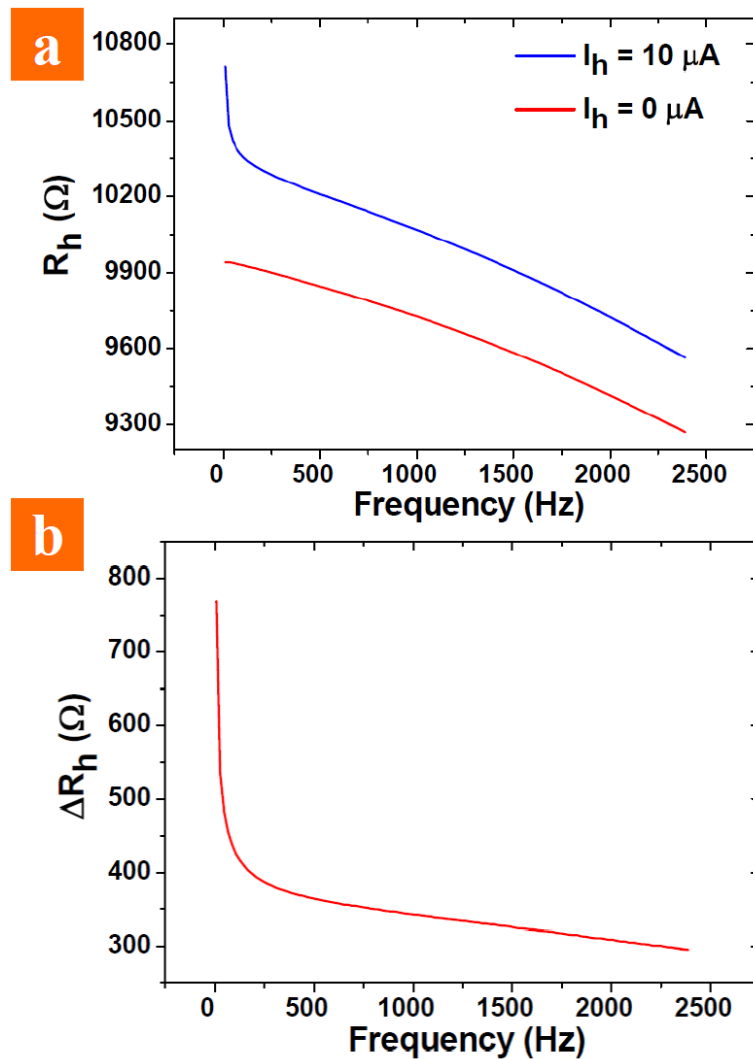
Figure 3.7: (a) Measured R_h as a function of $f_{lock-in}$ before and after applying a 10 μA dc heating current. (b) ΔR_h calculated from (a) as a function of $f_{lock-in}$.

The METS was placed on a feedback-controlled heater stage in the vacuum chamber, and the substrate temperature T_{sub} could be independently varied from 77 K (with a liquid nitrogen source) to 500 K (the heater stage limit) with a sensitivity of 0.01 K. By setting I_h to 0 and sweeping T_{sub}, the values of R_h and R_s were calibrated versus temperature at 20 K intervals as shown in Figure 3.8 (symbols). Typically for metals like Pt, the electrical resistance R_{Pt} increases approximately linearly near room temperature. However, the $R_{Pt} - T$ relation is much more complex at lower T. When T is less than the Debye temperature (240 K for Pt), R_{Pt} decreases as T^5 due to electron-phonon interaction. At even lower T, electron-electron scattering dominates, and R decreases as T^2. Also there exists a constant component due to scattering at impurities in the Pt. Therefore, R_{Pt} can be expressed as:

$$R_{Pt} = R_{imp} + aT^2 + bT^5 + cT \tag{3.1}$$

We used a 5th order polynomial fit for R_h and R_s as shown in Figure 3.8 (lines). When I_h was non-zero during the thermal experiments, the exact temperatures at the *heater* (T_h) and *sensor* (T_s) were obtained from the curves.
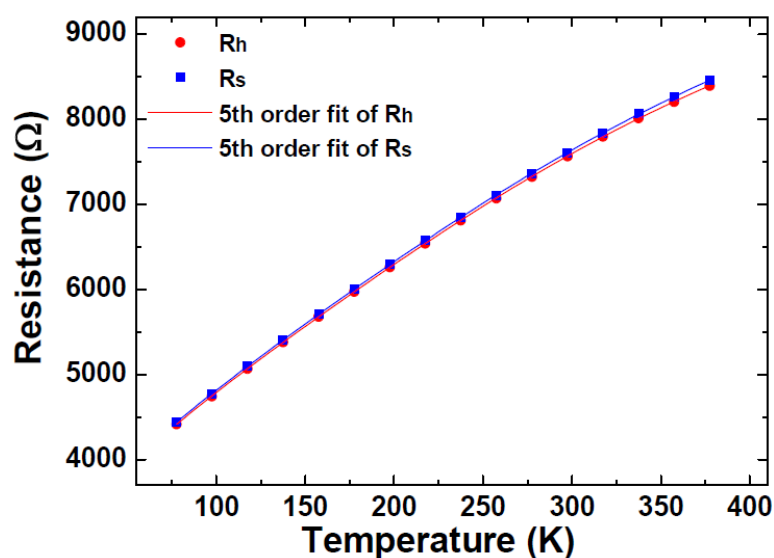
Figure 3.8: Data points (symbols) and 5th order fit (lines) of the *heater* and *sensor* resistances as a function of temperature.

The equivalent thermal circuit of the test device is shown in Figure 3.9. Since the METS was fully suspended and thermally isolated from the bulk substrate, the total power input to the system is:

$$Q = I_h^2 R_h + \frac{1}{2} I_h^2 R_L \tag{3.2}$$

where R_L is the total electrical resistance of the two connecting beams for passing the heating current I_h, and $\frac{1}{2} I_h^2 R_L$ accounts for the heating generated in these two beams of which only half flows towards the *heater* platform and the other half flows towards the bulk substrate. R_L was measured to be $\sim 22.8\%$ of R_h, and hence:

$$Q = 1.114 I_h^2 R_h \tag{3.3}$$

By Fourier's law:

$$Q_1 = (T_h - T_{sub})G_b = \Delta T_h G_b \tag{3.4}$$

$$Q_2 = (T_s - T_{sub})G_b = \Delta T_s G_b \tag{3.5}$$

where G_b is the total thermal conductance of the six SiN_x beams connecting the *heater* or *sensor* to the substrate. At steady state:

$$Q = Q_1 + Q_2 = (\Delta T_h + \Delta T_s)G_b \tag{3.6}$$

Combining Eqs. (3.3) and (3.6), we obtain:

$$G_b = \frac{1.114 I_h^2 R_h}{\Delta T_h + \Delta T_s} \tag{3.7}$$

When the *sensor* is at steady state, the heat coming from the *heater* side should be equal to Q_2, and hence:

$$Q_2 = G_s(T_h - T_s) = G_s(\Delta T_h - \Delta T_s) \tag{3.8}$$

where G_s is the thermal conductance of a suspended graphene sample. Combining Eqs. (3.5), (3.7) and (3.8), we obtain:

$$G_s = G_b \frac{\Delta T_s}{\Delta T_h - \Delta T_s} = \frac{1.114 I_h^2 R_h \Delta T_s}{\Delta T_h^2 - \Delta T_s^2} \qquad (3.9)$$

The contact resistance between graphene and platforms need to be excluded before computing the actual thermal conductance. Detailed discussion of the contact effects will be held later in Section 4.5.

For supported samples, G_s also includes the parallel thermal conduction in the SiN$_x$ platform bridging the *heater* and *sensor*. After the calculation of G_s, the graphene was removed using oxygen plasma, and the thermal conductance of the SiN$_x$ platform, G_{SiNx}, was measured in the same way. The actual thermal conductance of the supported graphene sample is simply the difference $G_s - G_{SiNx}$.

In our system, the lock-in amplifiers provide ± 0.05 Ω resolution on R_h and R_s, corresponding to ± 0.005 K temperature resolution in ΔT_h and ΔT_s. From Eq. (3.9), this translates into a sensitivity of ~10^{-10} W/K in the calculation of G_s, which is sufficiently good for graphene samples whose G_s values are normally in the order of 10^{-7} W/K.
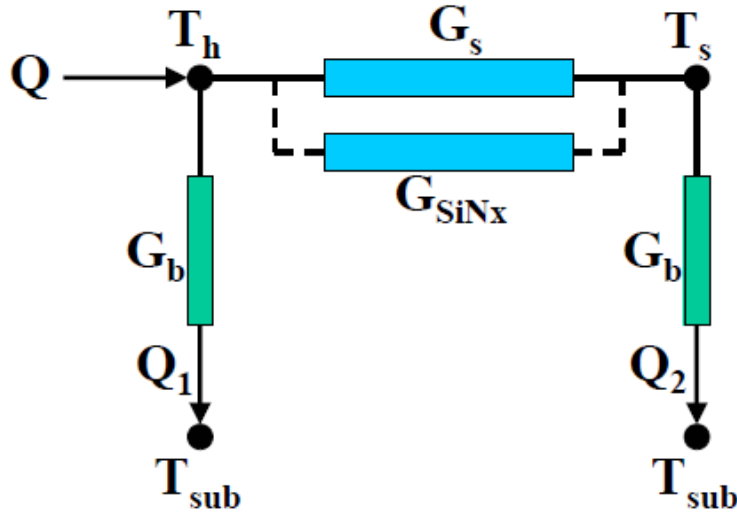
Figure 3.9: Equivalent thermal circuit of the device: G_s and G_b are the thermal conductance of the graphene and the six nitride beams respectively, and G_{SiNx} is the thermal conductance of the nitride platform between the *heater* and *sensor* for supported samples.

The four-point electrical resistance R of the graphene can be measured using the four Pt electrodes contacting the two ends of graphene with a third lock-in amplifier (just like measuring R_h and R_s). In addition, the Seebeck coefficient S can also be obtained with the same setup. A small temperature gradient was established by setting I_h to 10 µA and the potential difference ΔV between the central two electrodes was measured using a multimeter (Hewlett Packard 3458A) with 8.5 digit resolution (up to 10 nV). By definition we have:

$$S = \frac{-\Delta V}{T_h - T_s} \tag{3.10}$$

3.2.2 Spatially-resolved thermal resistance by an electron-beam heating method

Sometimes when the sample is not uniform, or when thermal boundaries exist due to material or structural changes, the conventional thermal-bridge technique described earlier becomes inadequate since it only provides information of the whole sample including the contacts, and cannot discriminate the contributions from different parts. In view of this, we have developed an electron-beam heating technique that can measure the local differential thermal resistance at any position of the sample.
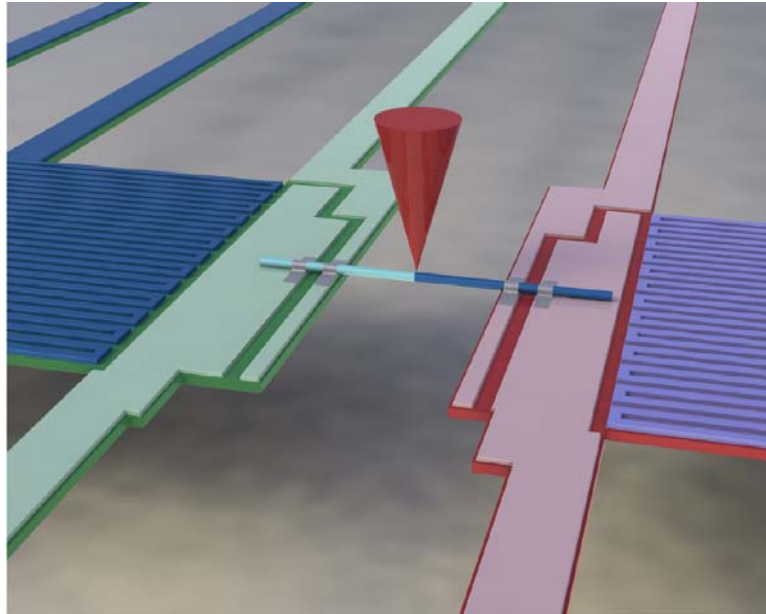
Figure 3.10: Schematic of the electron-beam heating method. The sample is assumed to be one-dimensional as far as heat flow is concerned.

Instead of using Joule heating from the *heater* to establish a temperature gradient for thermal conductance measurement, a focused electron beam in an SEM was used to induce localized heating along the sample, while both the *heater* and *sensor* acted as temperature sensors. The electron beam energy used in our experiments is $1-5$ keV, much lower than the 80 keV used in TEM imaging of graphene [102], hence lattice damage by the electron beam heating is negligible. The samples are assumed to be one-dimensional as shown in Figure 3.10. The heat generated at the electron beam spot flows in both directions, and the relative heat fluxes are determined by the cumulative thermal resistance from the spot to *heater* and to the *sensor*, respectively.
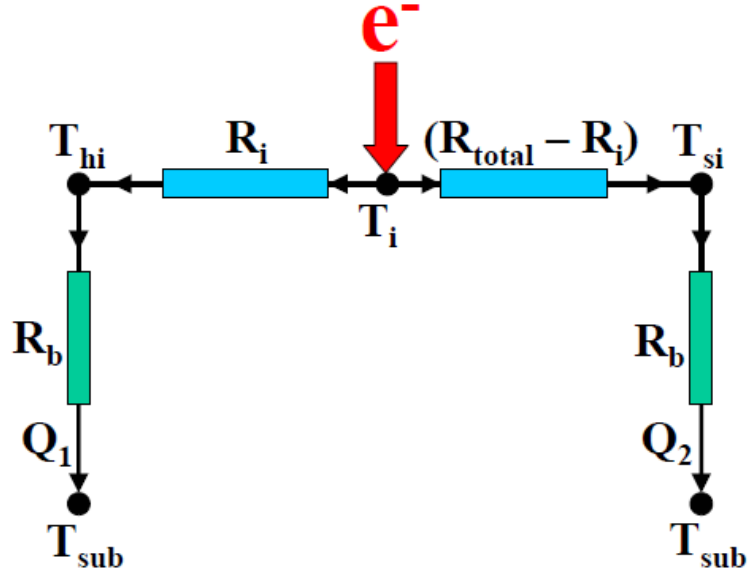
Figure 3.11: Equivalent thermal circuit of the device using the electron-beam heating method.

As illustrated by the thermal circuit in Figure 3.11, R_{total} is the total thermal resistance from the *heater* to the *sensor*, and R_i is the thermal resistance from the electron beam position i to the *heater*, R_b is the thermal resistance of the 6 SiN$_x$ beams, ΔT_i is the nominal temperature rise at position i, and ΔT_{hi} and ΔT_{si} are the temperature rises measured by the *heater* and the *sensor*, respectively. Since the *heater* and the substrate have a temperature difference of ΔT_{hi} with a known thermal resistance R_b in-between, the heat flux from the *heater* to the substrate is simply $\dfrac{\Delta T_{hi}}{R_b}$ by Fourier's law. At steady state, the net heat flow at the *heater* is zero, thus the heat flux from the electron beam position i to the *heater* is also $\dfrac{\Delta T_{hi}}{R_b}$, and hence:

$$\frac{(\Delta T_i - \Delta T_{hi})}{R_i} = \frac{\Delta T_{hi}}{R_b} \tag{3.11}$$

If we consider the heat flow at the *sensor*, a similar relationship is obtained:

$$\frac{(\Delta T_i - \Delta T_{si})}{R_{total} - R_i} = \frac{\Delta T_{si}}{R_b} \tag{3.12}$$

Making ΔT_i the subject in Eqs. (3.11) and (3.12), we have:

$$\Delta T_i = \frac{R_i \Delta T_{hi}}{R_b} + \Delta T_{hi} = \frac{(R_i + R_b)\Delta T_{hi}}{R_b} \tag{3.13}$$

$$\Delta T_i = \frac{(R_{total} - R_i)\Delta T_{si}}{R_b} + \Delta T_{si} = \frac{(R_{total} - R_i + R_b)\Delta T_{si}}{R_b} \tag{3.14}$$

Equating Eqs. (3.13) and (3.14):

$$\frac{(R_i + R_b)\Delta T_{hi}}{R_b} = \frac{(R_{total} - R_i + R_b)\Delta T_{si}}{R_b}$$

$$\frac{\Delta T_{hi}}{\Delta T_{si}} = \frac{R_{total} - R_i + R_b}{R_i + R_b} \tag{3.15}$$

For convenience, we define $\alpha_i = \dfrac{\Delta T_{hi}}{\Delta T_{si}}$. The electron beam is first focused on the

heater itself (denoted by position 0), $R_i = 0$ and by Eq. (3.15):

$$\alpha_0 = \frac{\Delta T_{h0}}{\Delta T_{s0}} = \frac{R_{total} - 0 + R_b}{0 + R_b} = \frac{R_{total}}{R_b} + 1 \tag{3.16}$$

Combining Eqs. (3.15) and (3.16):

$$\alpha_i = \frac{R_{total} - R_i + R_b}{R_i + R_b} = \frac{\dfrac{R_{total}}{R_b} - \dfrac{R_i}{R_b} + 1}{\dfrac{R_i}{R_b} + 1} = \frac{(\alpha_0 - 1) - \dfrac{R_i}{R_b} + 1}{\dfrac{R_i}{R_b} + 1}$$

$$\frac{R_i}{R_b} = \frac{\alpha_0 - \alpha_i}{1 + \alpha_i}$$

$$R_i = R_b \frac{\alpha_0 - \alpha_i}{1 + \alpha_i} \tag{3.17}$$

Note that α_0 is a constant determined at the start of the experiment by focusing the electron beam on the *heater*, and R_b is a known constant. By scanning the focused electron beam along the sample and recording the corresponding α_i, the cumulative

thermal resistance R_i can be obtained as a function of the distance between position i and the *heater*, i.e., the thermal resistance is spatially resolved.

From Eq. (3.9), we have:

$$R_{total} = R_b \left(\frac{\Delta T_h}{\Delta T_s} - 1 \right) \tag{3.18}$$

The uncertainty in the measurements of R_i using this technique is:

$$\delta R_i \leq \delta R_{total} = R_b \sqrt{ \left(\frac{\delta T_h}{\Delta T_h} \right)^2 + \left(\frac{\delta T_s}{\Delta T_s} \right)^2 } \tag{3.19}$$
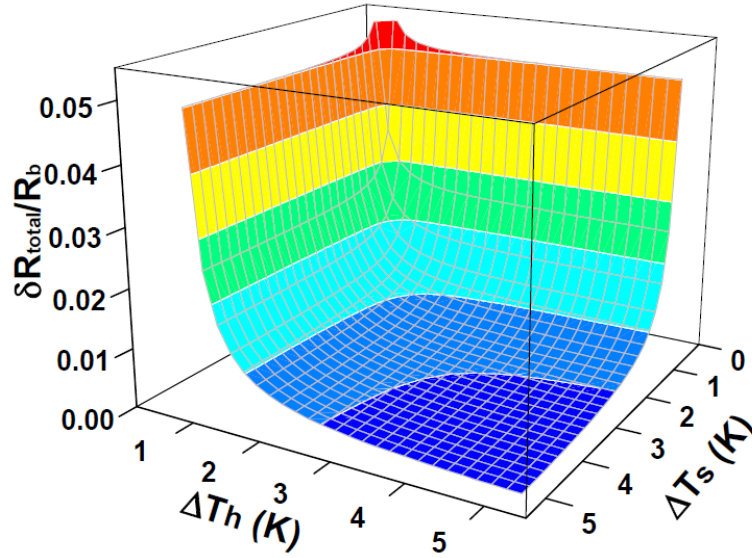
Figure 3.12: Normalized uncertainty in the thermal resistances measured by the electron-beam heating method as a function of temperature rises. The colors in sequence from red to deep blue indicate levels less than 0.05, 0.04, 0.03, 0.02, 0.01, 0.005, and 0.002.

Hence δR_i is limited by ΔT_h and ΔT_s, which depends on the heat generated from the electron beam. Here δT_h and δT_s are 0.005 K, and $\delta R_{total}/R_b$ is plotted as a function of the temperature rises in Figure 3.12. Typically the R_{total} concerned in the experiments is in the order of 10^6 K/W, or larger than 0.07 R_b (1.4×10^7 K/W at room temperature). For a reasonable level of $\delta R_{total}/R_{total} < 5$ %, ΔT_h and ΔT_s both need to be higher than 2 K.

Chapter 4   Thermal Transport in Graphene

Many theoretical studies on the thermal properties of graphene, such as the size dependence of its thermal conductivity [103] and effect of substrate scattering [104], have been reported recently but are yet to be experimentally verified. In addition, due to limitations of the existing approaches for thermal measurements, there still lacks a systematic study on the thermal transport in graphene. Based on the experimental techniques described in the previous chapter, the thermal conductivity and Seebeck coefficient of both suspended and supported graphene can be measured under different conditions. Various parameters affecting the thermal transport in graphene are investigated, and the experimental results are presented and analyzed in this chapter.

4.1   System calibration

Before proceeding with the thermal measurements, we noted that although the Pt resistance thermometers on the *heater* and *sensor* allowed fast and accurate temperature measurements with high sensitivity, the measured T_h and T_s represent the average temperatures of the Pt loops, and not the actual temperatures at the two ends of the graphene sample, as illustrated in Figure 4.1. In previous works [19, 39], the issue was disregarded by simply assuming that the *heater* and *sensor* platforms both had a uniform temperature distribution. However, we found that this idealized assumption could lead to large errors in the calculation of the sample thermal conductance G_s. Considering the direction of the heat flow, the actual T_h at one end of the sample is always slightly lower than the measured T_h from the Pt loop; and

similarly the actual T_s is higher than the measured T_s. Let us recall Eq. (3.8) for the calculation of G_s:

$$G_s = G_b \frac{\Delta T_s}{\Delta T_h - \Delta T_s} = \frac{1.114 I_h^2 R_h \Delta T_s}{\Delta T_h^2 - \Delta T_s^2} \qquad (3.8)$$

Since $\Delta T_h - \Delta T_s$ is involved in the denominator, even a marginal increase in this temperature difference could cause substantial decrease in the reciprocal value, i.e. G_s would be underestimated.
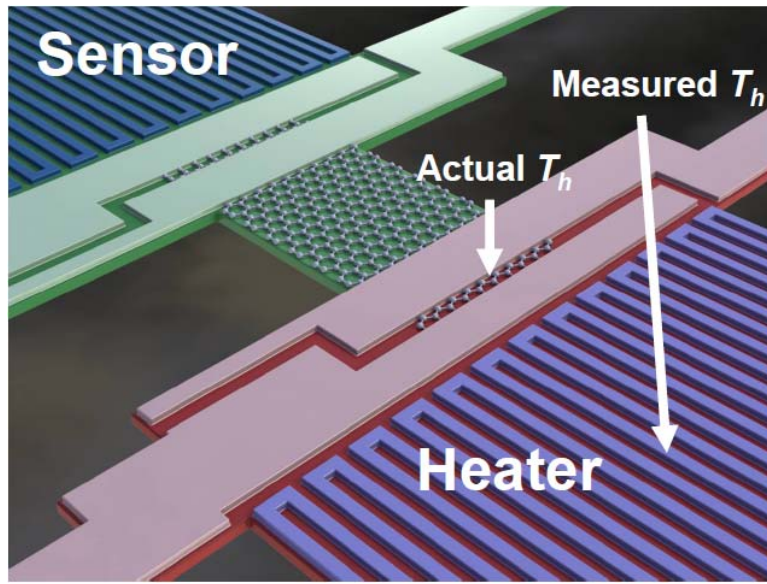
Figure 4.1: Schematic of the METS showing the difference between the actual T_h at the graphene edge and the measured T_h value by the Pt thermometer.

To eliminate this source of error, we carried out finite element method (FEM) modeling of the temperature profile using the ANSYS® Multiphysics software. The model was built with the same dimensions as the real test device, and the thermal conductivities for low stress SiN$_x$ and Pt thin films were specified using our measured values, which will be discussed shortly. Nevertheless, to reduce the complexity of the system and save computation time, the long SiN$_x$ beams connecting the *heater* and *sensor* to the substrate were shortened from 300 μm to 7.5 μm in the simulations. The

specified thermal conductivity for the beams was reduced by the same factor of 40 to keep their thermal conductance unchanged.

As shown in Figure 4.2 for the *sensor* platform, when the incoming heat flux causes a temperature rise of 10 K at the edge of the sample, the heat spreads towards the Pt resistance thermometer and finally towards the substrate through the six beams. The temperature profile along the dash-dotted line shows the non-uniformity on the *sensor* platform. The measured ΔT_s would be the average value in the Pt loop region, which is only 9.66 K. The actual ΔT_s is 10 K, ~ 3.5 % higher than the measured value. Since thermal conduction depends linearly on the temperature differences, the 3.5 % obtained is constant for any ΔT_s in actual experiments.
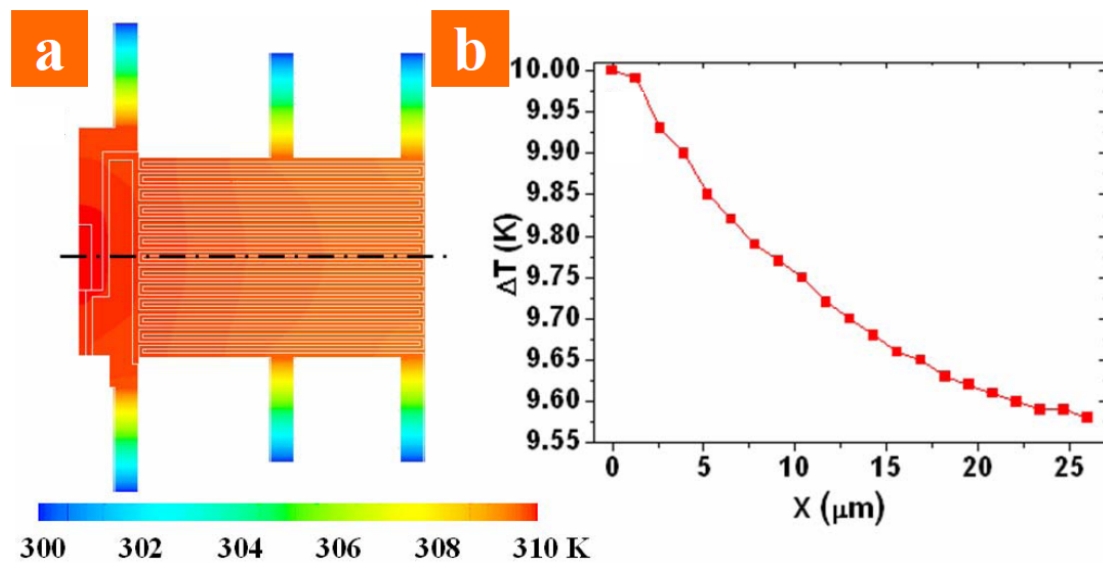
Figure 4.2: (a) Temperature distribution on the sensor platform when the actual ΔT_s is 10 K, simulated using FEM method. (b) Temperature profile along the dash-dotted line in (a).

The case is slightly more complicated for the *heater* platform, because the temperature distribution depends on the thermal conductance of the sample G_s as well. The extra rectangular region attached on the left-hand-side of the *heater* model shown in Figure 4.3(a) represents the simplified thermal path towards the sample and the *sensor* platform with the 6 connecting beams. The thermal resistance of the *sensor* is

constant at 1.5×10^7 K/W, and the value of G_s was typically between 1×10^{-7} W/K to 6×10^{-7} W/K for suspended and supported few-layer graphene samples. For instance, when $G_s = 1 \times 10^{-7}$ W/K, the temperature profile along the dash-dotted line plotted in Figure 4.3(b) shows that the actual ΔT_h at the edge of graphene is only 10.01 K, 3.0 % lower than the 10.32 K obtained by averaging in the Pt loop region.
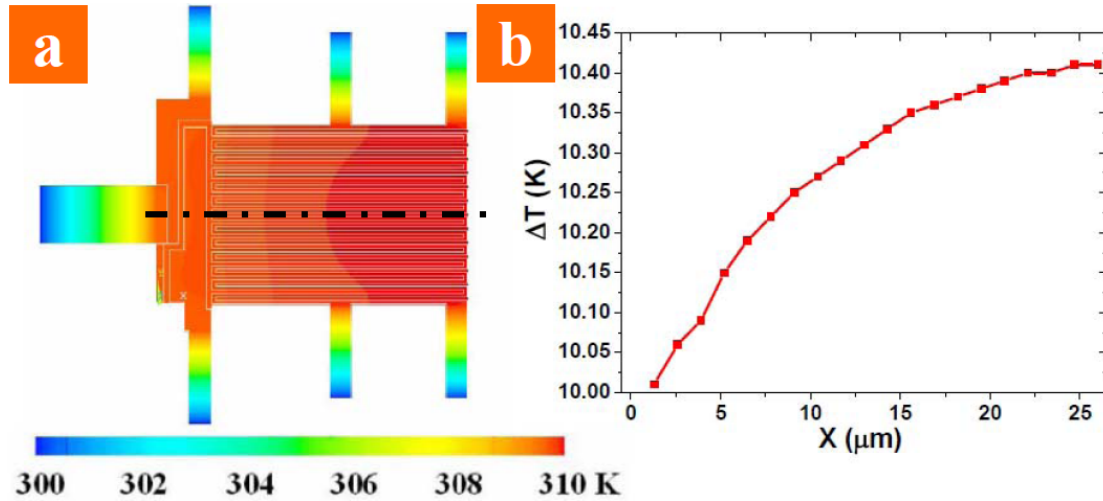
Figure 4.3: (a) FEM simulation of the temperature distribution on the *heater* platform when the actual ΔT_h is 10.01 K. (b) Temperature profile along the dash-dotted line in (a).
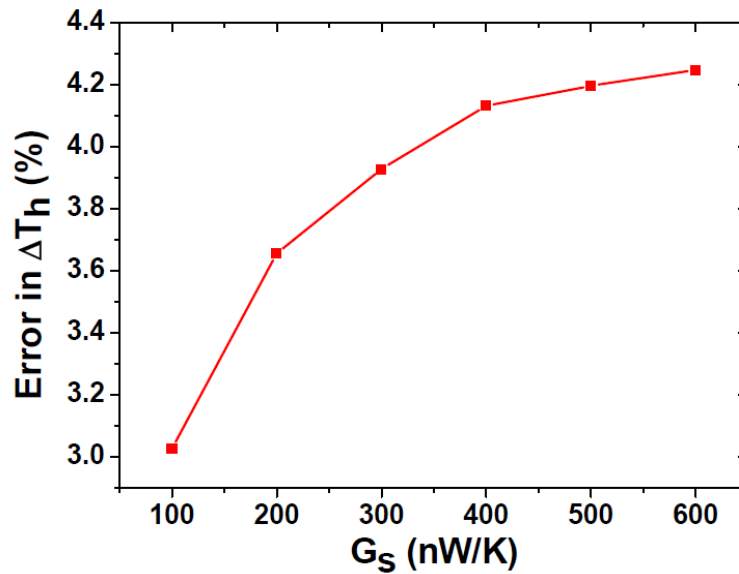
Figure 4.4: Simulated percentage error in ΔT_h as a function of G_s.

Simulations were also done for different values of G_s and the percentage error is plotted in Figure 4.4. For samples with higher G_s, the error increases as expected

due to a larger proportion of heat flowing in the sample direction. Hence the actual ΔT_h is ~ 3.0 – 4.3 % lower than that measured by the Pt thermometer. This substantial systematic error in ΔT_h and ΔT_s was compensated for in all subsequent calculations of G_s.

Thermal conductivity measurements were first performed on a calibration sample that was pre-fabricated together with the METS. It is a nanowire-like structure with a length of 5.0 μm and a width of 300 nm as shown in Figure 4.5. It was fabricated at the same time as the electrodes and the 12 connecting beams, comprising 60 nm thick Pt on top of 300 nm thick of SiN_x.
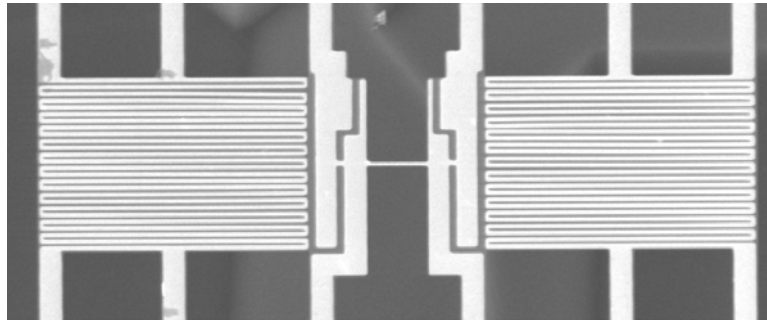
Figure 4.5: SEM image of the Pt/SiN$_x$ sample for calibration of the thermal measurements.
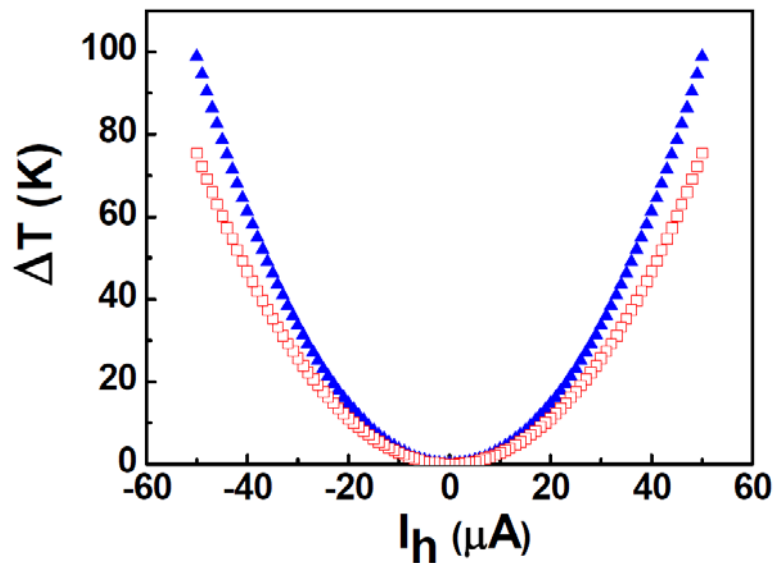
Figure 4.6: Plot of the temperature rise of the heater (blue triangle) and sensor (red square) as a function of the heating current I_h.

As shown in Figure 4.6, typically the temperature rise of the *heater* ΔT_h and the *sensor* ΔT_s shows a smooth quadratic increase when the heating current I_h ramps from 0 to 50 µA as expected from their linear relationship with the heating power $Q = 1.114I_h^2 R_h$. When the substrate was kept at room temperature (T_{sub} = 300 K), the $\Delta T_h - \Delta T_s$ plot in Figure 4.7 shows a perfect proportional relationship even when ΔT_h was as high as 100 K. Recalling Eq. (3.8):

$$G_s = G_b \frac{\Delta T_s}{\Delta T_h - \Delta T_s} \tag{3.8}$$

In this calibration sample $\Delta T_s \propto \Delta T_h$, i.e. $\dfrac{\Delta T_s}{\Delta T_h - \Delta T_s}$ is constant, and this implies that

$G_s \propto G_b$. Since this sample has the same material composition as the beams, it is not surprising that their thermal conductance have exactly the same temperature dependence. However, for other material systems such as graphene, the linear relationship between ΔT_h and ΔT_s will only hold for very small ΔT_h (< 10 K) where both G_s and G_b are almost unchanged.
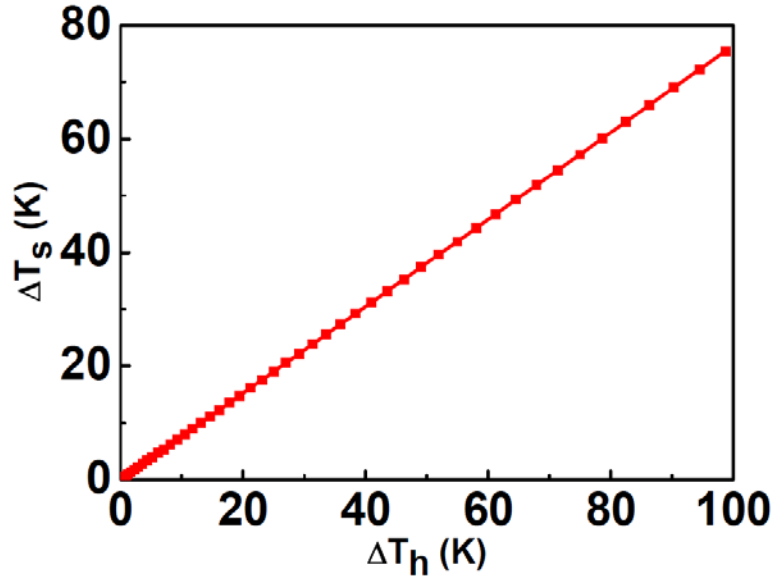
Figure 4.7: Plot of ΔT_s as a function of ΔT_h. Note the perfect straight line passing through all the data points showing $\Delta T_s \propto \Delta T_h$.

Figure 4.8 shows the calculated G_b and G_s as a function of I_h. At lower values

of I_h (< 3 μA), $\Delta T_h - \Delta T_s$ is too small (< 0.1 K), and results in overwhelming

measurement noise. As I_h sweeps from 3 μA to 10 μA, G_s stays almost constant since

there is little change in the sample temperature (< 4 K). The value of G_s was extracted

to be 85.0 nW/K at I_h = 10 μA, when the sample temperature was 303 K.
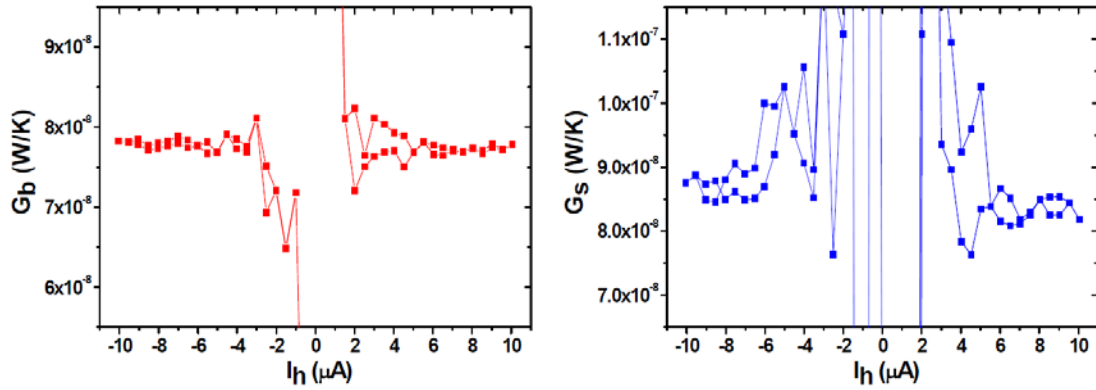
Figure 4.8: Plots of G_b (left) and G_s (right) as a function of I_h for the Pt/SiN$_x$ calibration sample.
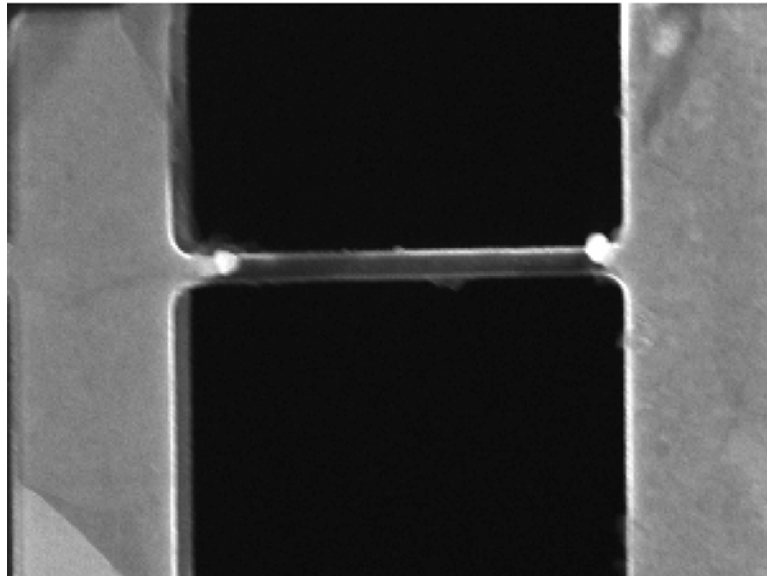
Figure 4.9: SEM image of the calibration sample after removing the top Pt layer using a Ga$^+$ focused ion beam.

The Pt layer was then removed using a Ga$^+$ focused ion beam (FIB), as shown

in Figure 4.9, and the value of G_{SiNx} for the remaining SiN$_x$ layer was measured to be

28.0 nW/K (Figure 4.10). Subtracting G_{SiNx} from G_s gives $G_{Pt} = 57.0$ nW/K. By definition of thermal conductivity:

$$\kappa = \frac{GL}{Wt} \tag{4.1}$$

We obtain $\kappa_{Pt} = 27.9$ Wm^{-1}K^{-1}. The four-point electrical resistance of the Pt layer was also measured, and the calculated electrical conductivity $\sigma_{Pt} = 0.41 \times 10^{-7}$ Ω^{-1}m^{-1}.
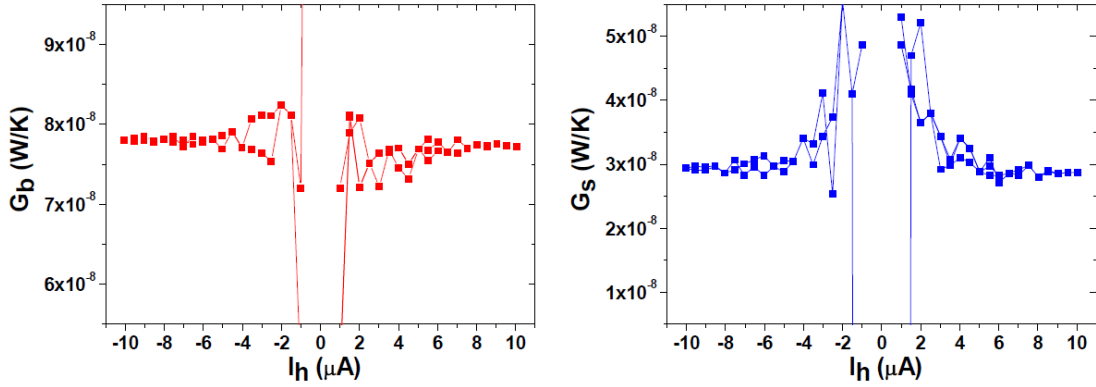
Figure 4.10: Plots of G_b (left) and G_s (right) as a function of I_h after removing the Pt layer.

For bulk Pt at 300 K, the reported values of κ'_{Pt} and σ'_{Pt} are 71.6 Wm^{-1}K^{-1} and 1.05×10^{-7} Ω^{-1}m^{-1}, respectively. It is unsurprising that large differences exist because σ and κ of a thin film depend very much on its thickness, crystalline quality and surface boundary scattering, and are generally lower than bulk values. Since in metals like Pt, thermal conduction is dominated by the electronic component, comparison of the measured and bulk values can instead be made using the Wiedemann-Franz law:

$$\frac{\kappa}{\sigma} = LT \tag{4.2}$$

where L is a constant known as the Lorenz number, and T is the sample temperature. We obtain $L = 2.25 \times 10^{-8}$ WΩm^{-2} for our sample and $L' = 2.27 \times 10^{-8}$ WΩm^{-2} for bulk Pt. The excellent agreement in L shows that the technique indeed provides reliable and accurate measurements of the thermal conductivity.

4.2   Thermal measurements of graphene

After testing with the Pt wire, a batch of suspended and supported graphene samples on the METS test structures were prepared as described in Section 3.1. For consistency, the widths (W) of all the samples were patterned to be 5.0 μm. Thermal measurements were first carried out on a supported 3-layer graphene flake S1 with a length (L) of 5.0 μm, as shown in Figure 4.11.
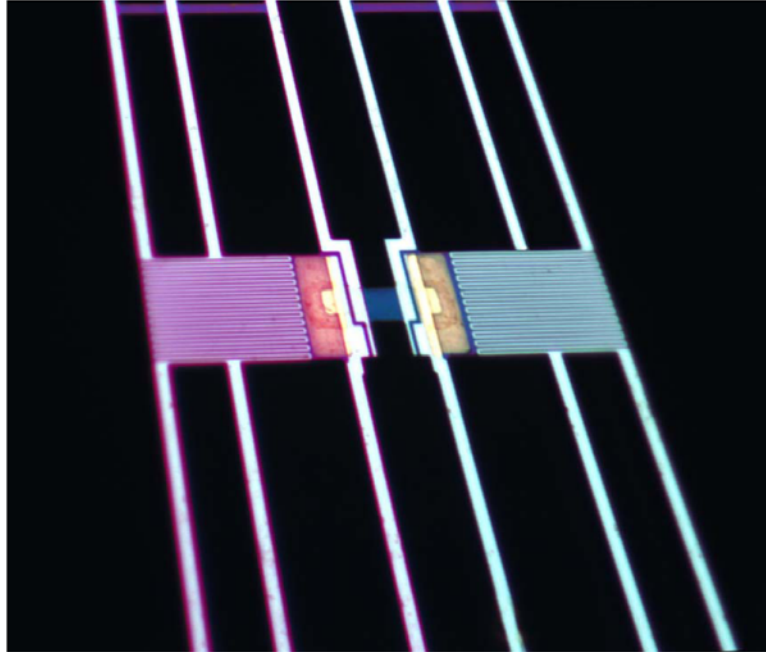
Figure 4.11: Optical image of sample S1 with false colors showing the temperature gradient established for thermal measurements (artificially colored − purple for 'hot' and blue for 'cold').

The Seebeck coefficient (S) of S1 was extracted using Eq. (3.9) and plotted against the sample temperature (T), as shown in Figure 4.12. The positive sign of S indicates that this graphene flake has an initial hole doping, which could have been introduced during the sample preparation process. The magnitude of S increases with T from 77 to 330 K, which agrees well with the linear scaling predicted by Mott formula of thermopower [105]:

$$S = -\frac{\pi^2}{3e}\frac{T}{\sigma(\mu)}\frac{\partial\sigma(\varepsilon)}{\partial\varepsilon}\bigg|_{\varepsilon=\mu} \tag{4.3}$$

where $\sigma(\varepsilon)$ is the energy-dependent electrical conductivity of graphene. The bending of the $S - T$ curve below 140 K is attributed to a small amount of doping from adsorption of residual gas molecules in the vacuum chamber, and this will be addressed in the next chapter. Also plotted in Figure 4.12 is the electrical conductivity (σ) calculated from its four-point resistance R, which increases with T due to thermal generation of charge carriers that enhances electrical conduction. Note that for two-dimensional systems like graphene, sheet conductivity is normally used instead of the 3D equivalent, and is defined as:

$$\sigma = \frac{L}{RW} \tag{4.4}$$
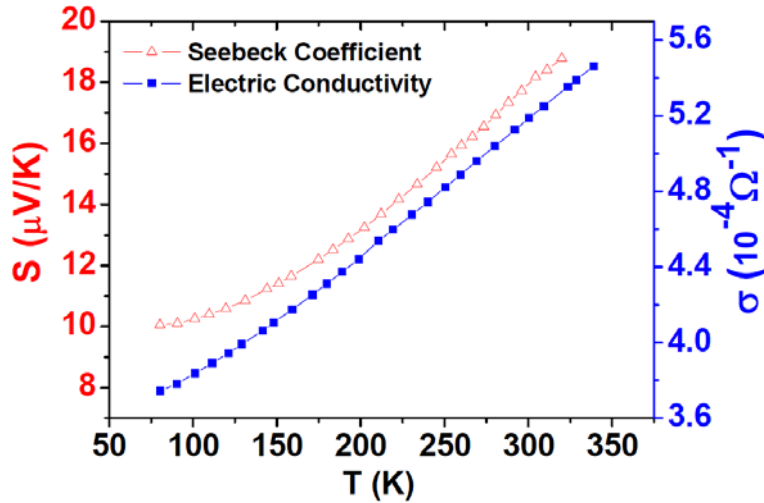
Figure 4.12: Plots of Seebeck coefficient S and electrical conductivity σ of S1 as a function of temperature T.

We have calculated the room temperature Seebeck coefficients for 3-layer graphene based on a density functional theory (DFT) model with the CASTEP package [106], using the method described by Ni *et al.* [107] and Markussen *et al.* [108]. Figure 4.13 shows the calculated S as a function of electron concentration n, where holes are represented by negative values of n. For a room temperature S of 18.0 µV/K obtained from Figure 4.12, the extracted hole concentration p is 4.7×10^{11} cm^{-2}.

Based on $\mu = \sigma / pe$, with e being the elementary charge, the calculated room temperature hole mobility μ has a high value of 7000 cm^{2}V^{-1}s^{-1}, which indicates that the graphene still maintains its good quality after going through the fabrication process.
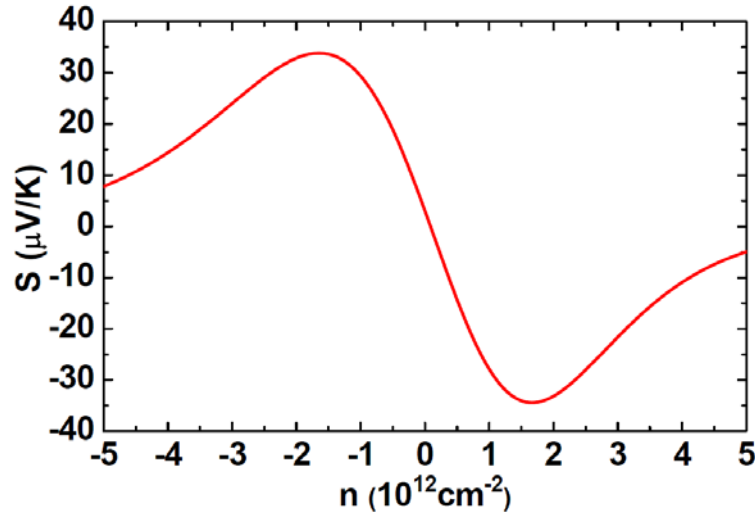
Figure 4.13: Simulated Seebeck coefficients at 300 K as a function of carrier concentration for 3-layer graphene.

Thermal conductance measurements of S1 were then carried out at different temperatures in a step-wise manner. As shown in Figure 4.14, T_{sub} was initially set to liquid nitrogen temperature of 77 K, and I_h was slowly swept from 0 to 20 µA causing a ΔT_h of 0 to 30 K (with $\Delta T_h - \Delta T_s < 3$ K). The thermal conductance of S1 was obtained the same way as with the calibration sample, and was continuously monitored as I_h increased. Since $\Delta T_h - \Delta T_s$ was kept small, κ of graphene may be assumed to be approximately linear between T_s and T_h, and hence the sample temperature can be safely assumed to be the average $T = \dfrac{T_h + T_s}{2}$, and the thermal conductance was plotted for $T \in$ (77 K, 106K). T_{sub} was then raised by 20 K and stabilized for 30 min in each subsequent step, and similar T-dependent thermal measurements were carried out.
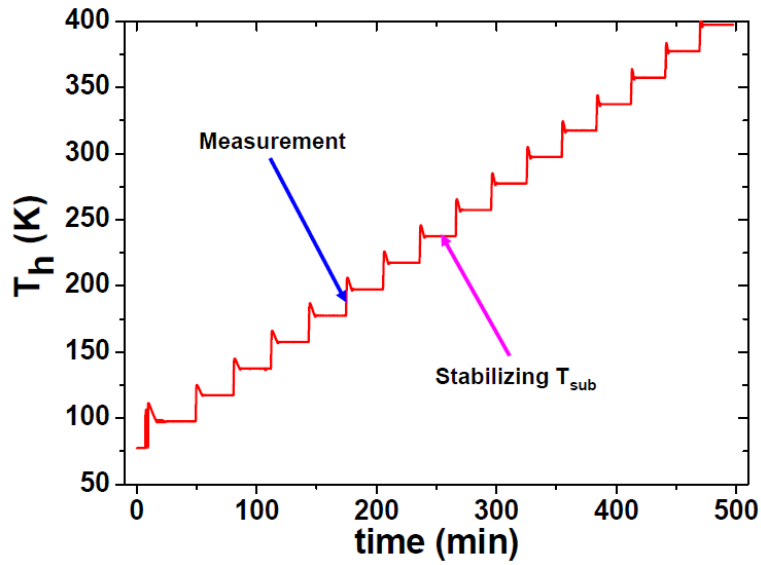
Figure 4.14: Plot of T_h as a function of time. T_{sub} was increased by 20 K after each measurement, so that ΔT_h can be kept small.

The measured thermal conductance segments from different steps joined smoothly, and G_{total} of S1 was plotted as a function of T in Figure 4.15 (blue curve). Since S1 is a supported sample, G_{SiNx} (red curve) of the SiN$_x$ support was also measured after removing the graphene using an oxygen plasma. By subtracting G_{SiNx} from G_{total}, the contribution of the graphene flake G_{S1} is obtained (green curve).
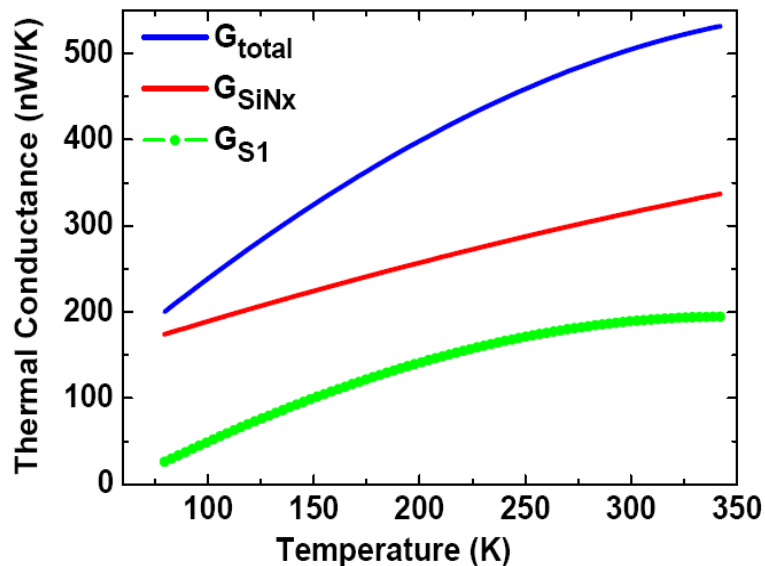
Figure 4.15: Measured thermal conductance of sample S1. G_{total} and G_{SiNx} are obtained before and after removing the graphene, and G_{S1} is the contribution from the graphene itself.

For graphene, the interlayer distance of graphite of 0.335 nm is used as the nominal thickness of each layer. For this 3-layer sample, κ is calculated using Eq. (4.1) and plotted in Figure 4.16. S1 has a room temperature κ of 1250 Wm^{-1}K^{-1}, which is comparable to that of pyrolytic graphite (PG) [36]. The similarity to the bulk value is reasonable since the lateral dimensions of S1 are relatively large (5.0 μm × 5.0 μm).
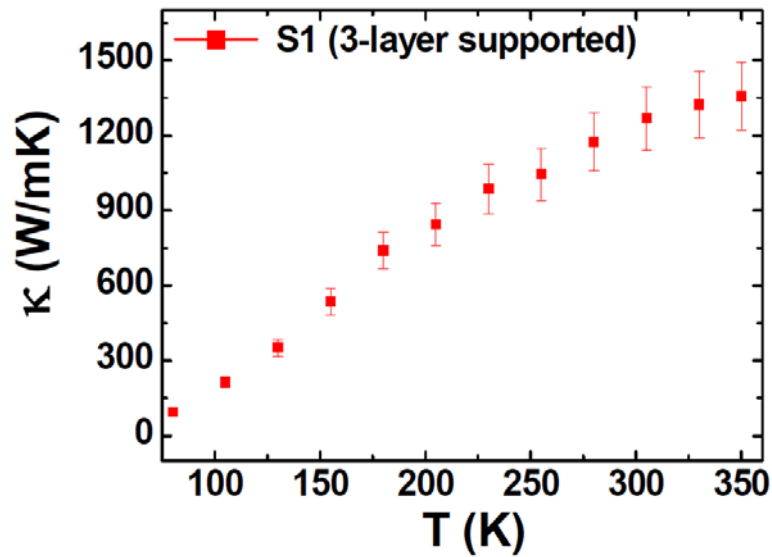
Figure 4.16: Thermal conductivity of S1 as a function of temperature.

4.3 Size dependence of κ and effect of substrate
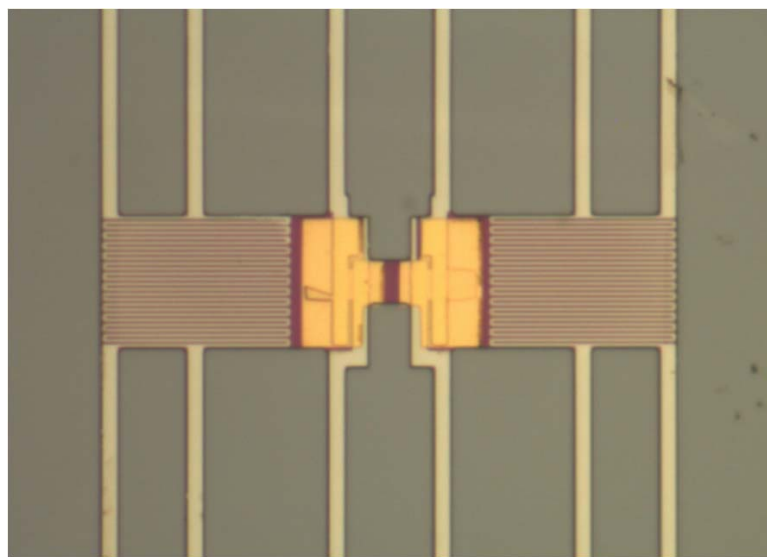
Figure 4.17: Optical image of S2, gap between the two gold pads is 2.0 μm.

To investigate the effect of lateral confinement on κ, the lengths of samples S2 and S3 were patterned to be 2.0 μm and 1.0 μm, respectively, while keeping all other parameters identical to those of S1. As shown in Figure 4.17, the METS used is the same as S1, but part of the graphene is covered by a thick gold layer that 'shorts' the thermal path. Thus the active length is actually defined by the distance between the gold pads.

The measured values of κ of S2 and S3 are shown in Figure 4.18. By a simple comparison, κ of S2 is remarkably lower than that of S1 with a room temperature value of 327 Wm^{-1}K^{-1}, and S3 has an even lower κ of only 150 Wm^{-1}K^{-1}.
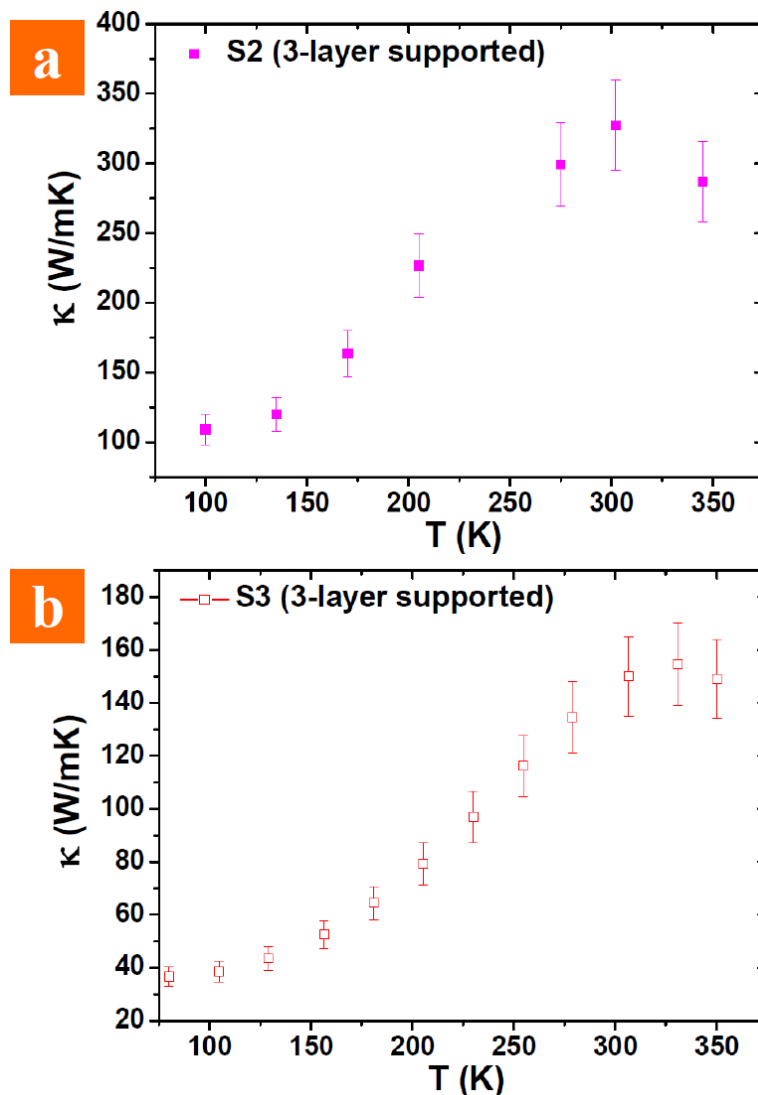
Figure 4.18: Thermal conductivity of (a) S2 and (b) S3 as a function of temperature.

Intrinsically, the thermal transport in graphene is limited by the three-phonon Umklapp scattering processes. For each branch of the phonon modes participating in the heat conduction, the thermal conductivity depends on the upper and lower cut-off values of the phonon frequencies, ω_{max} and ω_{min}. ω_{max} is defined from the actual phonon dispersion at the Brillouin Zone edges [75, 109], and ω_{min} for each branch is determined from the condition that the phonon mean free path (MFP) cannot exceed the actual physical length L of the graphene flake:

$$\omega_{min} \propto \sqrt{\frac{\omega_{max}}{L}} \qquad (4.5)$$

For bulk graphite, the low-bound cut-off frequency ω_c is defined by the on-set of cross-plane coupling of the phonon modes. Above ω_c, heat starts to propagate in all directions and heat transport along the basal plane reduces to a negligible value [103]. The ZO' phonon branch observed in the graphite spectrum provides a reasonable reference point for ω_c, which is close to 4 THz. When the flake size is larger than 4 – 10 μm (depending on T), ω_{min} falls below ω_c and the Umklapp-limited κ of graphene exceeds the theoretical value of graphite. For smaller flakes, due to boundary restrictions on the phonon MFP from the graphene edges, ω_{min} increases, which leads to a reduction in κ owing to a smaller interval of phonons (ω_{min}, ω_{max}) participating in the heat conduction. In other words, acoustic phonons with longer wavelengths are not available for heat transfer in smaller graphene flakes.

The inverse relationship of κ and L we have obtained is the first experimental evidence on the size dependence of the thermal conductivity of graphene, and is consistent with many theoretical works [79, 80, 103] which predict a drastic reduction in κ as the graphene size drops below 5 μm.

In addition, we also prepared a suspended 5-layer graphene sample S4 with L of 1.0 μm and W of 5.0 μm, and performed similar $\kappa - T$ measurements as shown in Figure 4.19. Since S4 has exactly the same lateral dimensions as S3, the discrepancy in their κ values is attributable either to the difference in their thickness, or to the effect of the substrate.
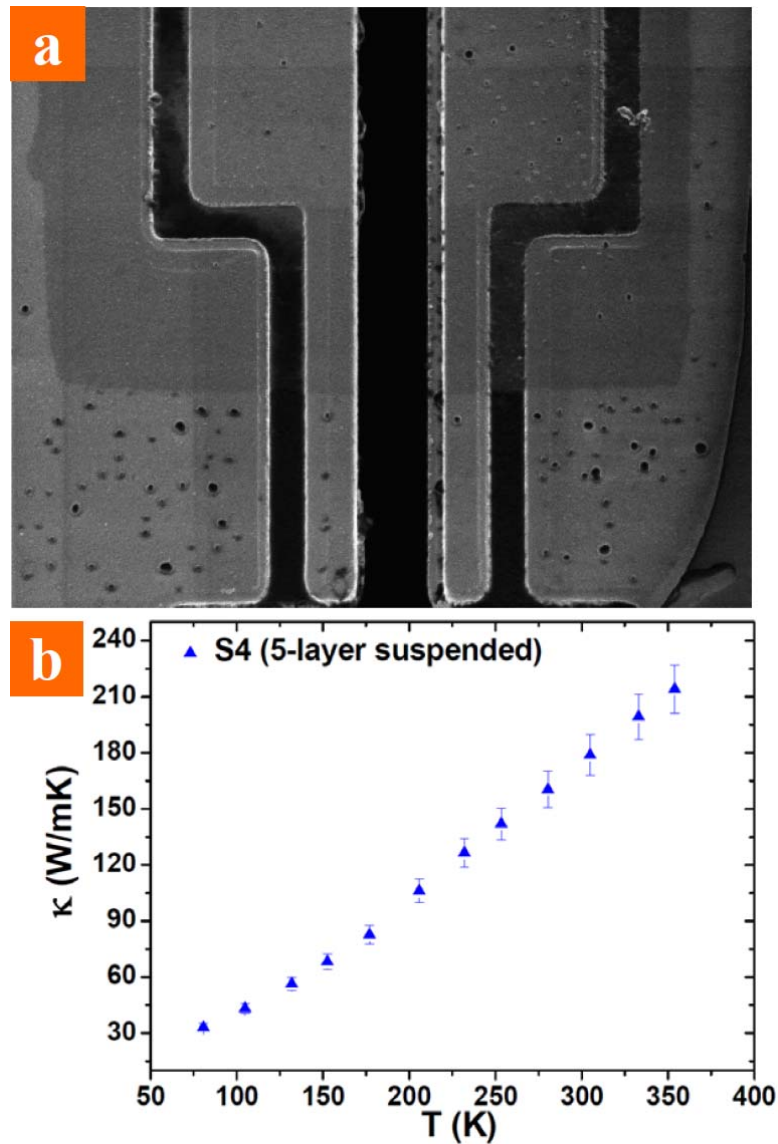
Figure 4.19: (a) SEM image of S4 taken after the measurements to avoid contamination. (b) Thermal conductivity of S4 as a function of temperature.

As freestanding graphene is very fragile, we could not prepare a 3-layer suspended sample. Nevertheless the inter-layer interactions in graphene have been

studied previously by Ghosh *et al.* [18], where κ is experimentally shown to inversely scale with the layer number. However, the κ of the 5-layer S4 is actually higher than that of the 3-layer S3 with a room temperature value of 170 Wm^{-1}K^{-1}, showing that thermal transport in graphene is indeed impeded by the presence of a substrate.
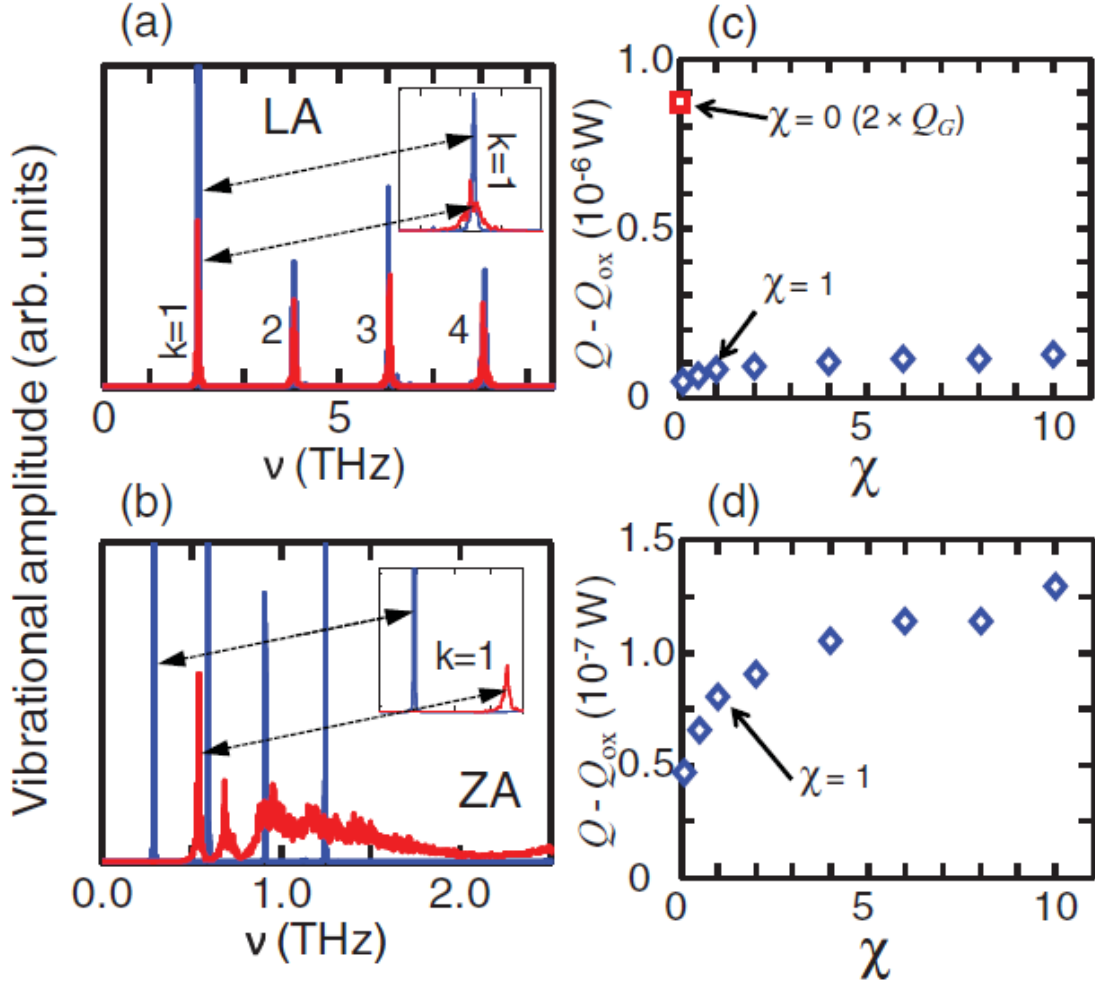
Figure 4.20: (a) and (b) Long-wavelength (k = 1 to 4) vibrational spectrum of free graphene (taller, narrower peaks) and supported graphene (shorter, broader peaks). (a) Distinct LA phonon peaks show little effect of the substrate. (b) ZA phonon peaks are significantly broadened and upshifted after the graphene is supported on the substrate. (c) Plot of heat flux through two suspended (2 Q_G) and supported ($Q - Q_{ox}$) graphene layers versus χ, which scales the vdW interaction at the graphene-SiO$_2$ surface; χ = 1 is the default interaction strength. The heat flux through supported graphene is approximately one order of magnitude lower than that through the suspended SLG. (d) Zoom-in version of previous plot. The heat flux along supported SLG ($Q - Q_{ox}$) increases by a factor of three as the graphene-SiO$_2$ interaction χ increases from 0.1 to 10. This counterintuitive result can be explained by the coupling of graphene ZA modes with SiO$_2$ surface waves, which increase the group velocity of the hybridized modes. [104]

The reduction in κ was also observed for a supported SLG [19] and is attributed to the suppression of the dominant out-of-plane (ZA) phonon modes by the

substrate [15], which contributes up to 77 % of κ (Figure 2.17). On the other hand, it has also been argued that ZA modes do not contribute significantly to κ due to their small group velocity [76, 103]. The former claim was bolstered by a very recent work [104] which computed the substrate effect using molecular dynamics (MD) simulations. It is shown that in suspended graphene, the long-wavelength ZA modes have the longest lifetimes and dominate thermal transport; whereas in supported graphene, significant broadening and frequency shift of the ZA peaks indicate strong coupling to the substrate (Figure 4.20), which lowers κ by up to 90.7 % depending on the strength of the van der Waals interactions.

However, the difference is only ~13% (170 $Wm^{-1}K^{-1}$ vs. 150 $Wm^{-1}K^{-1}$) in our case possibly because the upper layers of the FLG have less interaction with the substrate. The measured room temperature κ of the 3-layer S1 (1250 $Wm^{-1}K^{-1}$) is also higher than that reported for supported SLG (600 $Wm^{-1}K^{-1}$) [19], showing the diminishing effect of the substrate on the thermal transport in the top layers, and it is consistent with a recent report on thermal conductivity measurements of encased graphene [110].

4.4   Temperature dependence of κ

The $\kappa - T$ graphs of S2 – S4 are plotted together in Figure 4.21 for comparison. The κ of supported graphene shows an increase with temperature and reaches a maximum at around 310 – 360 K. This $\kappa - T$ relation agrees well with that obtained for a supported SLG [19], and the phonon transport is believed to be dominated by substrate interaction and Umklapp scattering before and after the peak, respectively. However, for suspended graphene, κ keeps increasing and shows no sign of saturation

even at 350 K. The turnover temperature is much higher than the 140 K measured for

bulk pyrolytic graphite [36] due to the restrictions on the phonon mean free path from

the graphene edges. Boundary scattering is believed to dominate Umklapp scattering

over the temperature range of measurements (77 to 350 K), and the peak of κ shifts

towards higher temperatures for smaller flakes as shown in Figure 4.22. This

temperature dependence of κ is also consistent with those obtained in the theoretical

studies for small-sized graphene flakes with dominant boundary effects [103, 111].
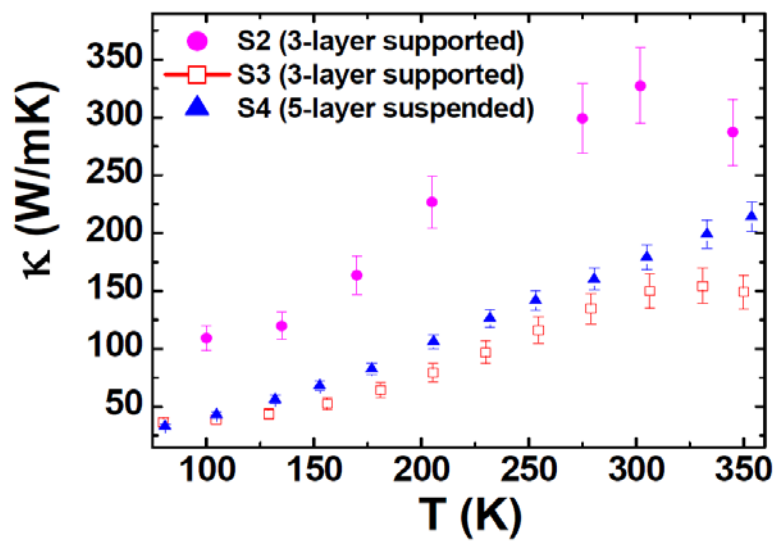
Figure 4.21: Thermal conductivity of S2 – S4 as a function of temperature. Sample dimensions ($L \times W$): S2 (2.0 μm × 5.0 μm), S3 (1.0 μm × 5.0 μm) and S4 (1.0 μm × 5.0 μm).
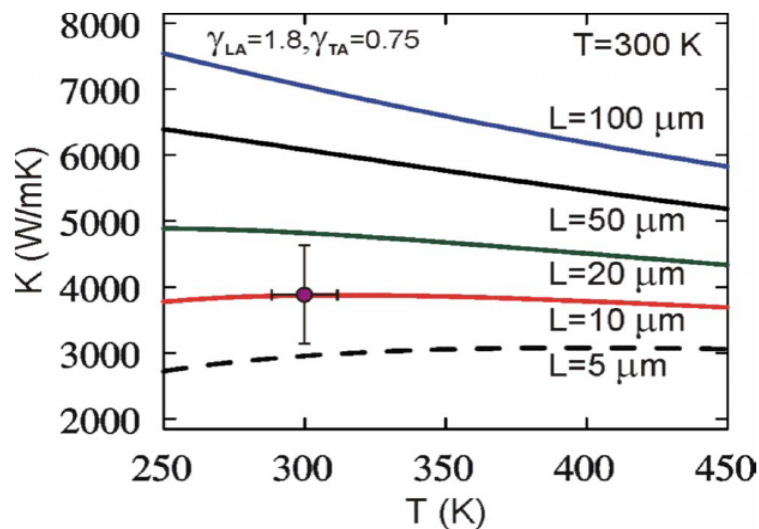
Figure 4.22: Thermal conductivity of graphene flake as a function of temperature for several linear dimensions L of the flake. [103]

The $\kappa - T$ relation of S4 is replotted on a logarithmic scale in Figure 4.23, which shows $\kappa \sim T^{\alpha}$ with $\alpha = 1.4 \pm 0.1$. This suggests that the flexural ZA phonon modes with a quadratic dispersion (giving $\alpha = 1.5$) may contribute more significantly than the linearly dispersed in-plane LA and TA modes (giving $\alpha = 2$) [63]. This temperature dependence could also be caused by other factors. However due to the limitation of our testing equipment, we could not go to very low temperatures to explore the exact mechanism.
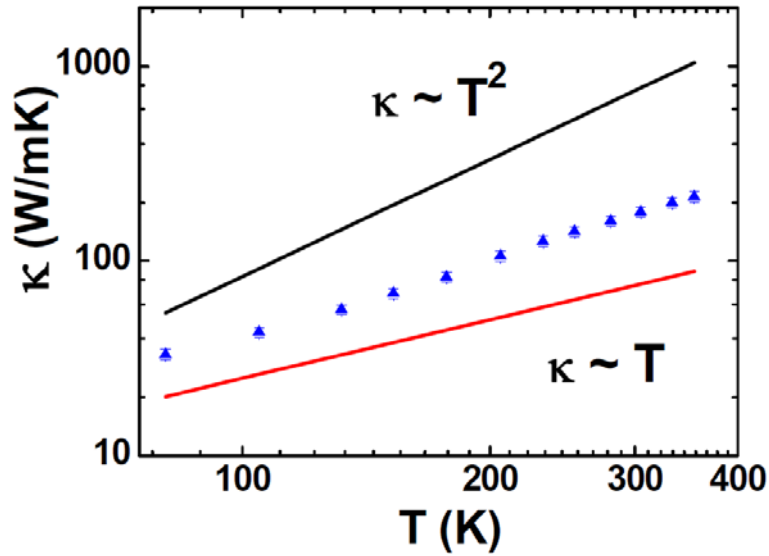
Figure 4.23: κ of S4 replotted on a logarithmic scale.

4.5 Thermal boundary resistance

The measured values of κ are generally lower than those from theoretical studies, and we attribute the deviation partly to the presence of the graphene-contact interface, which may constitute a significant scattering site. Here we investigated the thermal boundary resistances (TBR) at the contacts R_{c1} and R_{c2} in series with the graphene as shown in the equivalent thermal circuit (Figure 4.24).
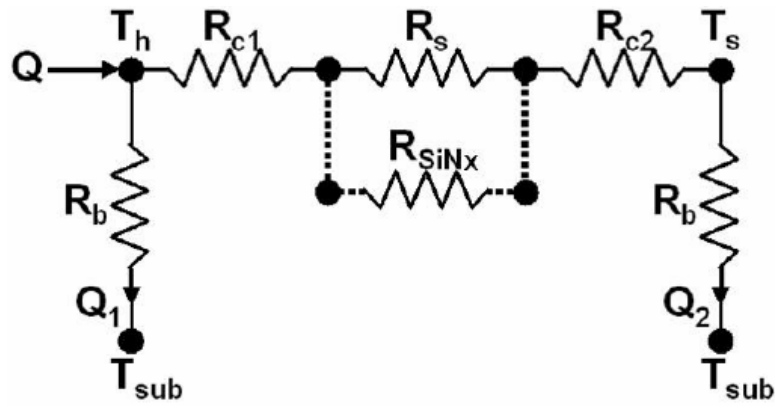
Figure 4.24: Equivalent thermal circuit of the device, R_{c1} and R_{c2} are TBR at the contacts, and R_{SiNx} is the thermal resistance of the nitride platform for supported samples.
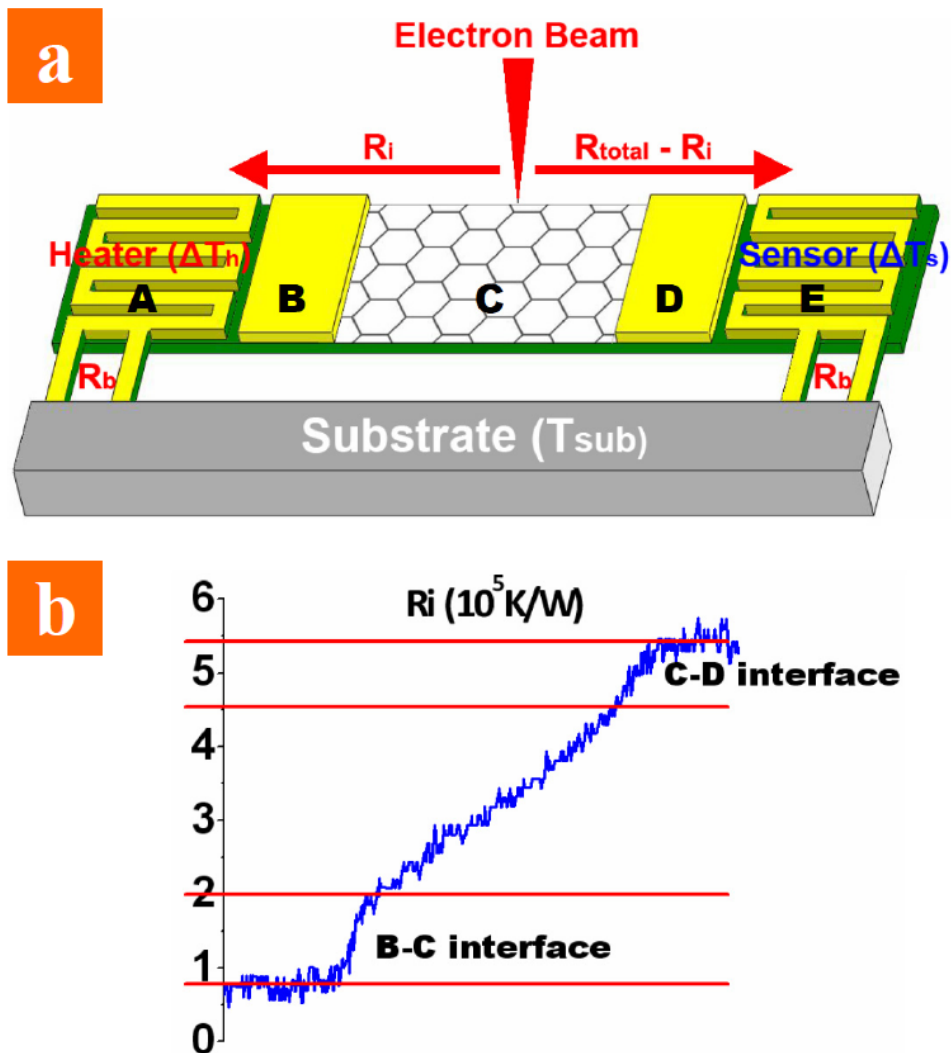
Figure 4.25: (a) Schematic of the localized electron beam heating technique. The connecting beams were only drawn on one side. R_b, R_{total} and R_i denote the thermal resistances of: the connecting beams, from heater to sensor, and from heater to electron beam spot respectively. (b) Spatially-resolved thermal resistance R_i of sample S3.

As illustrated in Figure 4.25(a), as heat flux propagates from the *heater* (A) to graphene (C) and from graphene to the *sensor* (E), phonon transport is impeded at the contacts (B & D) due to sudden material and structural changes. There are actually two distinct types of thermal boundaries to be studied.

The first is the cross-plane TBR between the Pt, graphene and SiN_x layers in regions B and D, which is normally referred to as the 'thermal contact resistance'. A half-space structure model is assumed for each of the Pt/graphene and graphene/SiN_x interfaces. Two widely used predictive models for calculating TBR are the acoustic mismatch model (AMM) and the diffusive mismatch model (DMM), which typically represent upper and lower limits for TBR, respectively.

In AMM, phonons propagate elastically across the interface, and the scattering is represented by the reflection coefficient R:

$$R = \frac{(Z_2 - Z_1)^2}{(Z_2 + Z_1)^2} \qquad\qquad (4.6)$$

where Z_1 and Z_2 are the acoustic impedances of the two materials calculated from:

$$Z = \rho V = \rho \sqrt{\frac{E}{\rho}} = \sqrt{\rho E} \qquad\qquad (4.7)$$

where ρ is the density, V is the acoustic velocity and E is the Young's modulus of the material.

For graphene, the reported E has a large value of 1.0 TPa [112] and ρ is assumed to be the same as high quality graphite (2.23 g/cm^3). For Pt and SiN_x, bulk values of ρ (21.45 g/cm^3 and 3.44 g/cm^3) and E (168 GPa and 380 GPa) are used. The calculated reflection coefficient is 1.4 % for the Pt/graphene interface and 1.8 % for the graphene/SiN_x interface. Since AMM places an upper bound on TBR, more than 98 % of the energy can be transmitted freely between the planes. In addition, the

contact area of the 3 layers (6 μm × 5 μm) is much larger than the cross-section of the graphene itself (~ 1 nm × 5 μm), and the cross-plane TBR is therefore negligible. This is also consistent with the low thermal contact resistance measured experimentally between graphene and SiO_2 [95] or between graphite basal plane and Pt [97].

The other type of TBR is also called Kapitza resistance, which differs from contact resistance and exists even at atomically perfect interfaces. In our system, the TBR is encountered as phonons transport from region B to C (or C to D). This is normally overlooked in the thermal analysis of bulk materials, but becomes critical for low-dimensional samples such as carbon nanotubes [113]. When heat is conducted by the graphene lattice vibration, thermal waves are scattered at the B-C junction due to the different boundary conditions arising from the additional Pt layer in region B. At intermediate or high temperatures, transmission at the interface is determined mainly by the mismatch in the density of phonon modes, since the phonon wavelength is short and the scattering is purely diffusive [114]. Due to the complex phonon dispersion of the sandwiched graphene in region B, it is difficult to obtain an analytical solution for the in-plane TBR. Hence, we employed the non-contact electron beam heating method described in Section 3.2.2 to quantitatively analyze the TBR incurred at the B-C (or C-D) junction.

For the 1 μm-long sample S3, the spatially-resolved thermal resistance R_i from position i on the sample to the *heater* (A) is plotted in Figure 4.25(b) as the electron beam scans across regions B, C, and D. The value of R_i remains constant in regions B and D showing good temperature uniformity at the metal-covered area, and increases linearly in region C as expected. However, an abrupt step increase in the R_i value is observed at both B-C and C-D interfaces, which accounts for almost half of the total measured thermal resistance. The TBR incurred is almost the same regardless of the

sample length, and was found to be 35 % and 20 % of the total measured thermal resistance for the 2 μm-long S2 and 5 μm-long S1, respectively. Thus, the apparent measured thermal conductance of graphene is significantly reduced by the in-plane TBR at the contacts, especially for smaller flakes.

Although this in-plane TBR is not part of the intrinsic characteristic of the thermal transport in graphene, it closely mimics the real-life scenario as there are always material or structural changes at the graphene edges when it is used as a thermal element in electronic devices.

The phenomenon could be more obvious in suspended graphene as the ZA flexural phonons are employed for the thermal transport in addition to the LA and TA phonons in supported samples. Unfortunately, the suspended S4 was too transparent to the electron beam for sufficient heat to be generated for the technique to work, and we are unable to verify this.

To investigate the operation limit of the technique on suspended graphene, we have carried out Monte Carlo simulations using the CASINO$^{®}$ software to calculate the absorbed electron energy. Note that this is a simplified approach that only gives a very rough estimate on the electron energy loss, whereas the interaction between electrons and real graphene is much more complex. The trajectories of 1 million electrons were simulated when passing through a layer of carbon with a specified density of 2.23 g/cm^2, and the distributions of the energies of backscattered electrons (BE) and transmitted electrons (TE) were calculated. Figure 4.26 shows the energy distributions of TE and BE for a primary electron beam energy (E_{beam}) of 1 keV and a carbon layer thickness of 1 nm (equivalent to 3-layer graphene), and the backscattering coefficient $\eta = 0.008416$. It is observed that the TE still possesses very high (~ 0.975 keV) energy after penetrating the 3-layer graphene, and very little

energy is transferred from the former to the latter. The average energy absorbed for each primary electron ($E_{absorbed}$) is:

$$E_{absorbed} = E_{beam} - (1 - \eta)E_{TE} - \eta E_{BE} \qquad (4.8)$$

where E_{TE} and E_{BE} are the average energies of each TE and BE respectively, obtained by integrating the energy distribution graphs weighted by the normalized hits. Thus for the first model, $E_{absorbed}$ was found to be 27.02 eV.
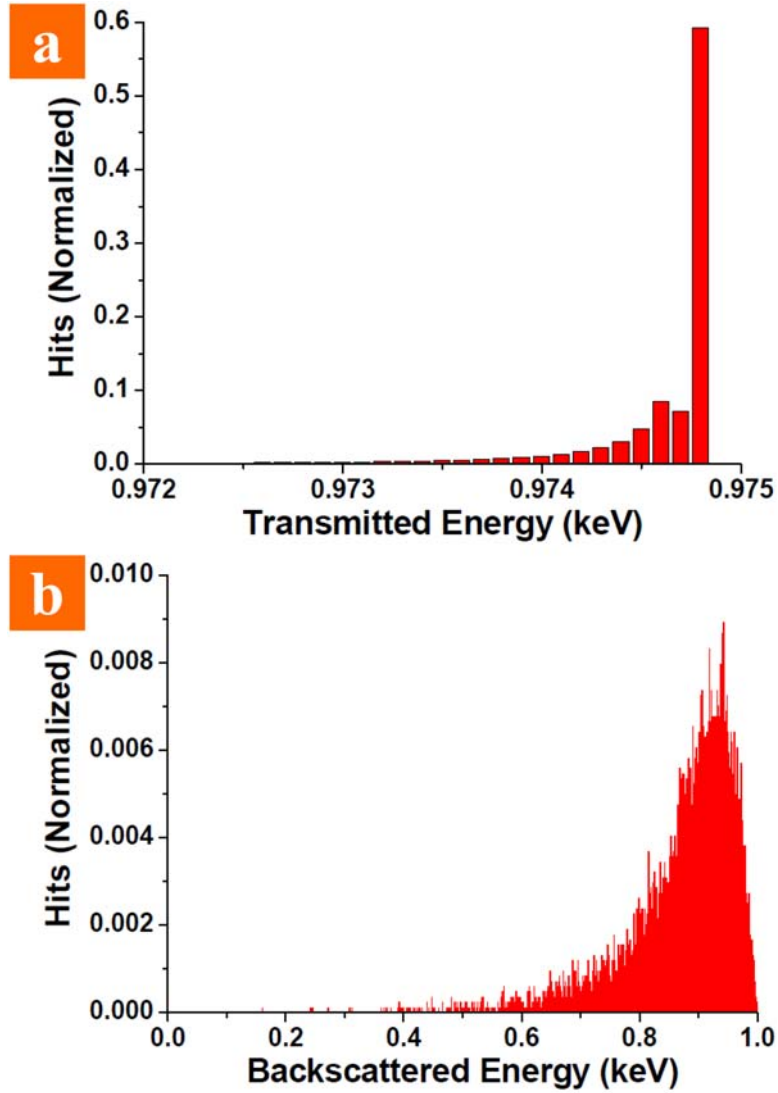
Figure 4.26: Energy distribution of (a) transmitted electrons and (b) backscattered electrons for a primary beam energy of 1 keV and a graphene thickness of 1 nm.

To spatially resolve the thermal resistance, typically the e-beam technique requires a minimum ΔT_h and ΔT_s of 0.2 K for a tolerable level of noise. By Eq. (3.5),

using 7×10^{-8} W/K measured for G_b, the minimum heating power Q_{min} is 28 nW. The e-beam power absorbed by graphene is:

$$Q_{absorbed} = \frac{I_{beam}}{e} E_{absorbed} \qquad (4.9)$$

Even for a large beam current of 0.5 nA, the required $E_{absorbed}$ needs to exceed 56 eV, much higher than that absorbed by the 3-layer graphene. The energy absorption was also simulated for different beam energies from 2 to 5 keV as shown in Figure 4.27, where $E_{absorbed}$ actually decreases for larger E_{beam} as a result of reduced interaction with higher energy primary electrons. Hence the only way to increase $E_{absorbed}$ is by increasing the graphene thickness.
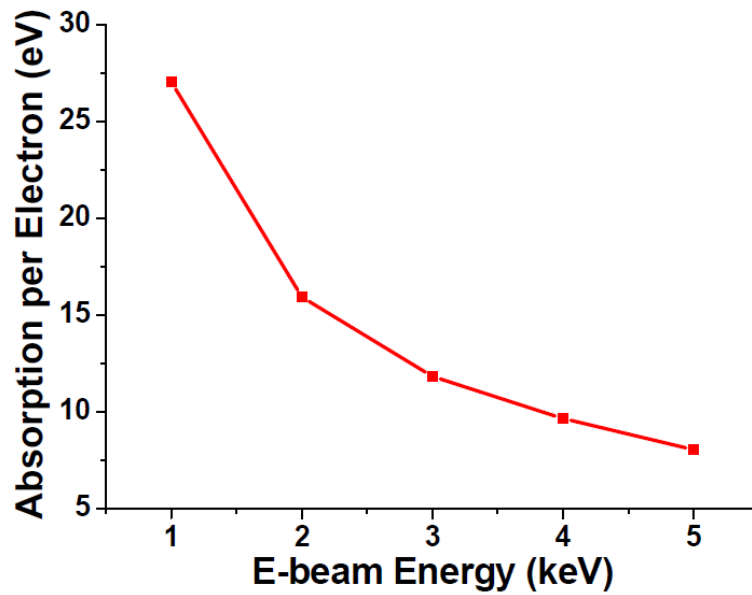
Figure 4.27: Average energy absorbed per primary electron as a function of primary beam energy.

Simulation results show that $E_{absorbed}$ scales almost linearly with the number of layers of graphene (Figure 4.28) for an E_{beam} of 1 keV. This is expected since most electrons can penetrate the entire sample and the energy transfer at each individual graphene layer is almost the same. Thus the technique should work for graphene samples thicker than 6 layers ($E_{absorbed}$ = 57.10 eV). Note that here we have only

considered the ideal case and calculated a lower bound. In real experiments, the sample needs to be slightly thicker subject to different noise levels and beam currents.
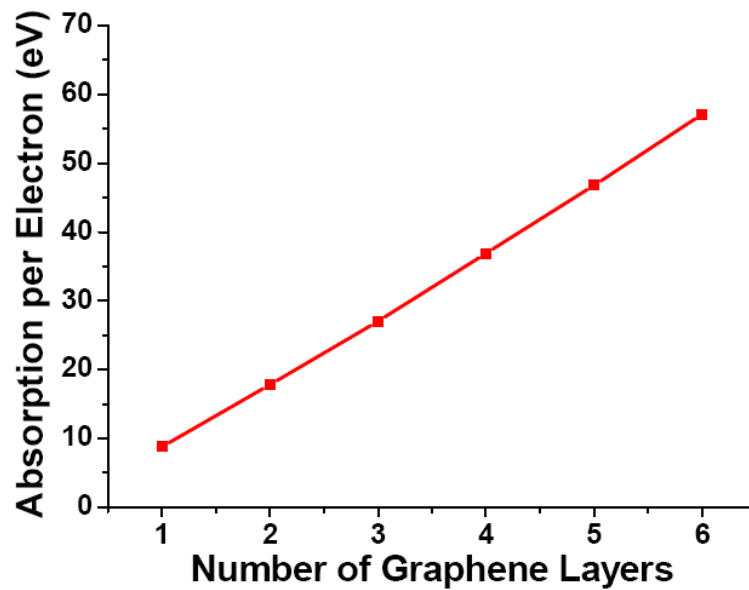
Figure 4.28: Average energy absorbed per primary electron as a function of number of graphene layers.

4.6   Summary

In summary, the focus of the work in this chapter is to investigate various parameters affecting the thermal transport in graphene. We have provided the first experimental evidence on the size dependence of thermal conductivity, and also looked into practical issues such as substrate scattering and thermal boundary resistances at the edges of graphene.

Chapter 5   Gas Adsorption Studies on Graphene

From the previous chapter, it is found that thermal transport in graphene is significantly impeded by the presence of an underlying substrate. In practical devices, the surface of graphene is also exposed to various gas ambients during the fabrication processes. If graphene is not properly desorbed before the final encapsulation, gas molecules/atoms can get trapped on the graphene, and may act as phonon scattering sites and affect the thermal transport. In addition, charge transfer can also take place between adsorbates and graphene via chemical bonds or van der Waals interactions, resulting in an electrical doping effect. This chapter describes measurements carried out in different gas environments, and we will focus on the effects of gas adsorption on the thermal and electrical properties of graphene.

5.1   Effects of gas adsorption on the thermal and electrical properties of graphene

To exclude the complication from the substrate effect, experiments were carried out on the suspended sample S4. The surface of S4 was first cleaned by a thermal annealing process to remove the adsorbates (hereafter referred to as 'contaminants' to differentiate from the intended adsorbates we are studying) originating from the imperfect vacuum (the best achievable pressure in our system is 3×10^{-7} mBar). A current of 50 μA was passed through both the *heater* and the *sensor* Pt loops for the heating. The bulk substrate remained at the initial temperature, and only a small region around the graphene sample (including the *heater* and *sensor* platforms) was heated to the desired temperature of 600 K. Due to the small thermal capacity of that region, the graphene sample could be heated up and cooled back

down in less than 10 seconds. The cooling rate is critical, because once the graphene surface has cooled down, it would once again be slowly covered by contaminants. The adsorption rate of gases on the graphene surface will be discussed in detail shortly.

The sample S4 was annealed at 600 K in vacuum for 2 hours and its surface condition was inferred from the electrical resistance R that was monitored *in situ*. Generally, the adsorbates would contribute a small n- or p-type doping to the graphene, and a pristine surface would result in the highest R. Upon annealing, R kept increasing with time due to the gradual desorption of the adsorbates, and saturated after 90 min, showing that the surface was almost free of contaminants. After annealing for another 30 min, the sample was quickly cooled down and was ready for adsorption studies.
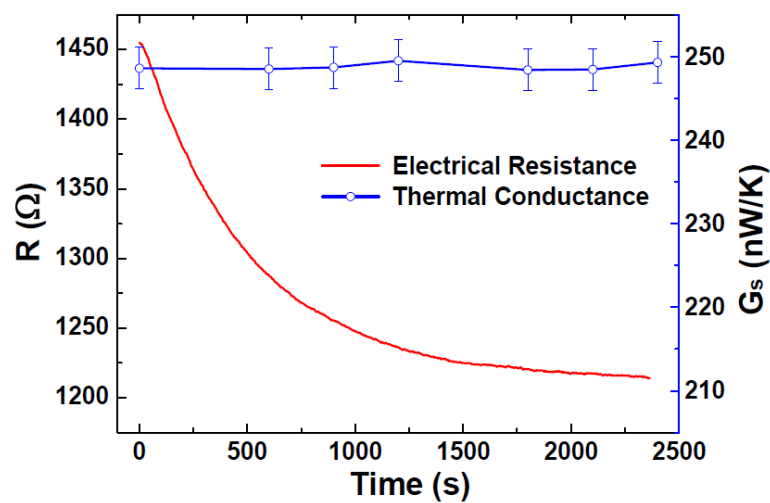
Figure 5.1: Measured R and G_s as a function of time when the graphene is exposed to a N_2 atmosphere $(1 \times 10^{-3}$ mBar) at 300 K.

Firstly, we exposed the pristine S4 to an N_2 atmosphere $(1.0 \times 10^{-3}$ mBar) at room temperature and monitored R *in situ*. Thermal conductance G_s measurements were performed at intervals of 5 to 10 min. As shown in Figure 5.1, R decreases after the gas is introduced, showing that the N_2 gas indeed adsorbs onto the graphene

surface and contributes a certain level of doping. The mechanism and rate of the charge transfer between graphene and N_2 will be discussed in detail in the next section.

On the other hand, it is observed that G_s stays almost unchanged even after 40 min of gas adsorption. Before drawing any conclusions, we need to first analyze the parasitic thermal conduction through the surrounding gas molecules, since the measured G_s is the total thermal conductance between the *heater* and *sensor* platforms. Based on the kinetic theory of gases, the mean free path λ of the N_2 molecules is:

$$\lambda = \frac{1}{\sqrt{2}\pi d^2 n} \tag{5.1}$$

where d is the physical size of an N_2 molecule, and n is the number of molecules per unit volume. For the diatomic elliptical N_2 molecule, the covalent radius of each N atom is 75 pm, hence the longest length of the ovoid is around 3 Å. The volume density n of N_2 is related to its partial pressure P in the test chamber by the ideal gas law:

$$PV = Nk_BT \tag{5.2}$$

$$n = \frac{N}{V} = \frac{P}{k_BT} \tag{5.3}$$

where k_B is Boltzmann's constant. Substituting Eq. (5.3) into Eq. (5.1), λ of N_2 at room temperature is:

$$\lambda = \frac{k_BT}{\sqrt{2}\pi d^2 P} = \frac{(1.38\times10^{-23})(300)}{\sqrt{2}\pi(3\times10^{-10})^2 P} = \frac{0.0104}{P} \tag{5.4}$$

where P is in Pascal, and λ is in meters. Hence, the mean free path of N_2 gas at a pressure of 1.0×10^{-3} mBar is 10 cm, almost 4 orders larger than the separation D between the centers of the *heater* and *sensor* platforms (21 μm).

The parasitic thermal conductance of the ambient N_2 can be written as:

$$G_{h-s,N_2} = \frac{\kappa_{N_2} A_{eq}}{D} \tag{5.5}$$

where κ_{N_2} is the thermal conductivity of the N_2 molecules, and A_{eq} is the equivalent surface area of the *heater* and *sensor* platforms. Since $\lambda \gg D$, the N_2 gas is in the molecular flow regime where wall collisions dominate, and according to the kinetic theory:

$$\kappa_{N_2} = \frac{CvD}{3} \tag{5.6}$$

$$G_{h-s,N_2} = \frac{CvA_{eq}}{3} \tag{5.7}$$

where C and v are the volumetric heat capacity and velocity of N_2 molecules, respectively. The specific heat of N_2 at constant pressure is 29.1 $Jmol^{-1}K^{-1}$, which translates into a volumetric C value of 1.17×10^{-3} $Jm^{-3}K^{-1}$ at $P = 1.0 \times 10^{-3}$ mBar by the ideal gas law. The velocity v (root-mean-square value) is obtained from the average kinetic energy:

$$\frac{1}{2}mv^2 = \frac{3}{2}k_B T \tag{5.8}$$

$$v = \sqrt{\frac{3k_B T}{m}} \tag{5.9}$$

where m is the mass of an N_2 molecule (4.65×10^{-26} kg), and hence $v = 517$ ms^{-1}. The equivalent surface area A_{eq} is 300 μm^2 from the design of the METS, and from Eq. (5.7), the estimated $G_{h-s,N_2} = 6.0 \times 10^{-11}$ WK^{-1}. This is well below the measured G_s of 2.5×10^{-7} WK^{-1}. For the temperature (77 K to 500 K) and pressure ranges (3.0×10^{-7} mBar to 1.0×10^{-3} mBar) of interest in all subsequent experiments, the parasitic thermal conductances through the ambient gases are all less than 1.0×10^{-10} WK^{-1}, and can be safely neglected.

For the graphene surface to be completely covered by an adsorbate, the monolayer formation time t_{ml} is given by:

$$t_{ml} = \frac{1}{\Gamma d^2} = \frac{4}{nvd^2} \qquad (5.10)$$

where Γ is the arrival rate of the gas molecules. Combining Eqs. (5.3) and (5.10):

$$t_{ml} = \frac{4k_B T}{vd^2 P} \qquad (5.11)$$

For N_2 molecules at 1.0×10^{-3} mBar and 300 K, t_{ml} is only 3.56 ms.
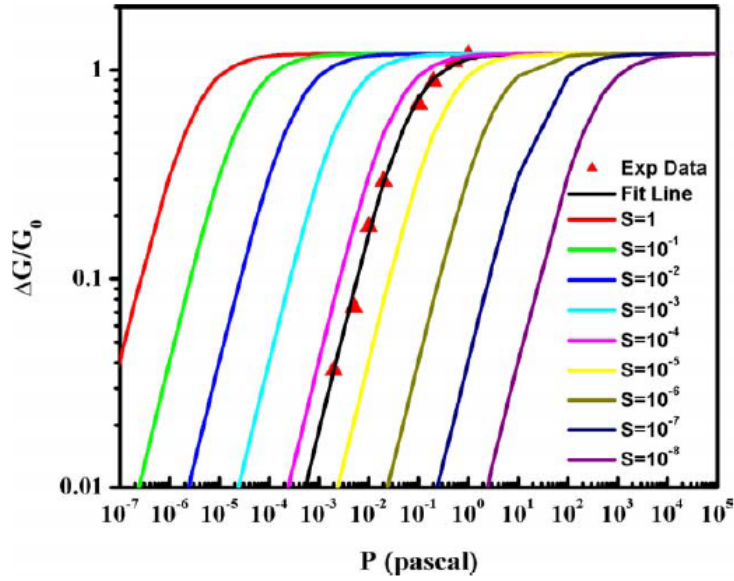
Figure 5.2: Calculated $\Delta G/G_0$ for p-type SWNT sensors versus NO_2 partial pressure (P) for NO_2 sticking coefficient (S) ranging from 1 to 10^{-8}. The solid triangles represent experimental data. Comparison between calculations (see the fit line) and experimental result suggests that the sticking coefficient $S = 4.5 \times 10^{-5}$ [115].

However, the underlying assumption for Eq. (5.10) is that all molecules striking the graphene surface from the gas phase adhere to the surface permanently, i.e., with a sticking coefficient $S = 1$. For graphitic surfaces, S is expected to be very small due to the lack of dangling bonds and hence poor adhesion for the gas molecules. The only available relevant data for S is from the work of Peng *et al.* on a CNT gas sensor [115] (Figure 5.2). By fitting the change in the electrical conductance at different pressures of NO_2, the obtained sticking coefficient S is 4.5×10^{-5}. In spite

of the difference in the gas species and surface curvatures, the same S was adopted in the study of ozone adsorption on graphene [116]. Although NO_2 is a polar molecule while N_2 is not, their interaction with the non-polar graphene is through van der Waals forces, which primarily depend on the size of the molecule. Hence, S for N_2 adsorption should be lower than that for NO_2. In our case, the same S of 4.5×10^{-5} is used as a rough reference, and the estimated t_{ml} is then ~80 s.

Since the duration of adsorption is 40 min, much longer than t_{ml} of 80 s, the graphene surface is expected to be fully covered by N_2 molecules. The little difference in G_s before and after N_2 adsorption shows that, unlike the electrical properties, the thermal transport properties of graphene are rather insensitive to gas adsorbates at room temperature.

There are a few studies on the phonon scattering on other crystal surfaces due to gas adsorption. Figure 5.3 shows the decrease in the phonon mean free path when a 10 Å thick layer of H_2, D_2 (deuterium) or Ne condenses on the surface of Si [117]. However, one should note that the experiments were conducted at low temperatures (< 2 K), where the adsorbates solidified into thin films. It was suggested that the phonons are not scattered by interface states or individual atoms/molecules adsorbed on the surface, but are strongly scattered by islands of discontinuous thin films, or by microscopic disorders in thicker films such as grain boundaries, voids and surface roughness [117]. In our experiment at room temperature, the adsorbed N_2 molecules certainly do not form a rigid structure, and the acoustic match between the 'soft' adsorbate layer and graphene can be very close to unity. Therefore, nearly all the phonons trying to enter the adsorbate layer will be specularly reflected at the interface, and hence not scattered, i.e., the thermal transport in graphene is minimally affected by the adsorbates. This can also explain why the phonon scattering at the graphene-

adsorbates interface appears to be much weaker than that at the graphene-substrate

interface, because more phonons will 'leak' into the 'harder' substrate as a result of a

much smaller acoustic mismatch.
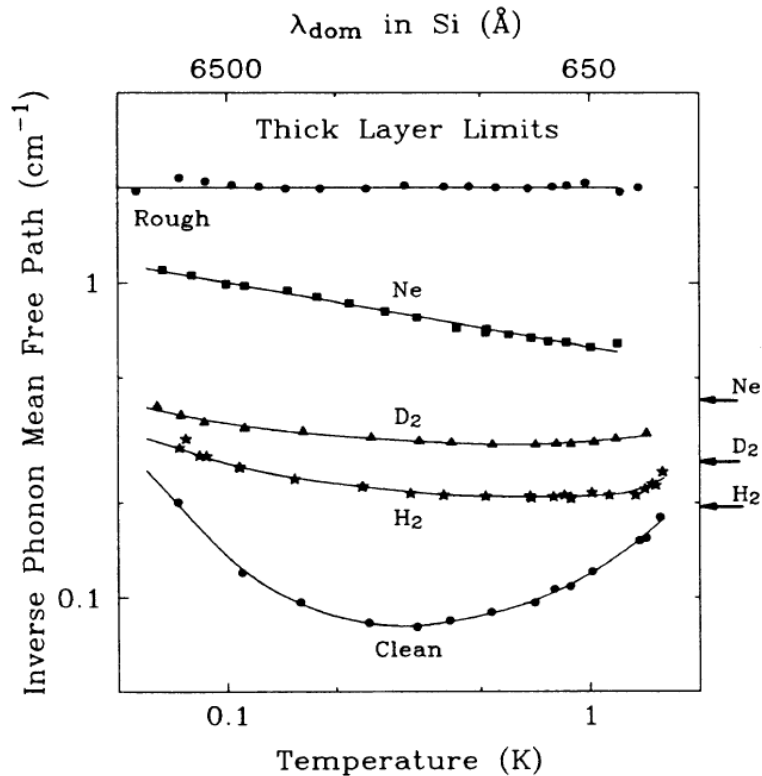
Figure 5.3: Thick layer maximum scattering limits for condensed gas films of Ne, D_2 and H_2. Films up to 10 Å thick were studied [118]. Arrows on the side indicate the value of l^{-1} expected on the basis of acoustic mismatch between Si and these condensed gases for isotropic angles of incidence, and correspond to a probability for specular reflection of 98% for H_2, 95% for D_2, and 85% for Ne (Monte Carlo calculation by Fischer) [117].

The effects of N_2 adsorption on the thermal properties of a SiO_2 thin film had

also been theoretically studied [119] (Figure 5.4). The thermal conductivity of SiO_2 is

found to be reduced by 12 % for a 50 % surface coverage when submitted to a

stationary N_2 environment. In the simulation, the adsorbed N_2 molecules were

assumed to be at a depth of 0.5 Å below the SiO_2 surface. However, due to the lack of

dangling bonds, gas adsorbates such as N_2, Ar, and SF_6 can only reside at several

angstroms above the graphene surface [120] and interact with graphene through weak

van der Waals forces. The 'embedded' molecules responsible for the substantial

phonon scattering in SiO_2 can never exist on graphene surfaces, and this highlights an important difference between layered materials like graphene and other systems with three-dimensional lattices.
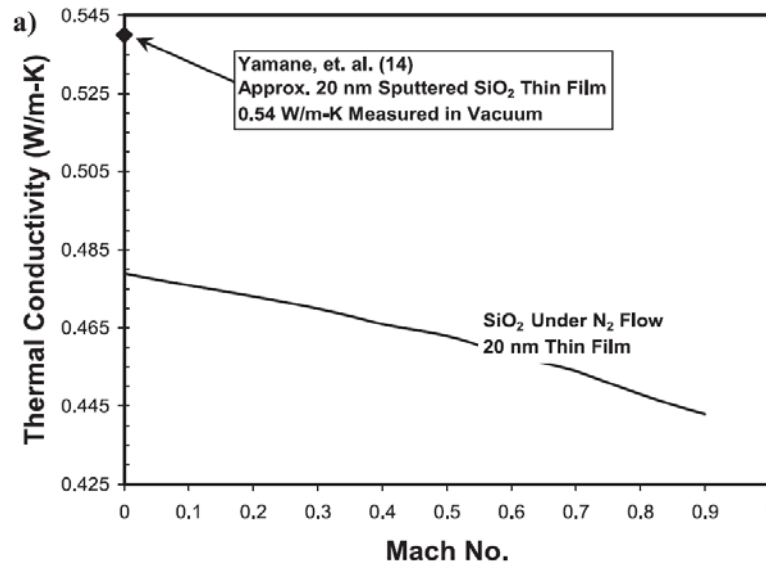
Figure 5.4: The SiO_2 thin-film model thermal conductivity is correlated to experimental data (solid diamond) then submitted to a N_2 environment (solid line) to characterize the effects on thermal conductivity. The flow velocity is increased to Mach 0.9 to obtain predicted trends to the thermal conductivity behavior. Thermal conductivity is predicted to decrease by 12% when the stationary flow N2 atmosphere is introduced [119].

When S4 was annealed again and exposed to an O_2 atmosphere, a similar result was obtained where G_s showed negligible differences before and after the adsorption. Therefore, although we cannot quantify the phonon scattering due to adsorbed N_2 or O_2 molecules, it is at least clear from our experimental results that for real-life exposed devices operating under ambient conditions, the air molecules covering the graphene surface will not adversely affect its thermal conductivity.

Experiments were also carried out at 77 K. Since it is much easier for gas adsorption to take place at lower temperatures, we expect to see a more significant change in the electrical and thermal properties of graphene in various gas ambients.

The sample was annealed at 600 K for 2 h in vacuum and cooled to 77 K within 10 s. As discussed earlier, monolayer formation time on the graphene surface

is rather slow due to the small sticking coefficients. Under vacuum (3×10^{-7} mBar) condition, it can be up to several hours from Eq. (5.11), and hence the contaminants in the vacuum chamber will have little effect on the measurements. The sample was first exposed to an Ar atmosphere (1×10^{-3} mBar) as a control experiment, and its 4-point electrical resistance R and Seebeck coefficient S were monitored *in situ*, as plotted in Figure 5.5. The positive sign of S indicates a p-type doping of graphene, possibly from the metal contacts. The values of S and R barely change during the 40 min adsorption period, which is expected given the inert nature of Ar.
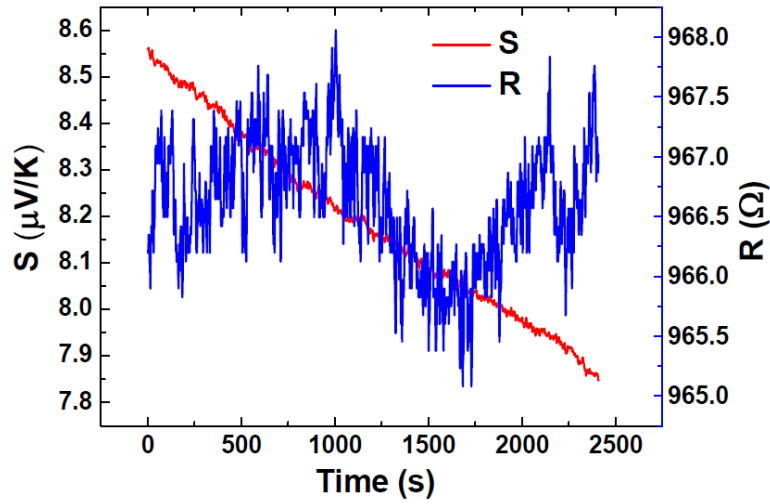
Figure 5.5: Measured S and R as a function of time when the graphene is exposed to an Ar atmosphere (1×10^{-3} mBar) at 77 K.

The sample was then annealed and exposed an N_2 atmosphere (1×10^{-3} mBar) at 77 K. As shown in Figure 5.6(a), S decreases from +4.0 μV/K to -7.8 μV/K, which implies that the adsorbed N_2 molecules contribute a substantial n-type doping to the graphene. At *time* = 80 s, the peak in R coincides with $S = 0$ μV/K (indicated by the pink dashed lines), where the net charge in the graphene is approaching zero (charge neutrality point). The interesting n-type doping behavior of N_2 on graphene has never been reported, and will be thoroughly studied in the next section.

Since the adsorption of SF_6 on graphite has been extensively studied [120, 121], we repeated the experiment in an SF_6 atmosphere (1×10^{-4} mBar) at 77 K. The pressure was set 10 times lower than that of Ar and N_2 because the doping effect of SF_6 was found to be much stronger. As shown in Figure 5.6(b), S decreases to a minimum value of -4.5 µV/K in less than 100 s, indicating an n-type doping effect of SF_6. The decrease in the magnitude of S after *time* = 100 s is a characteristic of graphene in the high charge carrier density regime, as illustrated in Figure 4.13.
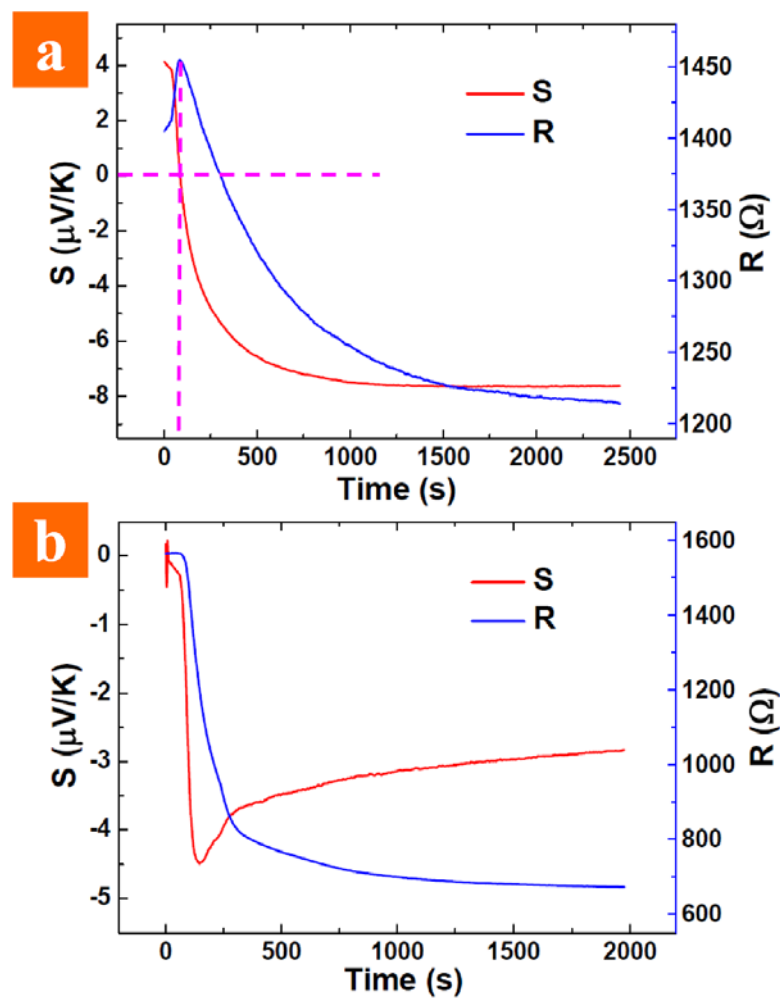
Figure 5.6: Measured S and R as a function of time when the graphene is exposed to an atmosphere of (a) N_2 (1×10^{-3} mBar) and (b) SF_6 (1×10^{-4} mBar) at 77 K.

The thermal conductance of the graphene with adsorbed SF_6 molecules was measured from 77 K to 375 K (still in SF_6 environment), and the results are plotted in Figure 5.7. As the sample temperature increases (forward) and decreases (backward),

a hysteresis is observed in the measured G_s between 77 K and 158 K, and the data points in the backward sweep coincide with those from pristine S4. It seems that the adsorbed SF_6 molecules had arranged themselves into continuous multilayer thin films (since a monolayer of SF_6 would not have a noticeable thermal conductance) which provide a parallel thermal conduction path that can contribute a finite G_s up to 158 K. For a better understanding of the event, we have also plotted the $R - T$ curve. As T increases from 77 K to 158 K, R shows a gentle decrease as expected due to thermal generation of charge carriers in graphene (see Figure 4.12). However, as T increases further, R suddenly increases. Note that the trends of G_s and R both change at the same T. The abrupt decrease in the charge carrier concentration indicates desorption of SF_6 from the graphene surface, which can also explain the hysteresis in G_s below 158 K. During the backward sweep, SF_6 starts to re-adsorb upon cooling and causes a decrease in R towards its initial value. We will now try to find the two missing pieces of the puzzle: why SF_6 desorbs from the graphene surface at this particular T of 158 K; and why SF_6 re-adsorbed upon cooling cannot contribute a measurable thermal conductance.
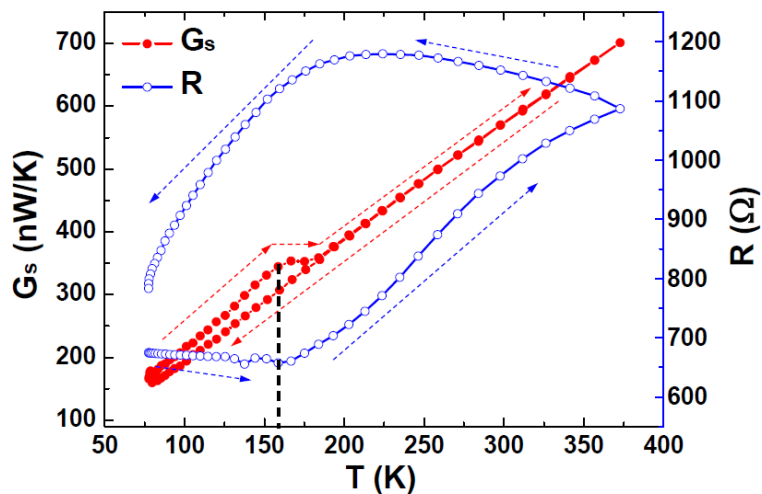
Figure 5.7: Measured G_s and R as a function of temperature after exposing the graphene to a SF_6 atmosphere (1×10^{-4} mBar) at 77 K. The measurements were carried out in the same SF_6 atmosphere, and the dashed lines indicate the direction of temperature sweeps.

The 2D critical point (T_c) of SF_6 on graphite has been experimentally obtained previously as 156 ± 1 K [121], above which the correlation length diverges, i.e., the adsorbed SF_6 layer loses its long-range order. The phase diagram of an SF_6 monolayer on graphite is shown in Figure 5.8, where a transition of SF_6 from an incommensurate solid (IC2) to a liquid (L) phase occurs at T_c. This suggests that in our case, at 158 K ($\sim T_c$), the layer of SF_6 closest to the graphene surface has possibly experienced a solid-liquid phase transition that breaks down its continuity, which in turn disturbs the upper layers and results in a desorption. However, this is only a hypothesis as we do not have the necessary facilities (ultrahigh vacuum, infrared spectroscopy or x-ray diffraction etc.) to carry out a systematic surface study.
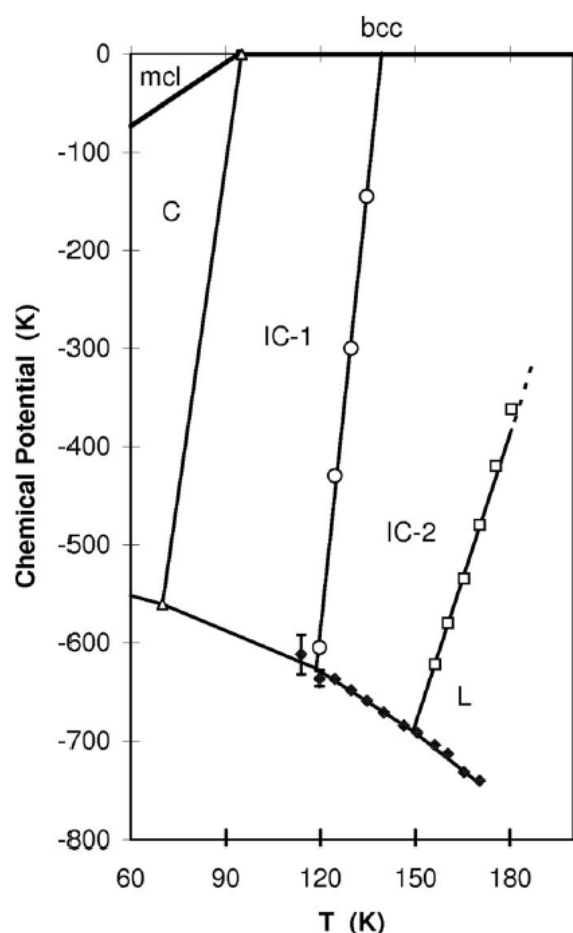
Figure 5.8: SF_6 monolayer phase diagram in the intensive variables chemical potential and temperature. Solid symbols are measured layer condensation points. Open symbols are measured (centers of) phase transitions. C = commensurate 2 × 2 monolayer; IC1 and IC2 are incommensurate solid phases; L = liquid monolayer; mcl = monoclinic bulk; bcc = body centered cubic bulk. Chemical potential is measured relative to monolayer—bcc bulk coexistence (extrapolated) [121].
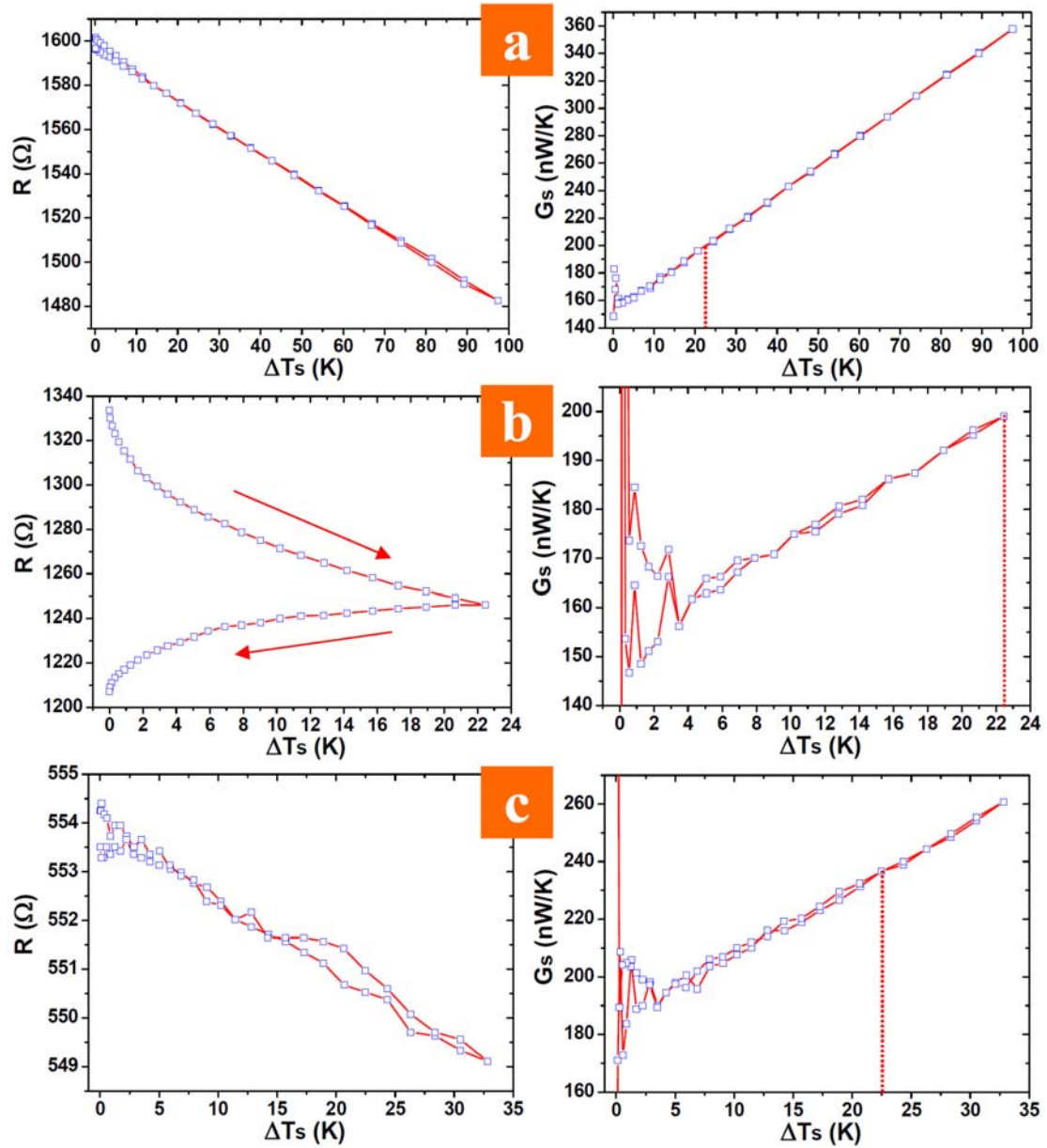
Figure 5.9: Measured R and G_s of the graphene sample when exposed to a SF$_6$ atmosphere (1×10^{-4} mBar) at 77 K: (a) pristine graphene right before the exposure, (b) exposed for 5 min, and (c) exposed for 95 min. Red dashed lines indicate a sample temperature of 100 K ($\Delta T = 22.5$ K).

Furthermore, we have also obtained the time evolution of G_s as SF$_6$ molecules progressively adsorbed onto the graphene surface at 77 K. For pristine graphene at *time* = 0 (Figure 5.9a), no hysteresis is observed in both R and G_s, showing that the results are not affected by the background contaminants. The sample was then exposed to SF$_6$ gas (1×10^{-4} mBar) at *time* > 0, and electrical and thermal measurements were performed every 5 min (the measurement itself takes 2 min, and

the interval is 3 min). For G_s measurements, the sample temperature was swept from 77 K to 115 K (well below 158 K) to avoid desorption of SF_6. At *time* = 5 min (Figure 5.9b), R keeps decreasing due to strong doping from SF_6, and G_s shows little change from that of pristine graphene. At *time* = 95 min (Figure 5.9c), R no longer decreases showing saturation of the doping, while G_s exhibits a significantly higher value than at *time* = 0.
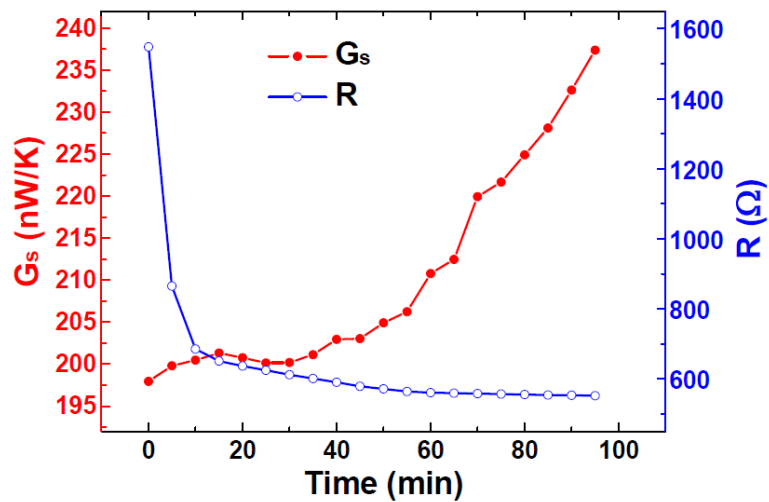
Figure 5.10: Measured G_s (at 100 K) and R as a function of time when the graphene is exposed to a SF_6 atmosphere (1×10^{-4} mBar) at 77 K.

The time dependent G_s measured at 100 K (indicated by vertical dashed lines in Figure 5.9) and R are plotted in Figure 5.10. It is observed that G_s stays relatively constant for the first 30 min, and then steadily increases. We propose that the increase in G_s is due to the multi-layer stacking of SF_6 adsorbates that acts as a parallel thermal conduction path. The first 30 min is a settling time for the SF_6 molecules to arrange themselves into a densely packed solid phase, and a longer exposure time thereafter will lead to a thicker SF_6 thin film forming on the graphene surface, and hence a higher G_s. This settling time also explains why G_s did not increase during cooling in Figure 5.7, which was too fast for the thin film formation (~ 1 min). Nevertheless, R shows a rapid decrease at the start, and saturates after 15 min. This is reasonable

because the SF_6 layers stacked further away from the surface would have a weaker interaction with the graphene, and hence a diminishing doping effect. This is consistent with the work of Mann *et al.* [122], which studied the thermal properties of CNTs in various gas ambients and showed that the adsorbed gas molecules, in particular solidified CO_2 at low temperatures, assist in the relaxation of hot phonons.

A similar hysteresis in G_s was also observed during adsorption of N_2 and Ar gases as shown in Figure 5.11. Unfortunately there is no published work on their adsorption on graphitic surfaces, and the exact mechanism will have to be a subject of future work.
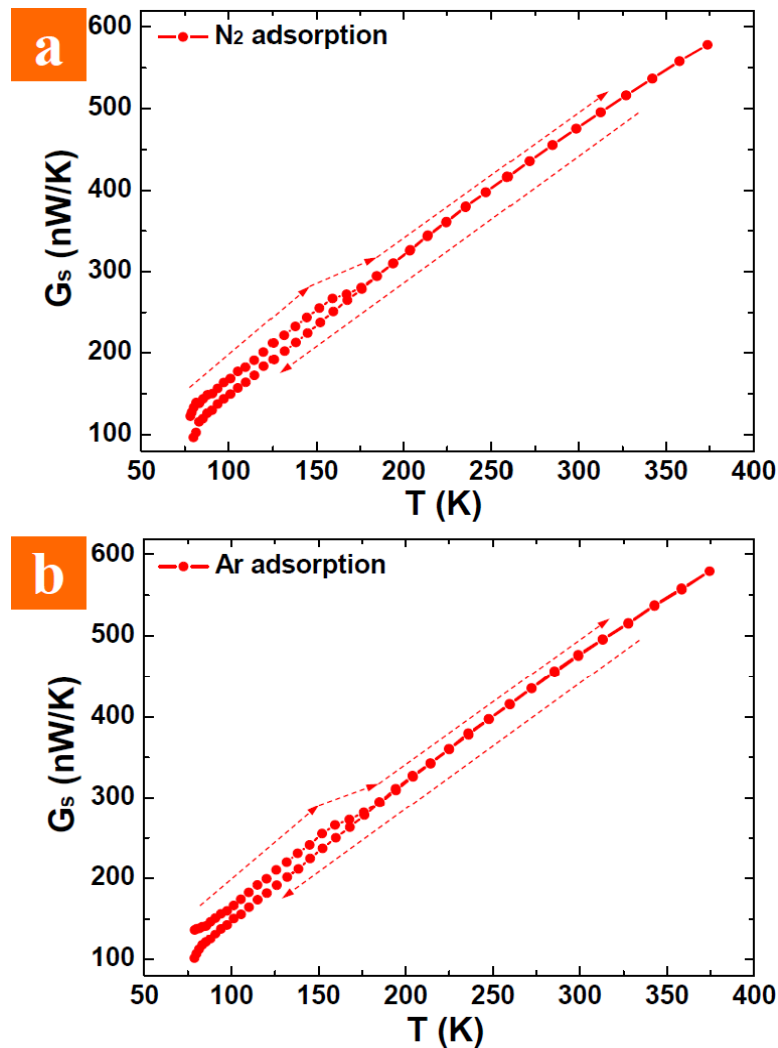
Figure 5.11: Measured G_s as a function of temperature after exposing the graphene to an atmosphere of (a) N_2 (1×10^{-4} mBar) and (b) Ar (1×10^{-3} mBar) at 77 K. The measurements were carried out in the respective atmospheres, and the dashed lines indicate the direction of temperature sweeps.

5.2 Doping graphene with nitrogen

In the previous section, we described the discovery of an interesting n-type doping effect of N_2 adsorbed on the graphene surface. However, limited by the design of the METS, we are unable to 'gate' (apply an electric field perpendicular to the graphene basal plane) the device, and electrical properties are only inferred from the Seebeck coefficient S. We can easily discern the majority charge carrier type from the sign of S, but quantitative analysis of the electron concentration n is difficult due to the complex relationship between S and n (see Figure 4.13).
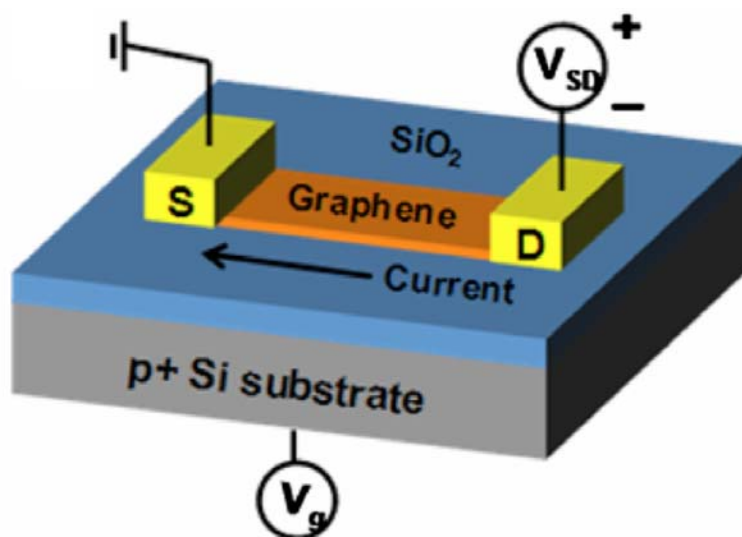
Figure 5.12: Schematic structure of graphene FET on SiO_2 substrate with heavily p-doped Si substrate serving as the back gate. Here S and D refer to the source and drain metal contacts, respectively [123].

In view of this, we fabricated a batch of single-layer graphene (SLG) devices on an oxidized Si substrate with 285 nm thick SiO_2. Figure 5.12 shows the schematic of a typical device [123], where Cr/Au (5/55 nm) source/drain electrodes were deposited on the graphene flakes by EBL for electrical resistance (R) measurements, and the degenerately doped Si substrate acts as a gate electrode. The device structure resembles that of a metal-oxide-semiconductor field-effect-transistor (MOSFET). When a gate voltage (V_g) is applied on the Si substrate, it induces a certain carrier

concentration at the graphene/oxide interface through a capacitive effect of the oxide layer. For instance, applying a positive V_g will cause accumulation of negative charges (electrons) at the interface and hence dope the graphene n-type, while a negative V_g will dope the graphene p-type.

At the six corners of the Brillouin zone where the conduction and valence bands meet (Dirac points), the carrier concentration in graphene is at the minimum, which gives a maximum R. Note that residual charges still exist in graphene as localized electron-hole puddles with equal amount of electrons and holes [124, 125]. Here we are only interested in the net charge in the graphene sample either induced by the gate bias or from the gas adsorption effect.

We define V_{dp} as the value of V_g corresponding to the peak in the $R - V_g$ graph. For undoped graphene, $V_{dp} = 0$ V. If the graphene is initially doped p-type by other means, applying a certain positive V_g can counter-dope it and balance the charges, hence $V_{dp} > 0$. Similarly for n-type graphene, $V_{dp} < 0$. The electron concentration n_i induced by V_g is:

$$n_i = \frac{CV_g}{A} = V_g \frac{\varepsilon_r \varepsilon_0}{d}$$
(5.12)

where C and d are the capacitance and thickness of the SiO_2 layer, respectively. Substituting the relevant values into Eq. (5.12), we have:

$$n_i = (7.56 \times 10^{10}) V_g \text{ cm}^{-2}\text{V}^{-1}$$
(5.13)

At V_{dp}, the net charge in graphene approaches 0, and hence the electron concentration n in graphene can be obtained as:

$$n = -(7.56 \times 10^{10}) V_{dp} \text{ cm}^{-2}\text{V}^{-1}$$
(5.14)

Figure 5.13 (black line) shows the typical $R - V_g$ graph of a pristine SLG flake (V_{dp} near 0) annealed in vacuum. However, when exposed to ambient air (red line),

V_{dp} quickly shifts to a very large positive value, indicating a strong p-type doping from the adsorb air. It is widely accepted that the charge transfer is from the hydroxyl group [126, 127] formed by the oxygen and water molecules in air through a chemical reaction:

$$O_2 + 2H_2O + 4e^- \rightarrow 4OH^- \qquad (5.15)$$

Nevertheless, the doping effect of the most abundant constituent of air, N_2 gas, has not been reported, possibly because it is obscured by the much stronger counter effect from O_2 and H_2O.
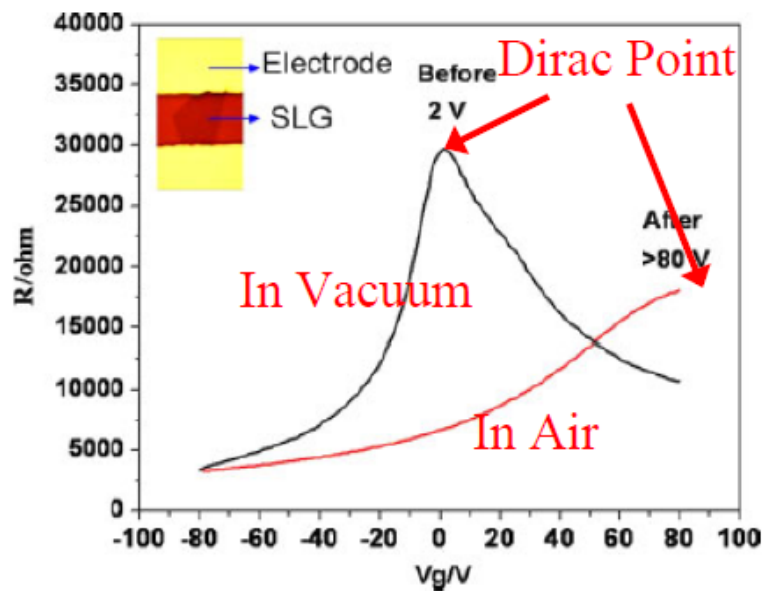
Figure 5.13: Transport properties of SLG (Resistance vs. gate voltage) before annealing, after annealing and exposed to air ambient. The inset is optical image of SLG and two electrodes. The gate voltage corresponds to the highest resistance reveals the neutral point [127].

The SLG sample was first annealed in vacuum at 500 K for 24 hours to remove possible contaminants from the fabrication process and random adsorbates. After annealing, $V_{dp} = 0$ V (Figure 5.14, black line) showing the graphene is pristine. The asymmetry in the $R - V_g$ plots is caused by localized electron-hole puddles in the graphene, which gives a small local maximum of R at $V_g = -15$ V. This is often

observed in graphene samples prepared on SiO_2 substrate, and will not affect our results and discussions hereafter.

The sample was exposed to an N_2 atmosphere (1.5×10^{-4} mBar) at 300 K, and R was measured as a function of V_g using a semiconductor parameter analyzer (Keithley 4200-SCS) every 2 min (each sweep took ~ 10 s). The results are shown in Figure 5.14, where V_{dp} steadily shifts to the negative side, showing an increase in the electron concentration in the SLG (n-type doping). To exclude the effects of other gases, the chamber was baked overnight at 300 °C before the experiments, and a Residue Gas Analyzer (RGA) was installed to monitor the gas composition. Figure 5.14 (inset) shows the partial pressures of common residual gases such as water and hydrogen, which are all in the order of 10^{-8} mBar. Hence, the observed doping effect is indeed due to adsorbed N_2 molecules.
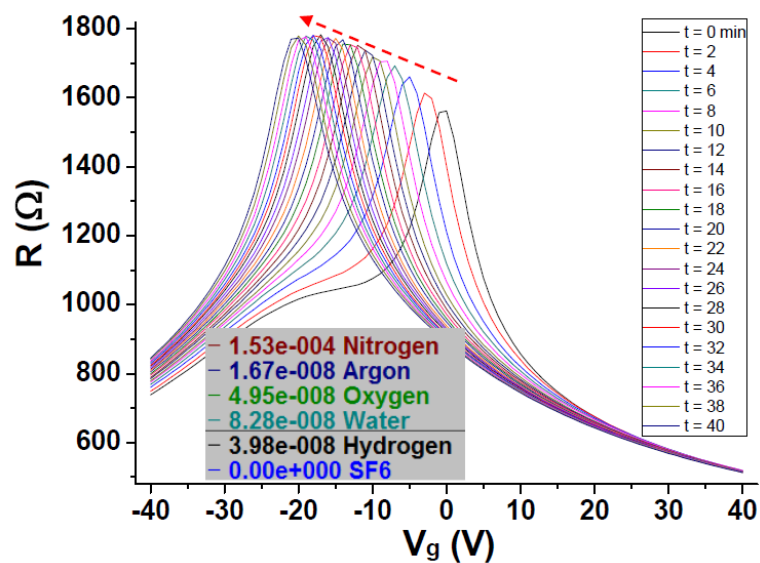
Figure 5.14: Measured R as a function of V_g when the sample is exposed to a N_2 atmosphere (1.5×10^{-4} mBar) at 300 K. Interval between measurements is 2 min. Inset: partial pressures (mBar) of gases in the test chamber measured by RGA.
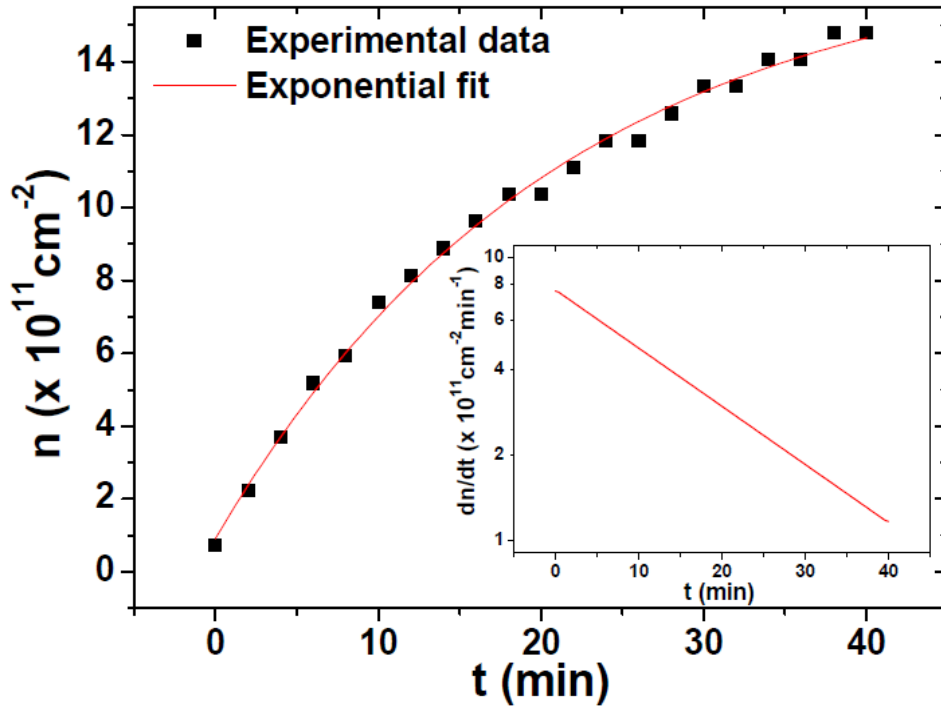
Figure 5.15: Extracted electron concentration in graphene as a function of time during N_2 adsorption (black squares), fitted with an exponential function (red line). Inset: Rate of charge transfer as a function of time, showing $\log(dn/dt) \propto -t$, i.e. $dn/dt \propto \exp(-t/\tau)$.

The electron concentration n is calculated from Eq. (5.14) and plotted as a function of time t in Figure 5.15, which fits well with an exponential function. The rate of charge transfer calculated from the fitting line is plotted in the inset. The obtained relationship is in the form of:

$$dn/dt \propto \exp(-t/\tau) \tag{5.16}$$

where τ is the time constant for adsorption. This agrees well with the relationship expected from the conventional Langmurian kinetics for molecular adsorption [126].
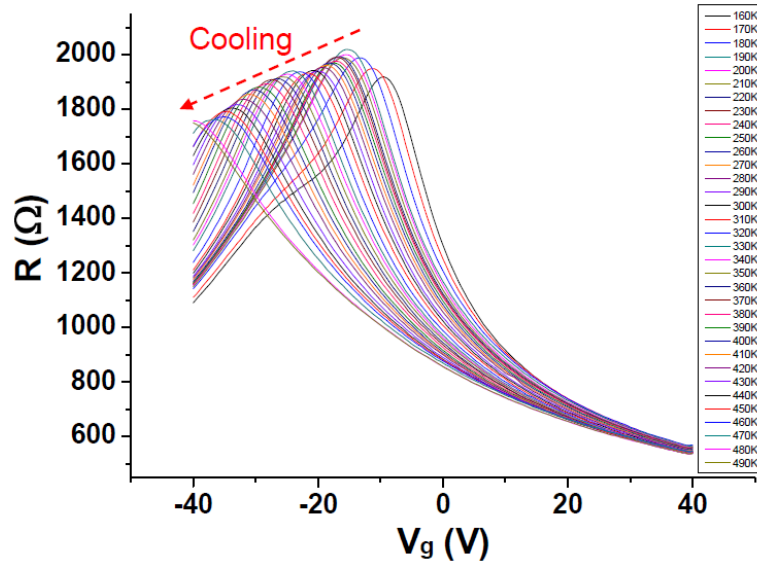
Figure 5.16: $R - V_g$ plots obtained when sample was cooled in a N_2 atmosphere from 490 K to 160 K at -10 K steps.

We have also studied the temperature dependence of the charge transfer. The sample was first cleaned by annealing at 500 K in vacuum until V_{dp} returned to 0 V, and then exposed to an N_2 atmosphere (1.5×10^{-4} mBar). The sample temperature was lowered by 10 K every hour in a stepwise manner. It is found that at each temperature, V_{dp} will saturate within the 1-hour window, indicating that the charge transfer process has reached steady state. The $R - V_g$ plots obtained after the saturation points are shown in Figure 5.16. V_{dp} becomes more negative during cooling, and the stronger doping effect is attributed to more N_2 molecules adsorbing on the graphene surface at steady state at lower temperatures.
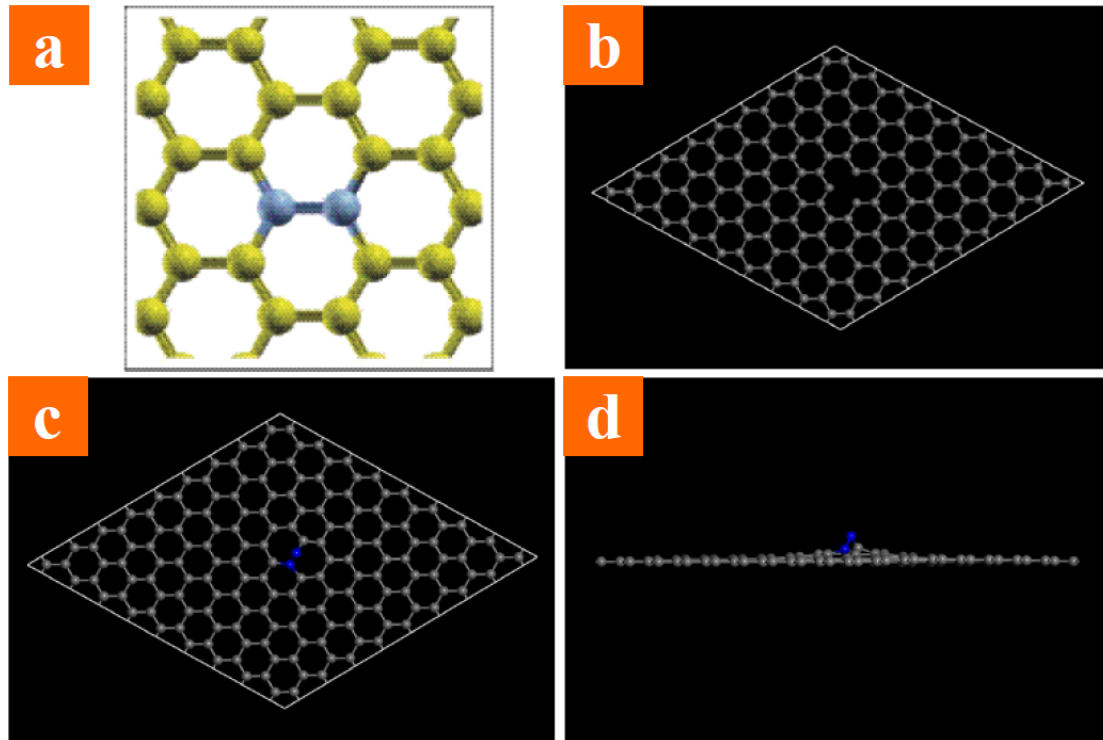
Figure 5.17: (a) Schematic of N_2 adsorption on double-vacancies [128]. (b) A 9×9 supercell constructed with a single-vacancy in our simulation. (c) Top view of the relaxed system. (d) Side view of the relaxed system.

We have theoretically studied the mechanism for the charge transfer between adsorbed N_2 molecules and graphene with a density functional theory (DFT) approach. Four types of adsorption sites are considered: (1) pristine graphene, (2) Stone-Wales defects, (3) double-vacancy defects, and (4) single-vacancy defects. It is found that N_2 molecules interact very weakly with pristine graphene and SW defects, and cannot lead to an appreciable doping. This is consistent with the weak interaction observed between N_2 and CNT [129]. On double-vacancies, it is reported that a N_2 molecule will decompose into 2 N atoms that substitute into the positions of the missing C atoms, as illustrated in Figure 5.17(a) [128]. Our calculation also shows similar results, and the N atoms in the graphene lattice act as n-type dopants. These N atoms are chemically bonded to the neighboring C atoms, and will be desorbed only at high temperatures. This is different from our observation that V_{dp} readily returning to 0 V

upon annealing at 500 K in vacuum. Thus adsorption of N_2 at double-vacancies is not the dominant mechanism for the observed doping effect.
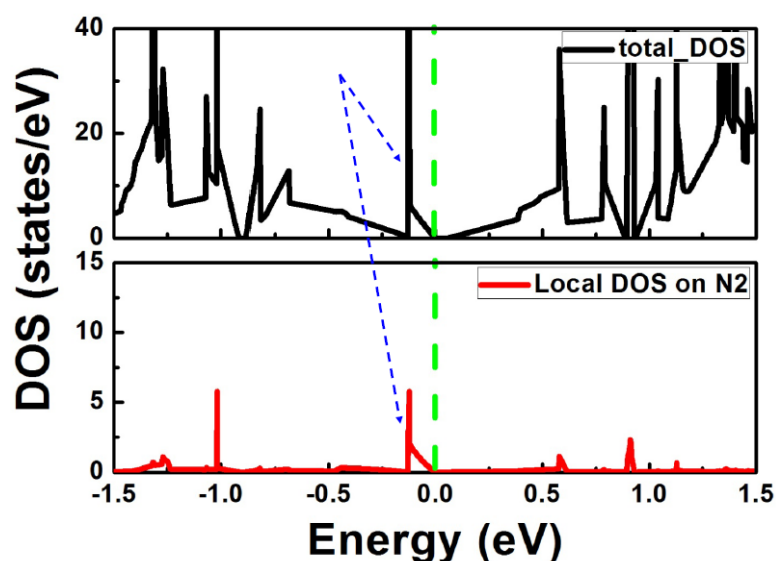
Figure 5.18: DOS of graphene with N_2 adsorbed on a single-vacancy (upper black plot) and local DOS of N_2 (lower red plot) simulated using a DFT approach. The N_2-induced 'defect level' is indicated by the blue dashed lines.

For adsorption on single-vacancies, a 9×9 supercell was constructed for each vacancy (Figure 5.17b) corresponding to a defect density of ~ 0.6 %, and a periodic boundary condition was used. An N_2 molecule was placed at the vacancy, and Figures 5.17(c) and (d) show the top and side view of the system relaxed by minimizing the surface energy. The lines connecting the N and C atoms are to illustrate the interactions, and do not represent real chemical bonds. Note that N_2 does not decompose, and adsorbs as a molecule. The calculated density of states (DOS) of graphene with adsorbed N_2 molecules, as well as the local DOS of the N_2 molecule itself, is shown in Figure 5.18. It is found that the N_2 induces a 'defect level' (indicated by blue dashed arrows), which lies slightly below the Fermi level of graphene and is hence occupied. Electrons can only be excited to the conduction band, leading to electron conduction, i.e., n-type doping. In this case, N_2 is only partially bonded to the

lattice C atoms, and is likely to be recoverable at moderate temperatures such as 500 K.

In addition to the four cases discussed above, the graphene edges can also be important adsorption sites. To study the edge effects, we covered the entire sample with a layer of PMMA and opened a small window on the graphene basal plane, as shown in Figure 5.19. The sample still exhibits an n-type behavior when exposed to the same N_2 atmosphere, but the doping effect is much weaker with $V_{dp} >$ -5 V at 300K. By comparing the doping effect of N_2 before and after covering the graphene edges, it is evident that the edges play a critical role in the charge transfer. Unfortunately, the assumption of a periodic boundary condition is not longer applicable in this case, and it is difficult to simulate the scenario with our DFT approach. What is happening at the edges could be an interesting topic for future research.

Figure 5.19: Graphene edges covered by a layer of PMMA, with only a portion of the graphene basal plane exposed to a N_2 atmosphere. Red dashed lines indicate the edges of the SLG. Inset: optical image of the graphene flake before device fabrication.

Furthermore, to ensure that the charge transfer is from molecular N_2 and not from the constituent N atoms like in the double-vacancy case, we also introduced

atomic N into the chamber using a remote N_2 plasma source, where the N^+ and N_2^+ ions were trapped by an ion reflector grid. The sample was placed far away (~30 cm) from the plasma and faced parallel to the incoming gas flux, thus any residual ion damage to the graphene lattice is negligible. Note that the gas environment comprised both N_2 molecules and N atoms. The sample was doped n-type after the gas exposure, similar to the results obtained earlier for pure N_2 gas adsorption. However, upon annealing at 500 K for up to 6 hrs, V_{dp} stayed approximately constant at -20V, as shown in Figure 5.20. For the pure N_2 case, V_{dp} readily returns to 0 V after annealing at 500 K for 2 hrs. Hence this stable doping is attributable to the adsorption of atomic N at vacancies and graphene edges. This is consistent with the stable n-type doping effect observed when N atoms are incorporated into the graphene lattice by other methods [27, 28].
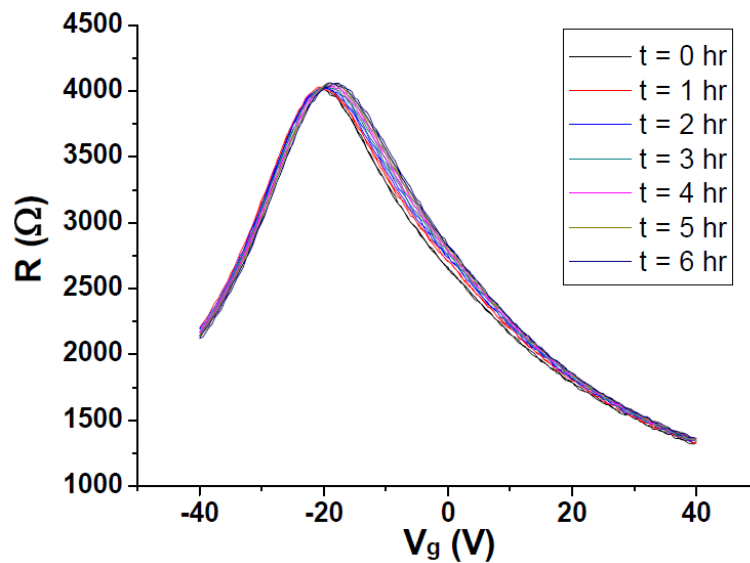
Figure 5.20: $R - V_g$ plots obtained during annealing at 500 K after the device was exposed to a N_2+N gas environment.

5.3 Electric-field-controlled doping of graphene
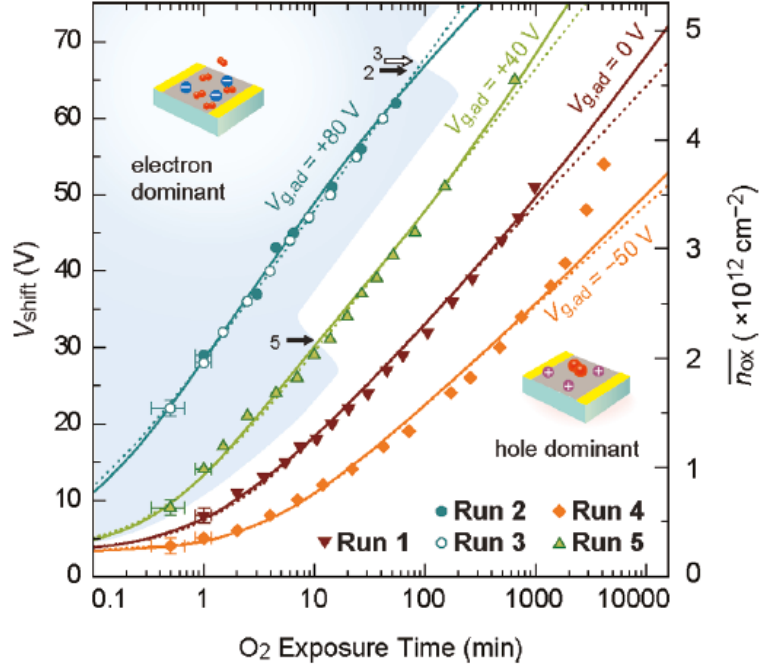
Figure 5.21: Time dependence of V_{shift} and doping density n_{ox} with doping due to the O_2 exposure under application of various $V_{g,ad}$. Solid and dotted curves are the fits based on the H kinetics and the P kinetics, respectively. The curve fitting is made in the range of exposure time below 2000 min [126].

In an O_2 adsorption study on graphene by others, the rate of charge transfer was found to be affected by V_g (or by the electric field perpendicular to the graphene surface) applied during the gas adsorption [126]. As shown in Figure 5.21. The shift in V_{dp} is much faster for positive V_g, and slower for negative V_g.

Inspired by their findings, we have also investigated the effect of V_g on the charge transfer from N_2. The sample was kept in a N_2 atmosphere (1.5×10^{-4} mBar) at 300 K while different V_g was applied (30 min interval between different V_g). As shown in Figure 5.22, when $V_g = 0$ V, V_{dp} saturated at -34.5 V. When $V_g = -30$ V, V_{dp} shifted to < -40 V showing increased doping concentration. When $V_g = +30$ V, V_{dp} increased to -29 V, showing a lower doping level than at $V_g = 0$ V. When $V_g = 0$ V again, V_{dp} returned to the starting point of -35 V.
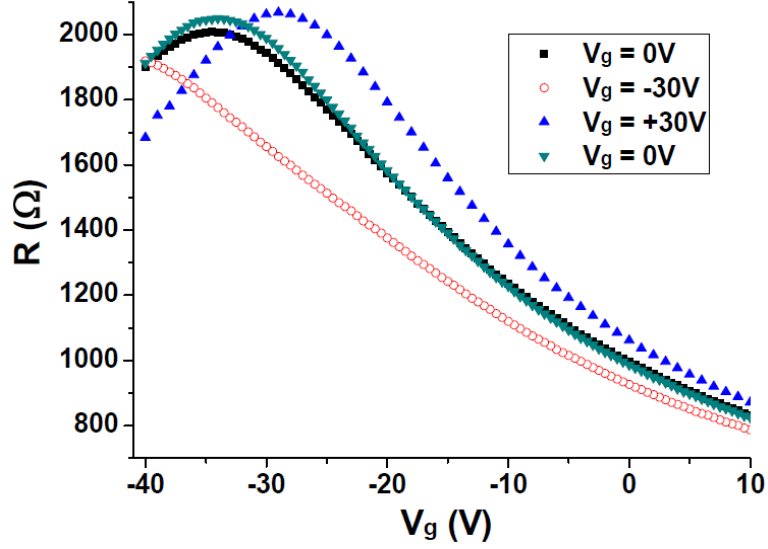
Figure 5.22: $R − V_g$ plots obtained when the sample was kept in a N_2 atmosphere (1.5×10^{-4} mBar) at 300 K while V_g was changed every 30 min in the sequence shown in the legend.

It is evident that the charge transfer from N_2 is reduced by applying a positive V_g and enhanced by a negative V_g, which is exactly the opposite to that observed in O_2 adsorption. It is suggested that in the O_2 case, electrons in graphene have to overcome an energy barrier to reach a transition state before transferring to the O_2 molecules as shown in Figure 5.23 [126]. Applying a positive V_g increases the electron concentration in graphene and elevates its Fermi level. The activation energy for electron transfer from graphene to the transition state becomes lower, and hence the charge transfer is enhanced. Our observation in the V_g-dependent doping from N_2 can also be explained by a similar mechanism. In the N_2 case, applying a positive V_g will still elevate the Fermi level of graphene. However, since electrons transfer from the N_2 molecules to graphene, this actually increases the activation energy and hence reduces the charge transfer between graphene and N_2. Similarly, applying a negative V_g will enhance the n-type doping effect of adsorbed N_2.
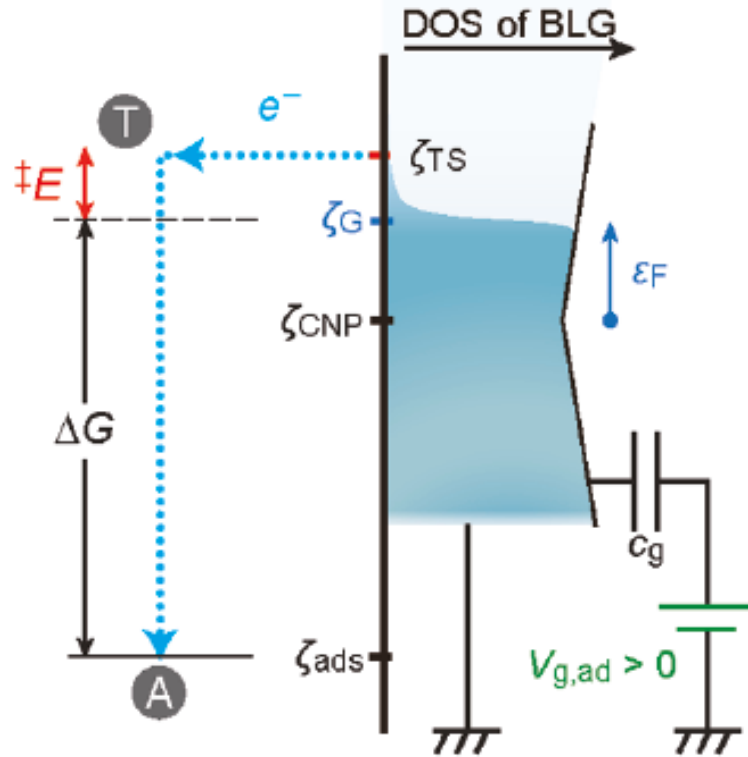
Figure 5.23: Schematic energy diagrams of the kinetics of O_2 adsorption (H kinetics). Path for electron transfer in this model is shown by the blue dotted arrow; electrons in BLG are transferred to O_2 molecules via the transition state (the circled T), giving the adsorbed oxygen species (the circled A). The activation energy, the free energy change, and the level of the CNP are denoted by ‡E, ΔG, and ζ_{CNP}, respectively [126].

It is interesting that O_2 and N_2 have opposite doping types, and their V_g dependence of the charge transfer is also opposite. If we mix the two gases in a certain ratio such that their doping effects cancel each other at $V_g = 0$ V, then the overall doping type of graphene can be controlled by the polarity of V_g. For instance, a positive V_g enhances p-doping from O_2 and suppresses n-doping from N_2. The balance of charge carriers is disturbed, and we will have a p-type graphene device. Similarly a negative V_g leads to an n-type device.

After a few trial experiments, we have optimized the gas composition as N_2 at 1.03×10^{-4} mBar and O_2 at 7.28×10^{-7} mBar. As illustrated in Figure 5.24, when exposed to the gas mixture, V_{dp} of the graphene stays at 0 V (black symbols) without any gate voltage. When V_g changes to −40 V, V_{dp} saturates at −3.0 V (red); and when

V_g is set to +40 V, V_{dp} shifts to +10.5 V (green). Similar results are obtained when V_g is switched again to −40 V (blue, V_{dp} = −2.5 V) and +40 V (turquoise, V_{dp} = +12.0 V). It is evident that the doping type of graphene follows the polarity of V_g. By making local gate electrodes underneath different regions of the same graphene flake, the doping type and concentration at each position can be individually controlled, i.e. the region above a positively biased gate will behave as p-type and the region above a negatively biased gate will behave as n-type in the mixed O_2/N_2 gas ambient. Although the doping process is rather slow, it can be useful in forming versatile p-n junctions in graphene electronics.
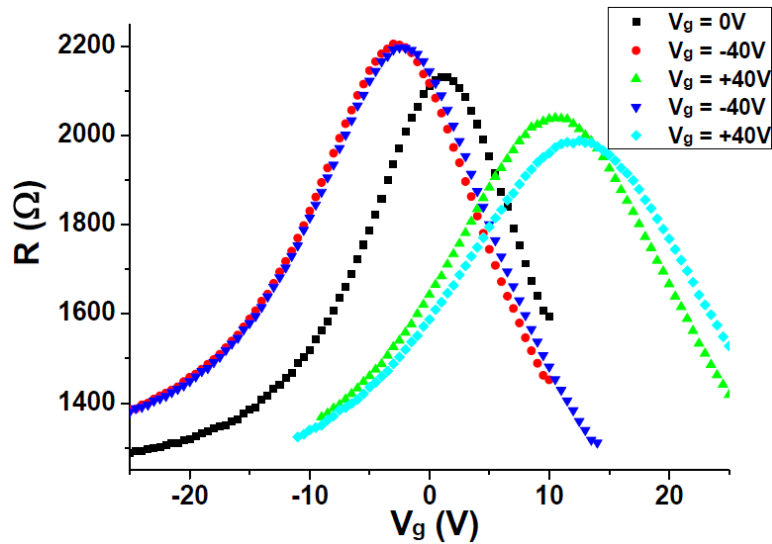
Figure 5.24: Graphene device exposed to a mixture of O_2 and N_2 gases. The overall doping type of graphene is controlled by polarity of the applied V_g. V_g was changed every 30 min in the sequence shown in the legend.

5.4 Summary

In summary, the effects of gas adsorption on the thermal and electrical properties of graphene have been investigated. The adsorbates have negligible effect on the thermal transport in graphene at room temperature, and can form continuous thin films at low temperatures that will improve the total thermal conductance of the system. An n-type doping effect of N_2 molecules is discovered for the first time, and

is attributed to the interaction on single-vacancy defects and graphene edges. The charge transfer rate follows conventional Langmurian kinetics, and is found to depend on the applied gate-voltage that shifts the Fermi level of graphene, and changes the activation energy of the charge transfer process. By mixing p-type O_2 and n-type N_2 in the right proportion as the gas environment, we have realized a graphene device whose doping type can be reversibly controlled by selective charge transfer from the two species.

Chapter 6   Conclusions and Future Work

6.1   Conclusions

In this work, we have developed a process to transfer and pattern graphene samples on a pre-fabricated METS device that incorporates thermal-bridge structures. This approach has two advantages over other existing techniques: it allows precise control over the size and shape of the graphene flake; and it can be used to measure both suspended and supported samples. We have also carried out finite element method simulations to correct a systematic error in the temperature sensing, which had been overlooked in previous works using similar thermal-bridge configurations.

Various factors that could affect the thermal transport in graphene were investigated. It was observed that the room temperature thermal conductivity is comparable to that of bulk graphite for the largest flake, but reduces significantly for smaller flakes due to cut-off of low-frequency phonons involved in heat conduction. This is consistent with the predictions of many theoretical works, and provides the first experimental evidence for the size dependence of the thermal conductivity of graphene. The presence of a substrate was found to impede the thermal transport due to phonon coupling at the interface, and the effect becomes much weaker for thicker flakes showing diminished scattering in the top layers away from the substrate.

The temperature dependence of thermal conductivity obtained for supported samples shows a gradual increase and saturates at $310 - 360$ K, which agrees well with other published results. However, for the suspended sample, it shows no sign of saturation and follows a power law with an exponent of 1.4 ± 0.1, suggesting that the flexural phonon modes contribute significantly to the thermal transport. Thermal boundary scattering at the graphene-contact interfaces was also studied using a novel

non-contact electron beam heating method, which can spatially resolve the thermal resistance at any position on the sample. It was found that significant scattering occurs at the contacts especially for small flakes, as a result of material and structural changes.

Furthermore, the samples were exposed to various gas ambients instead of vacuum to study the effects of surface gas adsorption. It was found that the thermal conductance of graphene is hardly affected at 300 K, but increases substantially at low temperatures. This is attributed to the gas adsorbates condensing into continuous thin films that can act as parallel thermal conduction paths.

On the electrical aspect, it was discovered that adsorption of molecular nitrogen introduces n-type doping to graphene, and the doping rate agrees with that expected from the conventional Langmuirian kinetics. Based on our experiments and density functional theory simulations, the charge transfer was found to take place both at single-vacancy defects and at the edges of graphene, with the latter being the dominant sites.

The doping effect was found to depend on the applied electric field perpendicular to the graphene surface, which can shift the Fermi level of graphene and change the activation energy barrier for the charge transfer process. Interestingly, it is reported that adsorption of oxygen molecules introduces p-type doping effect and the electric field dependence is also opposite to that of nitrogen. By mixing the p-type oxygen and n-type nitrogen gases in the right proportion as the gas environment, we have realized a graphene device whose doping type can be reversibly controlled and switched by changing the electric field as a result of the selective charge transfer from the two species.

6.2 Future work

The sample fabrication process for the thermal devices can be improved. The graphene flake is transferred in deionized water, where residual water molecules could be trapped between the graphene and the SiN_x platform for supported samples. The thermal transport may be affected by this source of contaminants, especially if one wants to study the substrate effect in detail. Hence a dry transfer method similar to the nano-imprinting techniques [130] would be more appealing.

There are still many interesting aspects of the thermal transport we have not investigated. First is the effect of lattice strain on the thermal conductivity of graphene. By patterning holes or trenches on the SiN_x platform with focused ion beam or reactive ion etching, the graphene can be partially suspended. When a gate voltage is applied underneath the SiN_x, the graphene will bend due to electrostatic attraction and a strain will be induced. The $C - C$ bond stretching is expected to adversely affect the phonon propagation, and this can be verified by monitoring the thermal conductivity as the morphology of graphene changes.

In addition, a graphene super-lattice system can be realized if the holes or trenches are patterned in a regular array. As the period of the super-lattice approaches the phonon wavelength in graphene, the thermal conductivity will be reduced to a minimum due to pronounced quantum confinement of the phonons, while the electrical conductivity should be much less affected due to the Klein tunneling of the Dirac fermions (electrons). This can help us in understanding the fundamental physics behind the 2D phonon transport in graphene, which is still a subject of argument [14, 15].

In the gas adsorption studies, the exact mechanism for the increased thermal conductance observed below 158 K still remains unclear, although a reasonable

hypothesis has been suggested. More work can be done on the theoretical side, especially through molecular dynamics simulations, to truly understand the interaction between adsorbates and graphene, as well as between the adsorbates themselves.

The electric-field-controlled doping of graphene in nitrogen and oxygen ambients allows the formation of local p-n junctions on a single sheet of graphene. With the recent advances in large-scale (wafer-sized) graphene growth [131, 132], this opens a new route towards graphene-based electronics. More effort can be devoted into the fabrication and demonstration of a prototype device, which can be simple logic circuits for a start.

References

[1]   K. S. Novoselov, A. K. Geim, S. V. Morozov, D. Jiang, Y. Zhang, S. V. Dubonos, I. V. Grigorieva, and A. A. Firsov. "Electric field effect in atomically thin carbon films", Science, *306*, 666-669. 2004.

[2]   J. C. Charlier, P. C. Eklund, J. Zhu, and A. C. Ferrari. "Electron and phonon properties of graphene: Their relationship with carbon nanotubes", Topics in Applied Physics, *111*, 673-709. 2008.

[3]   P. Avouris, Z. H. Chen, and V. Perebeinos. "Carbon-based electronics", Nat. Nanotech., *2*, 605-615. 2007.

[4]   K. I. Bolotin, K. J. Sikes, Z. Jiang, M. Klima, G. Fudenberg, J. Hone, P. Kim, and H. L. Stormer. "Ultrahigh electron mobility in suspended graphene", Solid State Commun., *146*, 351-355. 2008.

[5]   A. K. Geim and K. S. Novoselov. "The rise of graphene", Nat. Mater., *6*, 183-191. 2007.

[6]   R. Sordan, F. Traversi, and V. Russo. "Logic gates with a single graphene transistor", Appl. Phys. Lett., *94*, 073305. 2009.

[7]   Y. M. Lin, C. Dimitrakopoulos, K. A. Jenkins, D. B. Farmer, H. Y. Chiu, A. Grill, and P. Avouris. "100-GHz transistors from wafer-scale epitaxial graphene", Science, *327*, 662-662. 2010.

[8]   F. Schedin, A. K. Geim, S. V. Morozov, E. W. Hill, P. Blake, M. I. Katsnelson, and K. S. Novoselov. "Detection of individual gas molecules adsorbed on graphene", Nat. Mater., *6*, 652-655. 2007.

[9]   S. Adam, E. H. Hwang, V. M. Galitski, and S. Das Sarma. "A self-consistent theory for graphene transport", Proc. Nat. Acad. Sci. USA, *104*, 18392-18397. 2007.

[10]   J. H. Chen, C. Jang, S. Adam, M. S. Fuhrer, E. D. Williams, and M. Ishigami. "Charged-impurity scattering in graphene", Nat. Phys., *4*, 377-381. 2008.

[11]   K. Saito, J. Nakamura, and A. Natori. "Ballistic thermal conductance of a graphene sheet", Phys. Rev. B, *76*, 115409. 2007.

[12]   N. M. R. Peres, J. dos Santos, and T. Stauber. "Phenomenological study of the electronic transport coefficients of graphene", Phys. Rev. B, *76*, 073412. 2007.

[13]   J. W. Jiang, J. S. Wang, and B. W. Li. "Thermal conductance of graphene and dimerite", Phys. Rev. B, *79*, 205418. 2009.

[14]   A. A. Balandin, S. Ghosh, W. Z. Bao, I. Calizo, D. Teweldebrhan, F. Miao, and C. N. Lau. "Superior thermal conductivity of single-layer graphene", Nano Lett., *8*, 902-907. 2008.

[15]   L. Lindsay, D. A. Broido, and N. Mingo. "Flexural phonons and thermal transport in graphene", Phys. Rev. B, *82*, 115427. 2010.

[16]   C. Faugeras, B. Faugeras, M. Orlita, M. Potemski, R. R. Nair, and A. K. Geim. "Thermal conductivity of graphene in Corbino membrane geometry", ACS Nano, *4*, 1889-1892. 2010.

[17]   L. Shi, W. W. Cai, A. L. Moore, Y. W. Zhu, X. S. Li, S. S. Chen, and R. S. Ruoff. "Thermal transport in suspended and supported monolayer graphene grown by chemical vapor deposition", Nano Lett., *10*, 1645-1651. 2010.

[18]   A. A. Balandin, S. Ghosh, W. Z. Bao, D. L. Nika, S. Subrina, E. P. Pokatilov, and C. N. Lau. "Dimensional crossover of thermal transport in few-layer graphene", Nat. Mater., *9*, 555-558. 2010.

[19]   L. Shi, J. H. Seol, I. Jo, A. L. Moore, L. Lindsay, Z. H. Aitken, M. T. Pettes, X. S. Li, Z. Yao, R. Huang, D. Broido, N. Mingo, and R. S. Ruoff. "Two-dimensional phonon transport in supported graphene", Science, *328*, 213-216. 2010.

[20]   M. W. Lin, C. Ling, Y. Y. Zhang, H. J. Yoon, M. M. C. Cheng, L. A. Agapito, N. Kioussis, N. Widjaja, and Z. X. Zhou. "Room-temperature high on/off ratio in suspended graphene nanoribbon field-effect transistors", Nanotechnology, *22*, 265201. 2011.

[21]   Y. X. Yang and R. Murali. "Impact of size effect on graphene nanoribbon transport", IEEE Electron Device Lett., *31*, 237-239. 2010.

[22]   R. Grassi, A. Gnudi, E. Gnani, S. Reggiani, and G. Baccarani. "Graphene nanoribbons FETs for high-performance logic applications: perspectives and challenges". In Proc. 9th International Conference on Solid-State and Integrated-Circuit Technology, *1-4*, 365-368. 2008.

[23] T. Wang, Q. Guo, Z. M. Ao, Y. Liu, W. B. Wang, K. Sheng, and B. Yu, Chin. "The tunable bandgap of AB-stacked bilayer graphene on SiO_2 with H_2O molecule adsorption", Phys. Lett., *28*, 117302. 2011.

[24] W. J. Zhang, C. T. Lin, K. K. Liu, T. Tite, C. Y. Su, C. H. Chang, Y. H. Lee, C. W. Chu, K. H. Wei, J. L. Kuo, and L. J. Li. "Opening an electrical band gap of bilayer graphene with molecular doping", ACS Nano, *5*, 7517-7524. 2011.

[25] T. Taychatanapat and P. Jarillo-Herrero. "Electronic transport in dual-gated bilayer graphene at large displacement fields", Phys. Rev. Lett., *105*, 166601. 2010.

[26] V. H. Nguyen, A. Bournel, and P. Dollfus. "The conduction gap in double gate bilayer graphene structures", J. Phys.-Condes. Matter, *22*, 115304. 2010.

[27] Z. Jin, J. Yao, C. Kittrell, and J. M. Tour. "Large-scale growth and characterizations of nitrogen-doped monolayer graphene sheets", ACS Nano, *5*, 4112-4117. 2011.

[28] Y. C. Lin, C. Y. Lin, and P. W. Chiu. "Controllable graphene n-doping with ammonia plasma", Appl. Phys. Lett., *96*, 133110. 2010.

[29] W. E. Sawyer, U.S. Patent No.: 229 335. 1880.

[30] A. A. Balandin, "Thermal properties of graphene and nanostructured carbon materials", Nat. Mater., *10*, 569-581. 2011.

[31] M. Pirani and W. Fehse. "Origin and characteristics of pure graphite", Zeitschrift Fur Elektrochemie Und Angewandte Physikalische Chemie, *29*, 168-174. 1923.

[32] S. Mrozowski. "Thermal conductivity of carbons and graphite", Phys. Rev., *86*, 251-252. 1952.

[33] J. M. Ziman. Electrons and Phonons. Oxford: Clarendon. 2001.

[34] Y. A. Logatchov and A. S. Skal. "Theory of basal plane thermal conductivity of graphite", Carbon, *9*, 711-714. 1971.

[35] R. Taylor, K. E. Gilchrist, and L. J. Poston. "Thermal conductivity of polycrystalline graphite", Carbon, *6*, 537-544. 1968.

[36]   G. A. Slack. "Anisotropic thermal conductivity of pyrolytic graphite", Phys. Rev., *127*, 694-701. 1962.

[37]   B. T. Kelly. "Effect of defects on basal plane thermal conductivity of a graphite crystal", Carbon, *5*, 247-260. 1967.

[38]   P. Kim, L. Shi, A. Majumdar, and P. L. McEuen. "Thermal transport measurements of individual multiwalled nanotubes", Phys. Rev. Lett., *87*, 215502. 2001.

[39]   L. Shi, D. Y. Li, C. H. Yu, W. Y. Jang, D. Kim, Z. Yao, P. Kim, and A. Majumdar. "Measuring thermal and thermoelectric properties of one-dimensional nanostructures using a microfabricated device", J. Heat Trans., *125*, 881-888. 2003.

[40]   K. Schwab, E. A. Henriksen, J. M. Worlock, and M. L. Roukes. "Measurement of the quantum of thermal conductance", Nature, *404*, 974-977. 2000.

[41]   B. T. Kelly. Physics of Graphite. London: Applied Science Publishers. 1981.

[42]   W. Yi, L. Lu, D. L. Zhang, Z. W. Pan, and S. S. Xie. "Linear specific heat of carbon nanotubes", Phys. Rev. B, *59*, R9015-R9018. 1999.

[43]   S. Lepri, R. Livi, and A. Politi. "Heat conduction in chains of nonlinear oscillators", Phys. Rev. Lett., *78*, 1896-1899. 1997.

[44]   A. V. Savin and O. V. Gendelman. "Heat conduction in one-dimensional lattices with on-site potential", Phys. Rev. E, *67*, 041205. 2003.

[45]   G. Zhang and B. W. Li. "Thermal conductivity of nanotubes revisited: effects of chirality, isotope impurity, tube length, and temperature", J. Chem. Phys., *123*, 114714. 2005.

[46]   T. Mai and O. Narayan. "Universality of one-dimensional heat conductivity", Phys. Rev. E, *73*, 061202. 2006.

[47]   L. Yang, P. Grassberger, and B. Hu. "Dimensional crossover of heat conduction in low dimensions", Phys. Rev. E, *74*, 062101. 2006.

[48] B. W. Li, H. Zhao, and B. B. Hu. "Can disorder induce a finite thermal conductivity in 1D lattices?", Phys. Rev. Lett., *86*, 63-66. 2001.

[49] C. W. Chang, D. Okawa, H. Garcia, A. Majumdar, and A. Zettl. "Breakdown of Fourier's law in nanotube thermal conductors", Phys. Rev. Lett., *101*, 075903. 2008.

[50] L. Lindsay, D. A. Broido, and N. Mingo. "Diameter dependence of carbon nanotube thermal conductivity and extension to the graphene limit", Phys. Rev. B, *82*, 161402. 2010.

[51] X. H. Yan, Y. Xiao, and Z. M. Li. "Effects of intertube coupling and tube chirality on thermal transport of carbon nanotubes", J. Appl. Phys., *99*, 124305. 2006.

[52] J. Hone, M. Whitney, C. Piskoti, and A. Zettl. "Thermal conductivity of single-walled carbon nanotubes", Phys. Rev. B, *59*, R2514-R2516. 1999.

[53] J. Hone, M. C. Llaguno, N. M. Nemes, A. T. Johnson, J. E. Fischer, D. A. Walters, M. J. Casavant, J. Schmidt, and R. E. Smalley. "Electrical and thermal transport properties of magnetically aligned single wall carbon nanotube films", Appl. Phys. Lett., *77*, 666-668. 2000.

[54] L. M. Ericson, H. Fan, H. Q. Peng, V. A. Davis, W. Zhou, J. Sulpizio, Y. H. Wang, R. Booker, J. Vavro, C. Guthy, A. N. G. Parra-Vasquez, M. J. Kim, S. Ramesh, R. K. Saini, C. Kittrell, G. Lavin, H. Schmidt, W. W. Adams, W. E. Billups, M. Pasquali, W. F. Hwang, R. H. Hauge, J. E. Fischer, and R. E. Smalley. "Macroscopic, neat, single-walled carbon nanotube fibers", Science, *305*, 1447-1450. 2004.

[55] J. E. Fischer, W. Zhou, J. Vavro, M. C. Llaguno, C. Guthy, R. Haggenmueller, M. J. Casavant, D. E. Walters, and R. E. Smalley. "Magnetically aligned single wall carbon nanotube films: preferred orientation and anisotropic transport properties", J. Appl. Phys., *93*, 2157-2163. 2003.

[56] S. Badaire, V. Pichot, C. Zakri, P. Poulin, P. Launois, J. Vavro, C. Guthy, M. Chen, and J. E. Fischer. "Correlation of properties with preferred orientation in coagulated and stretch-aligned single-wall carbon nanotubes", J. Appl. Phys., *96*, 7509-7513. 2004.

[57] D. J. Yang, Q. Zhang, G. Chen, S. F. Yoon, J. Ahn, S. G. Wang, Q. Zhou, Q. Wang, and J. Q. Li. "Thermal conductivity of multiwalled carbon nanotubes", Phys. Rev. B, *66*, 165440. 2002.

[58] W. Zhou, J. Vavro, C. Guthy, K. I. Winey, J. E. Fischer, L. M. Ericson, S. Ramesh, R. Saini, V. A. Davis, C. Kittrell, M. Pasquali, R. H. Hauge, and R. E. Smalley. "Single wall carbon nanotube fibers extruded from super-acid suspensions: preferred orientation, electrical, and thermal transport", J. Appl. Phys., *95*, 649-655. 2004.

[59] X. W. Wang, Z. R. Zhong, and J. Xu. "Noncontact thermal characterization of multiwall carbon nanotubes", J. Appl. Phys., *97*, 064302. 2005.

[60] S. Berber, Y. K. Kwon, and D. Tomanek. "Unusually high thermal conductivity of carbon nanotubes", Phys. Rev. Lett., *84*, 4613-4616. 2000.

[61] P. Kim, L. Shi, A. Majumdar, and P. L. McEuen. "Mesoscopic thermal transport and energy dissipation in carbon nanotubes", Physica B, *323*, 67-70. 2002.

[62] H. Y. Chiu, V. V. Deshpande, H. W. C. Postma, C. N. Lau, C. Miko, L. Forro, and M. Bockrath. "Ballistic phonon thermal transport in multiwalled carbon nanotubes", Phys. Rev. Lett., *95*, 226101. 2005.

[63] N. Mingo and D. A. Broido. "Carbon nanotube ballistic thermal conductance and its limits", Phys. Rev. Lett., *95*, 096105. 2005.

[64] J. A. Wang and J. S. Wang. "Carbon nanotube thermal transport: ballistic to diffusive", Appl. Phys. Lett., *88*, 111909. 2006.

[65] I. K. Hsu, M. T. Pows, A. Bushmaker, M. Aykol, L. Shi, and S. B. Cronin. "Optical absorption and thermal transport of individual suspended carbon nanotube bundles", Nano Lett., *9*, 590-594. 2009.

[66] D. J. Yang, S. G. Wang, Q. Zhang, P. J. Sellin, and G. Chen. "Thermal and electrical transport in multi-walled carbon nanotubes", Phys. Lett. A, *329*, 207-213. 2004.

[67] I. Calizo, F. Miao, W. Bao, C. N. Lau, and A. A. Balandin. "Variable temperature Raman microscopy as a nanometrology tool for graphene layers and graphene-based devices", Appl. Phys. Lett., *91*, 071913. 2007.

[68] I. Calizo, A. A. Balandin, W. Bao, F. Miao, and C. N. Lau. "Temperature dependence of the Raman spectra of graphene and graphene multilayers", Nano Lett., *7*, 2645-2649. 2007.

[69] J. U. Lee, D. Yoon, H. Kim, S. W. Lee, and H. Cheong. "Thermal conductivity of suspended pristine graphene measured by Raman spectroscopy", Phys. Rev. B, *83*, 081419. 2011.

[70] L. Shi, S. C. Chen, S. S., A. L. Moore, W. W. Cai, J. W. Suk, J. H. An, C. Mishra, C. Amos, C. W. Magnuson, J. Y. Kang, and R. S. Ruoff. "Raman measurements of thermal transport in suspended monolayer graphene of variable sizes in vacuum and gaseous environments", ACS Nano, *5*, 321-328. 2011.

[71] L. Shi, J. H. Seol, A. L. Moore, I. Jo, and Z. Yao. "Thermal conductivity measurement of graphene exfoliated on silicon dioxide", J. Heat Trans., *133*, 022403. 2011.

[72] L. Shi, M. P. Pettes, M. T., I. S. Jo, and Z. Yao. "Influence of polymeric residue on the thermal conductivity of suspended bilayer graphene", Nano Lett., *11*, 1195-1200. 2011.

[73] A. A. Balandin, D. L. Nika, S. Ghosh, and E. P. Pokatilov. "Lattice thermal conductivity of graphene flakes: comparison with bulk graphite", Appl. Phys. Lett., *94*, 203103. 2009.

[74] A. A. Balandin, S. Ghosh, I. Calizo, D. Teweldebrhan, E. P. Pokatilov, D. L. Nika, W. Bao, F. Miao, and C. N. Lau. "Extremely high thermal conductivity of graphene: prospects for thermal management applications in nanoelectronic circuits", Appl. Phys. Lett., *92*, 151911. 2008.

[75] N. Mounet and N. Marzari. "First-principles determination of the structural, vibrational and thermodynamic properties of diamond, graphite, and derivatives", Phys. Rev. B, *71*, 205214. 2005.

[76] B. D. Kong, S. Paul, M. B. Nardelli, and K. W. Kim. "First-principles analysis of lattice thermal conductivity in monolayer and bilayer graphene", Phys. Rev. B, *80*, 033406. 2009.

[77] P. G. Klemens and D. F. Pedraza. "Thermal-conductivity of graphite in the basal-plane", Carbon, *32*, 735-741. 1994.

[78] C. Dames, W. Y. Jang, Z. Chen, W. Z. Bao, and C. N. Lau. "Thickness-dependent thermal conductivity of encased graphene and ultrathin graphite", Nano Lett., *10*, 3909-3913. 2010.

[79]   P. G. Klemens. "Theory of the A-plane thermal conductivity of graphite", J. Wide Bandgap Mater., *7*, 332-339. 2000.

[80]   P. G. Klemens. "Theory of thermal conduction in thin ceramic films", Int. J. Thermophys., *22*, 265-275. 2001.

[81]   S. Lepri, R. Livi, and A. Politi. "Thermal conduction in classical low-dimensional lattices", Phys. Rep., *377*, 1-80. 2003.

[82]   O. Narayan and S. Ramaswamy. "Anomalous heat conduction in one-dimensional momentum-conserving systems", Phys. Rev. Lett., *89*, 200601. 2002.

[83]   G. Basile, C. Bernardin, and S. Olla. "Momentum conserving model with anomalous thermal conductivity in low dimensional systems", Phys. Rev. Lett., *96*, 204303. 2006.

[84]   A. A. Balandin, D. L. Nika, E. P. Pokatilov, and A. S. Askerov. "Phonon thermal conduction in graphene: role of Umklapp and edge roughness scattering", Phys. Rev. B, *79*, 155413. 2009.

[85]   M. Omini and A. Sparavigna. "Effect of phonon scattering by isotope impurities on the thermal conductivity of dielectric solids", Physica B, *233*, 230-240. 1997.

[86]   L. Lindsay, D. A. Broido, and N. Mingo. "Lattice thermal conductivity of single-walled carbon nanotubes: beyond the relaxation time approximation and phonon-phonon scattering selection rules", Phys. Rev. B, *80*, 125407. 2009.

[87]   A. Ward, D. A. Broido, D. A. Stewart, and G. Deinzer. "Ab initio theory of the lattice thermal conductivity in diamond", Phys. Rev. B, *80*, 125203. 2009.

[88]   A. A. Balandin, S. Ghosh, D. L. Nika, and E. P. Pokatilov. "Heat conduction in graphene: experimental study and theoretical interpretation", New J. Phys., *11*, 095012. 2009.

[89]   Z. Aksamija and I. Knezevic. "Lattice thermal conductivity of graphene nanoribbons: anisotropy and edge roughness scattering", Appl. Phys. Lett., *98*, 141919. 2011.

[90]   H. Sevincli and G. Cuniberti. "Enhanced thermoelectric figure of merit in edge-disordered zigzag graphene nanoribbons", Phys. Rev. B, *81*, 113401. 2010.

[91]   K. Cho, H. J. Zhang, G. Lee, A. F. Fonseca, and T. L. Borders. "Isotope effect on the thermal conductivity of graphene", J. Nanomater., 537657. 2010.

[92]   J. M. Ziman. Electrons and Phonons: The Theory of Transport Phenomena in Solids. Oxford: Clarendon Press. 1960.

[93]   L. Colombo, X. S. Li, W. W. Cai, and R. S. Ruoff. "Evolution of graphene growth on Ni and Cu by carbon isotope labeling", Nano Lett., *9*, 4268-4272. 2009.

[94]   J. N. Hu, S. Schiffli, A. Vallabhaneni, X. L. Ruan, and Y. P. Chen. "Tuning the thermal conductivity of graphene nanoribbons by edge passivation and isotope engineering: a molecular dynamics study", Appl. Phys. Lett., *97*, 133107. 2010.

[95]   Z. Chen, W. Jang, W. Bao, C. N. Lau, and C. Dames. "Thermal contact resistance between graphene and silicon dioxide", Appl. Phys. Lett., *95*, 161910. 2009.

[96]   Y. K. Koh, M. H. Bae, D. G. Cahill, and E. Pop. "Heat conduction across monolayer and few-layer graphenes", Nano Lett., *10*, 4363-4368. 2010.

[97]   R. Prasher. "Thermal boundary resistance and thermal conductivity of multiwalled carbon nanotubes", Phys. Rev. B, *77*, 075424. 2008.

[98]   A. J. Schmidt, K. C. Collins, A. J. Minnich, and G. Chen. "Thermal conductance and phonon transmissivity of metal-graphite interfaces", J. Appl. Phys., *107*, 104907. 2010.

[99]   N. S. Snyder. "Heat transport through helium II: Kapitza conductance", Cryogenics, *10*, 89-95. 1970.

[100]   C. Dames and G. Chen. "Theoretical phonon thermal conductivity of Si/Ge superlattice nanowires", J. Appl. Phys., *95*, 682-693. 2004.

[101]   J. C. Duda, J. L. Smoyer, P. M. Norris, and P. E. Hopkins. "Extension of the diffuse mismatch model for thermal boundary conductance between isotropic and anisotropic materials", Appl. Phys. Lett., *95*, 031912. 2009.

[102] C. O. Girit, J. C. Meyer, R. Erni, M. D. Rossell, C. Kisielowski, L. Yang, C.-H. Park, M. F. Crommie, M. L. Cohen, S. G. Louie, and A. Zettl. "Graphene at the edge: stability and dynamics", Science, *323*, 1705-1708. 2009.

[103] D. L. Nika, S. Ghosh, E. P. Pokatilov, and A. A. Balandin. "Lattice thermal conductivity of graphene flakes: comparison with bulk graphite", Appl. Phys. Lett., *94*, 203103. 2009.

[104] Z. Y. Ong and E. Pop. "Effect of substrate modes on thermal transport in supported graphene", Phys. Rev. B, *84*, 075471. 2011.

[105] E. H. Hwang, E. Rossi, and S. Das Sarma. "Theory of thermopower in two-dimensional graphene", Phys. Rev. B, *80*, 235415. 2009.

[106] S. J. Clark, M. D. Segall, C. J. Pickard, P. J. Hasnip, M. J. Probert, K. Refson, and M. C. Payne. "First principles methods using CASTEP", Zeitschrift Fur Kristallographie, *220*, 567-570. 2005.

[107] X. X. Ni, G. C. Liang, J. S. Wang, and B. W. Li. "Disorder enhances thermoelectric figure of merit in armchair graphane nanoribbons", Appl. Phys. Lett., *95*, 192114. 2009.

[108] T. Markussen, A. P. Jauho, and M. Brandbyge. "Electron and phonon transport in silicon nanowires: atomistic approach to thermoelectric properties", Phys. Rev. B, *79*, 035415. 2009.

[109] D. L. Nika, E. P. Pokatilov, A. S. Askerov, and A. A. Balandin. "Phonon thermal conduction in graphene: role of Umklapp and edge roughness scattering", Phys. Rev. B, *79*, 155413. 2009.

[110] W. Y. Jang, Z. Chen, W. Z. Bao, C. N. Lau, and C. Dames. "Thickness-dependent thermal conductivity of encased graphene and ultrathin graphite", Nano Lett., *10*, 3909-3913. 2010.

[111] J. H. Lan, J. S. Wang, C. K. Gan, and S. K. Chin. "Edge effects on quantum thermal transport in graphene nanoribbons: tight-binding calculations", Phys. Rev. B, *79*, 115401. 2009.

[112] C. Lee, X. D. Wei, J. W. Kysar, and J. Hone. "Measurement of the elastic properties and intrinsic strength of monolayer graphene", Science, *321*, 385-388. 2008.

[113]   H. L. Zhong and J. R. Lukes. "Interfacial thermal resistance between carbon nanotubes: molecular dynamics simulations and analytical thermal modeling", Phys. Rev. B, *74*, 125403. 2006.

[114]   F. X. Alvarez, J. Alvarez-Quintana, D. Jou, and J. R. Viejo. "Analytical expression for thermal conductivity of superlattices", J. Appl. Phys., *107*, 084303. 2010.

[115]   S. Peng, K. J. Cho, P. F. Qi, and H. J. Dai. "Ab initio study of CNT NO_2 gas sensor", Chem. Phys. Lett., *387*, 271-276. 2004.

[116]   G. Lee, B. Lee, J. Kim, and K. Cho. "Ozone adsorption on graphene: ab initio study and experimental validation", J. Phys. Chem. C, *113*, 14225-14229. 2009.

[117]   T. Klitsner and R. O. Pohl. "Phonon-scattering at silicon crystal-surfaces", Phys. Rev. B, *36*, 6551-6565. 1987.

[118]   T. Klitsner and R. O. Pohl. "Phonon-scattering at a crystal surface from *in situ* -deposited thin films", Phys. Rev. B, *34*, 6045-6048. 1986.

[119]   P. L. Garrity. "Dynamic phonon scattering rates of nanosurfaces with gas particles", Nanotechnology, *18*, 365703. 2007.

[120]   C. Marti, T. Ceva, B. Croset, C. Debeauvais, and A. Thomy. "The SF_6 monolayer on graphite by X-ray diffraction", J. Phys. France, *47*, 1517-1522. 1986.

[121]   P. Thomas, Y. Xia, D. A. Boyd, T. A. Hopkins, and G. B. Hess. "Study of SF_6 adsorption on graphite using infrared spectroscopy", J. Chem. Phys., *131*, 124709. 2009.

[122]   D. Mann, E. Pop, J. Cao, Q. Wang, K. E. Goodson, and H. J. Dai. "Thermally and molecularly stimulated relaxation of hot phonons in suspended carbon nanotubes", J. Phys. Chem. B, *110*, 1502-1505. 2006.

[123]   T. H. Yu, C. W. Liang, C. D. Kim, and B. Yu. "Local electrical stress-induced doping and formation of monolayer graphene P-N junction", Appl. Phys. Lett., *98*, 243105. 2011.

[124] W. J. Zhu, V. Perebeinos, M. Freitag, and P. Avouris. "Carrier scattering, mobilities, and electrostatic potential in monolayer, bilayer, and trilayer graphene", Phys. Rev. B, *80*, 235402. 2009.

[125] V. E. Dorgan, M. H. Bae, and E. Pop. "Mobility and saturation velocity in graphene on SiO_2", Appl. Phys. Lett., *97*, 082112. 2010.

[126] Y. Sato, K. Takai, and T. Enoki. "Electrically controlled adsorption of oxygen in bilayer graphene devices", Nano Lett., *11*, 4026-4026. 2011.

[127] Z. H. Ni, H. M. Wang, Z. Q. Luo, Y. Y. Wang, T. Yu, Y. H. Wu, and Z. X. Shen. "The effect of vacuum annealing on graphene", J. Raman Spectrosc., *41*, 479-483. 2010.

[128] B. Sanyal, O. Eriksson, U. Jansson, and H. Grennberg. "Molecular adsorption in graphene with divacancy defects", Phys. Rev. B, *79*, 113409. 2009.

[129] A. Goldoni, R. Larciprete, L. Petaccia, and S. Lizzit. "Single-wall carbon nanotube interaction with gases: sample contaminants and environmental monitoring", J. Am. Chem. Soc., *125*, 11329-11333. 2003.

[130] S. Y. Chou, P. R. Krauss, and P. J. Renstrom. "Imprint lithography with 25-nanometer resolution", Science, *272*, 85-87. 1996.

[131] K. V. Emtsev, A. Bostwick, K. Horn, J. Jobst, G. L. Kellogg, L. Ley, J. L. McChesney, T. Ohta, S. A. Reshanov, J. Rohrl, E. Rotenberg, A. K. Schmid, D. Waldmann, H. B. Weber, and T. Seyller. "Towards wafer-size graphene layers by atmospheric pressure graphitization of silicon carbide", Nat. Mater., *8*, 203-207. 2009.

[132] X. S. Li, W. W. Cai, J. H. An, S. Kim, J. Nah, D. X. Yang, R. Piner, A. Velamakanni, I. Jung, E. Tutuc, S. K. Banerjee, L. Colombo, and R. S. Ruoff. "Large-area synthesis of high-quality and uniform graphene films on copper foils", Science, *324*, 1312-1314. 2009.

Appendix: Publications

I. Thesis-related Publications

- **Ziqian Wang**, Rongguo Xie, Cong Tinh Bui, Dan Liu, Xiaoxi Ni, Baowen Li, and John T. L. Thong. "Thermal transport in suspended and supported few-layer graphene", Nano Lett., *11*, 113-118, 2011.

  Featured in "Graphene: how hot is it?", Nature Publishing Group, Asia Materials research highlight, 18 April 2011.

- **Ziqian Wang**, Rongguo Xie, Miao Zhou, Yuan Ping Feng, Baowen Li, and John T. L. Thong. "Reversible doping of graphene by electrically controlled gas adsorption", Appl. Phys. Lett., to be submitted.

II. Other Publications

- Rui Wang, Yufeng Hao, **Ziqian Wang**, Hao Gong, and John T. L. Thong. "Large-diameter graphene nanotubes synthesized using Ni nanowire templates", Nano Lett., *10*, 4844-4850, 2010.

- Shuai Wang, Priscilla Kailian Ang, **Ziqian Wang**, Ai Ling Lena Tang, John T. L. Thong, and Kian Ping Loh. "High mobility, printable, and solution-processed graphene electronics", Nano Lett., *10*, 92-98, 2010.

- Yufeng Hao, Yingying Wang, Lei Wang, Zhenhua Ni, **Ziqian Wang**, Rui Wang, Chee Keong Koo, Zexiang Shen, and John T. L. Thong. "Probing layer number and stacking order of few-layer graphene by Raman spectroscopy", Small, *6*, 195-200, 2010.

- Chee Leong Wong, Meenakshi Annamalai, **Ziqian Wang**, and Moorthi Palaniapan. "Characterization of nanomechanical graphene drum structures", J. Micromech. Microeng., *20*, 115029, 2010.